PROPERTIES OF WORKING FLUIDS
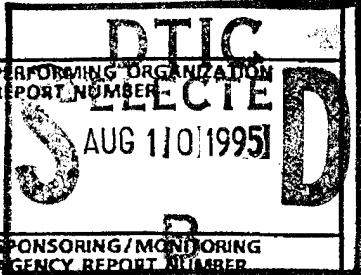# FOR THERMOACOUSTIC REFRIGERATORS

ANNUAL REPORT

Submitted by:
Michael R. Moldover and Keith A. Gillis
Thermophysics Division
Chemical Science and Technology Laboratory
National Institute of Standards and Technology
Gaithersburg, MD 20899

19950808 010

July 1995

REPORT DOCUMENTATION PAGE

Public reporting burden for this collection of information is estimated to average 1 hour per response, including the time for reviewing instructions, searching existing data sources, gathering and maintaining the data needed, and completing and reviewing the collection of information. Send comments regarding this burden estimate or any other aspect of this collection of information, including suggestions for reducing this burden, to Washington Headquarters Services, Directorate for Information Operations and Reports, 1215 Jefferson Davis Highway, Suite 1204, Arlington, VA 22202-4302, and to the Office of Management and Budget, Paperwork Reduction Project (0704-0188), Washington, DC 20503.

1. AGENCY USE ONLY (Leave blank)	2. REPORT DATE 8/01/95	3. REPORT TYPE AND DATES COVERED Annual Report 10/1/94 – 09/30/95

4. TITLE AND SUBTITLE	5. FUNDING NUMBERS
Properties of Working Fluids for Thermoacoustic Refrigerators	PE 61153N G N00014-93-F-0101

6. AUTHOR(S)

M.R. Moldover and K.A. Gillis

7. PERFORMING ORGANIZATION NAME(S) AND ADDRESS(ES)

National Institute of Standards and Technology

8. PERFORMING ORGANIZATION REPORT NUMBER

DTIC SELECTED
AUG 10 1995

9. SPONSORING/MONITORING AGENCY NAME(S) AND ADDRESS(ES)

Office of Naval Research
ONR 331
800 North Quincy Street
Arlington, VA 22217-5660

10. SPONSORING/MONITORING AGENCY REPORT NUMBER

11. SUPPLEMENTARY NOTES
Enclosed preprint entitled: "Greenspan acoustic viscometer for gases," by K.A. Gillis, J.B. Mehl, and M.R. Moldover, submitted to Review of Scientific Instruments

12a. DISTRIBUTION/AVAILABILITY STATEMENT	12b. DISTRIBUTION CODE
Approved for public release: Distribution unlimited	

13. ABSTRACT (Maximum 200 words)

The objective of this project is to provide thermophysical property data for candidate working fluids in a form suitable for optimizing the design of thermoacoustic refrigerators. The data will be provided in a computer program that calculates the properties of the most promising gas mixtures. This package will consist of currently available data from the literature (provided that it is of sufficient quality) and our own measurements (when insufficient literature data exist). The properties provided are viscosity, thermal conductivity, Prandtl number, density, speed-of-sound, specific heat, enthalpy, and entropy for temperatures between –20 and 30 C and pressures up to 20 bars. We will also explore methods of varying the composition of the working fluid to maintain a constant speed of sound over the operating range of the refrigerator.

14. SUBJECT TERMS	15. NUMBER OF PAGES
Thermoacoustics, Thermophysical properties, Prandtl Number, viscosity, noble gas mixtures, viscometry	
	16. PRICE CODE

17. SECURITY CLASSIFICATION OF REPORT	18. SECURITY CLASSIFICATION OF THIS PAGE	19. SECURITY CLASSIFICATION OF ABSTRACT	20. LIMITATION OF ABSTRACT
Unclassified	Unclassified	Unclassified	

DTIC QUALITY INSPECTED 5

TABLE OF CONTENTS

PROPERTIES OF WORKING FLUIDS FOR THERMOACOUSTIC REFRIGERATORS

ANNUAL REPORT

I. Brief Description of Project

The objective of this project is to provide thermophysical property data for candidate working fluids in a form suitable for optimizing the design of thermoacoustic refrigerators. The data will be provided in a computer program that calculates the properties of the most promising gas mixtures. This package will consist of currently available data from the literature (provided that it is of sufficient quality) and our own measurements (when insufficient literature data exist). The properties provided are viscosity, thermal conductivity, Prandtl number, density, speed-of-sound, specific heat, enthalpy, and entropy for temperatures between -20 and 30 C and pressures up to 20 bars. We will also explore methods of varying the composition of the working fluid to maintain a constant speed of sound over the operating range of the refrigerator.

II. Brief Description of Approach Taken

The computer program NOBLEG is an adaptation of our reference database for alternative refrigerants known as REFPROP. NOBLEG is specifically optimized to provide gas phase properties for noble gases, a few other simple gases, and their mixtures. The density, speed-of-sound, enthalpy, and entropy are calculated from the equation of state and the ideal gas heat capacity. The data originated from a combination of published measurements, our own measurements, or calculations from the best-known intermolecular potentials. The transport properties are calculated from collision integrals or from fits to actual measurements.

We measure the speed of sound in gases with a high Q acoustic resonator that has been well characterized. With this technique, we can measure sound speeds to about 0.01% and heat capacities to about 0.1%. We can also get accurate information about the equation of state at low temperatures from the acoustic data. In order to determine the speed of sound in an arbitrary mixture of two noble gases, the interaction acoustic virial coefficients β_{12}, γ_{112}, and γ_{221} must be measured in addition to the pure gas virial coefficients β_{11}, γ_{111}, β_{22}, and γ_{222}. Three mixtures of known composition, in addition to samples of the pure components, are required for these measurements.

Our apparatus for determining gas densities is based on the Burnett technique, and with it we can determine densities to about 0.02% over a wide temperature and pressure range. The Burnett data are combined with the acoustic data to determine the final $P\rho T$ surface. Again three mixtures must be studied in order to determine the interaction virial coefficients B_{12}, C_{112}, and C_{221}.

We have two devices for measuring transport properties of gases which have been developed under this project. The first is the Greenspan acoustic viscometer and the other is a

2

device for measuring the Prandtl number. Both of these devices utilize *new* techniques and show great promise for being the preferred method of measuring transport properties of gases.

III. Brief Description of Accomplishments

A. Density of He-Xe mixtures

We have completed $P\rho T$ measurements on helium, xenon, and three helium-xenon mixtures. The He/Xe mixtures had nominal molar compositions of 75/25, 50/50, and 25/75. The precise composition of each mixture was determined from speed of sound measurements. The measurements span the temperature range 273 K to 373 K, and a pressure range 0.5 to 5.0 MPA. Approximately 250 data points define the $P\rho Tx$ surface from which the interaction virial coefficients will be determined. A final analysis will be performed when the acoustic measurements are complete. (See Appendix A for a detailed report)

B. Experimental measurements of viscosity and Prandtl number

We have measured the viscous diffusivity of argon, helium, and propane using four Greenspan viscometers with different geometries. Figure 1 shows a cross section of one such device. The model used to analyze the data is described in section C below. The measurements were performed at pressures between 25 and 1000 kPa, and spanned a factor of 350 in viscous diffusivity, as shown in Fig. 2. For each of the instruments, the results for the viscosities of the three gases were consistent within ± 0.5%. Without calibration, the viscosities deduced from "the best" viscometer were 1% larger than data from the literature; the viscosities from "the worst" viscometer were 3% larger than data from the literature. The systematic differences can be removed by calibration with a single gas at a single temperature and pressure to yield results that fall within ± 0.5% of the literature data. The apparatus is currently being modified to extend the temperature and pressure ranges in preparation for viscosity measurements on He-Xe mixtures. (See Appendix B for a detailed report)

We have developed a second acoustic device with which information about both the thermal conductivity and the viscosity of a gas may be obtained. The device is a modified cylindrical acoustic resonator with an insert in the middle, as shown in Fig. 3. The insert consists of many parallel, hexagonally-shaped ducts and has a large surface area-to-volume ratio. The increased surface area near the center of the resonator causes a corresponding increase in the energy loss there. Whether the increased loss is due to viscous drag or to heat transport depends on the acoustic mode under study. Modes for which the tangential particle velocity has an anti-node within the insert (odd-numbered longitudinal modes) will exhibit an increased viscous loss. Modes for which the acoustic temperature has an anti-node within the insert (even-numbered longitudinal modes) will exhibit an increased thermal loss. Figure 4 shows how the even and odd modes are shifted relative to the modes without the insert, consistent with our model (see section C). Although the present device is not suitable for absolute measurements of viscosity and thermal conductivity, it is possible to obtain accurate measurements of the Prandtl number. We have completed a series of Prandtl number measurements for argon, helium, and propane. The

3

measurements were performed at room temperature and spanned pressures between 40 kPa and 1000 kPa. Figure 5 shows the measured Prandtl numbers as differences from the values based on data from the literature. If the systematic differences were removed by a calibration with argon, then the Prandtl numbers for helium would fall within 0.5% of the literature values, and the Prandtl numbers for propane would be within 1.5% of the literature values. Note that these differences fall within the estimated errors of the literature data.

C. Theories for the Greenspan viscometer and the Prandtl number meter

Jim Mehl has performed extensive numerical calculations of the acoustic response of the Greenspan viscometer. His results have been used to verify the analytic model, to provide a theoretical basis for the duct end corrections, and to test the importance of various geometrical perturbations. Mehl has calculated the inertial and dissipative effects of nonuniform flow near the ends of the duct; current analytic models of these effects are based on approximations of the flow field whose accuracy is uncertain. These effects are included in the analytical model through a series acoustic impedance Z_{end}

$$Z_{end} = (\rho\omega/A_d)(i\delta_i + \delta_R)$$

where δ_i is the inertial correction given by

$$\frac{\delta_i}{r_d} = 0.8215 - 1.107\frac{r_d}{r_{ch}} + \frac{L_{ch}r_d}{3r_{ch}^2}$$

in terms of the duct radius r_d, the chamber radius r_{ch} and the chamber length L_{ch}. The inertial correction directly affects the resonance frequency. The dissipative correction δ_R describes additional viscous dissipation due to nonuniform flow just inside and just outside the duct opening, and it is approximately equal to $0.81\delta_v$ for our geometry. An important advantage of Mehl's approach is that *any* geometry can be investigated. Mehl has investigated the effects of rounding the corner at the ends of the duct. For instance, if the corner is rounded with a radius equal to $0.1r_d$, then δ_R is reduced to $0.74\delta_v$. (See Appendix C1 for a detailed report)

We have developed a quantitative analytic model for the Greenspan viscometer that includes thermoviscous losses in the duct and in the chambers, duct end corrections, the presence of a fill duct, and transducer response. This model describes the response of the gas as a function of the drive frequency in terms of the gas properties and the resonator geometry. The model is central to the determination of gas viscosity from our experimental measurements with this device. (See Appendix C2 for a detailed report)

We have also developed a model for the Prandtl number meter mentioned in section B above. Our model assumes that the entire volume of the device as a series of parallel circular ducts. Each duct is divided into three sections along its length. The central section has a length L_d and cross sectional area A and represents the portion within the insert. This section is treated with a thermoviscous boundary condition. The two outer sections of the duct each have a length L_c and cross sectional area $A'>A$. These sections are treated with slip boundary conditions. The total length of the resonator L equals $2L_c + L_d$. The model predicts that the odd-numbered

longitudinal modes of this device will be shifted to lower frequencies relative to a resonator without an insert, whereas the even-numbered modes will be shifted upwards in frequency. (See Appendix C3 for a detailed report)
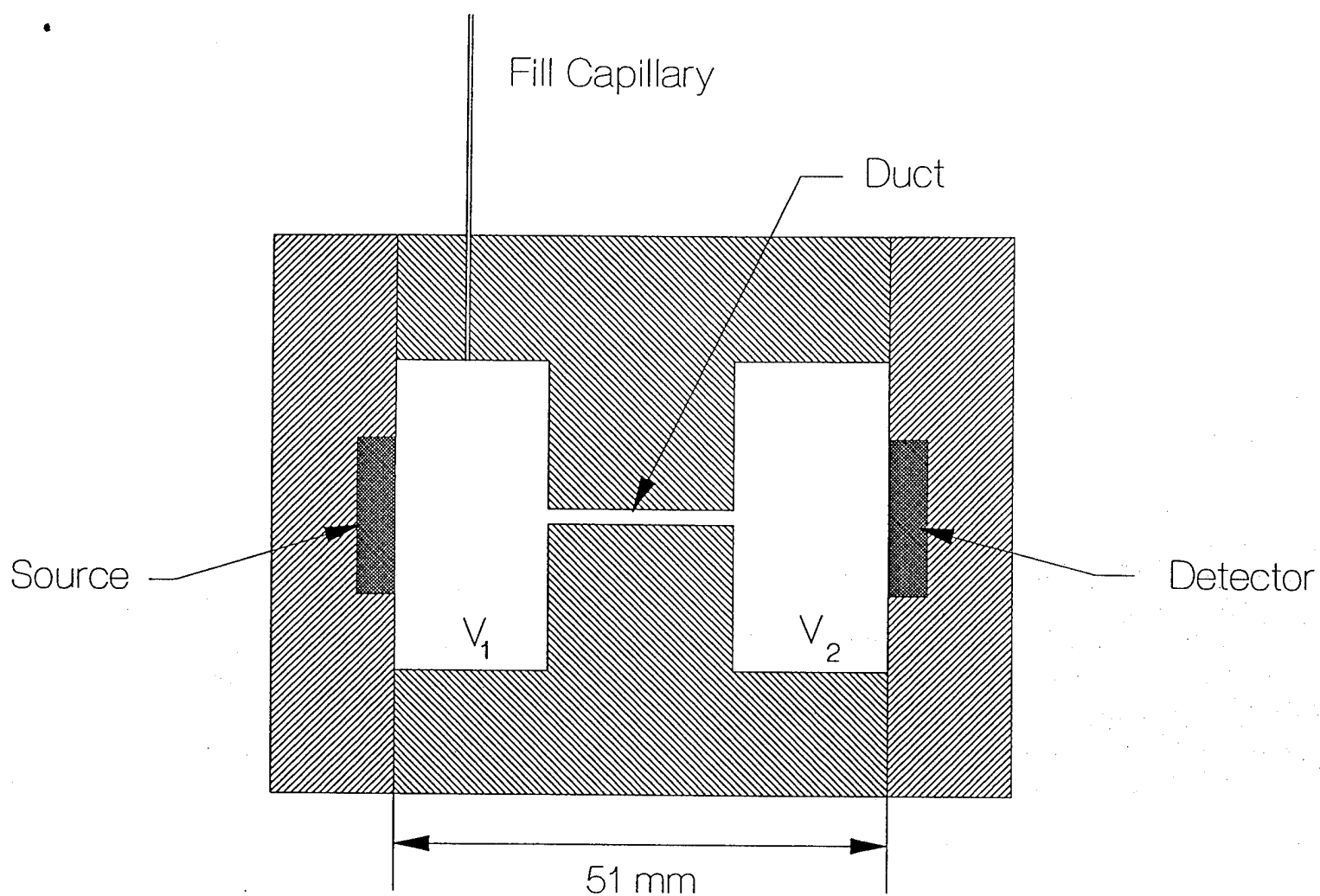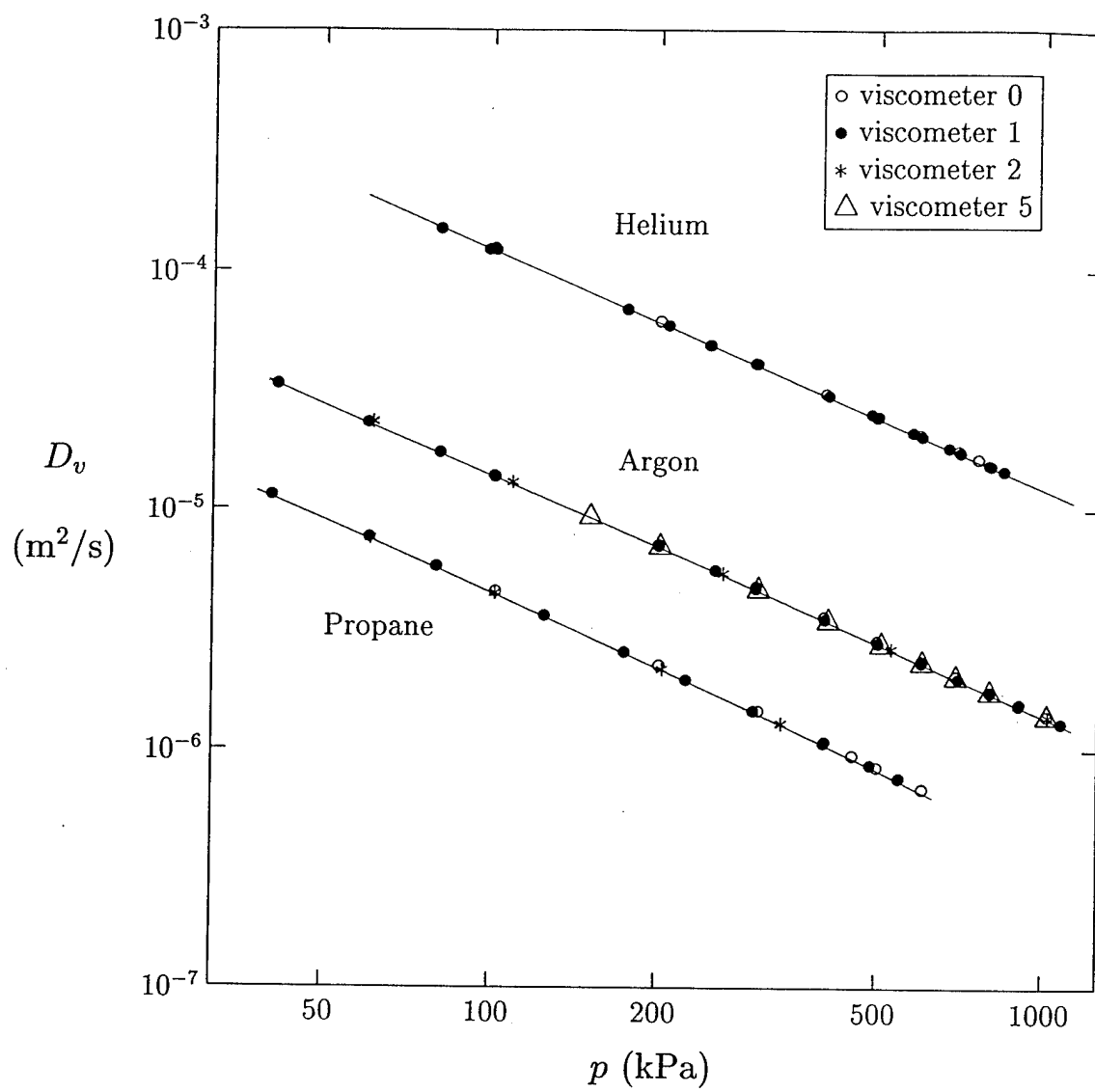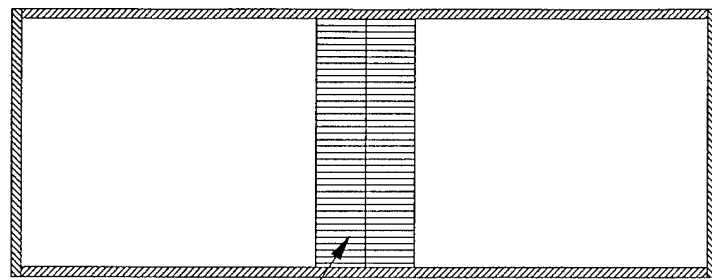
Fill Capillary

Duct

Source

Detector

V_1

V_2

51 mm

Fig 1

Fig. 2

Honeycomb Insert
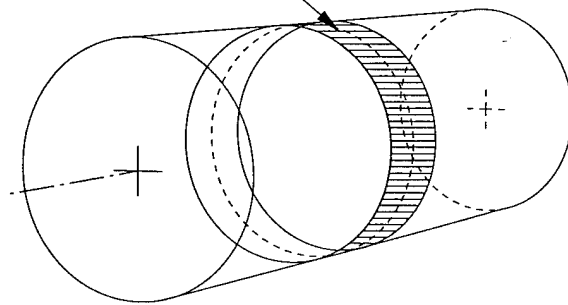
Fig. 3
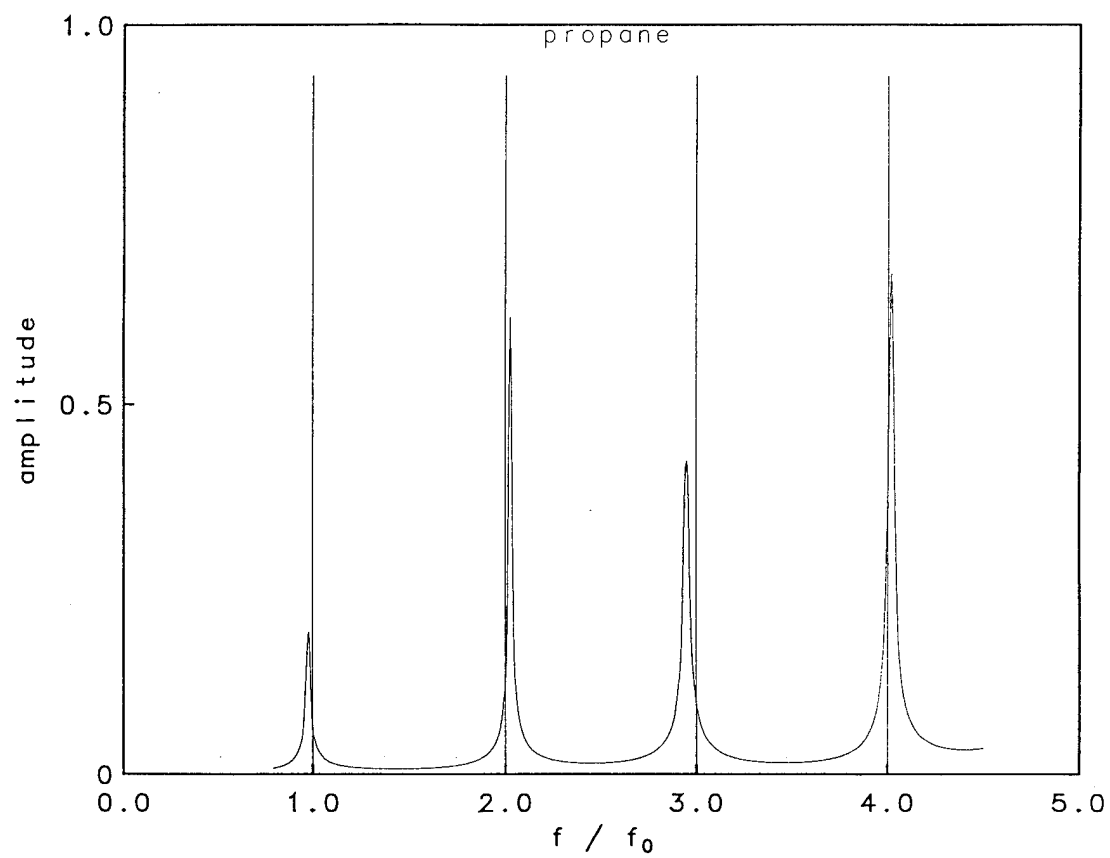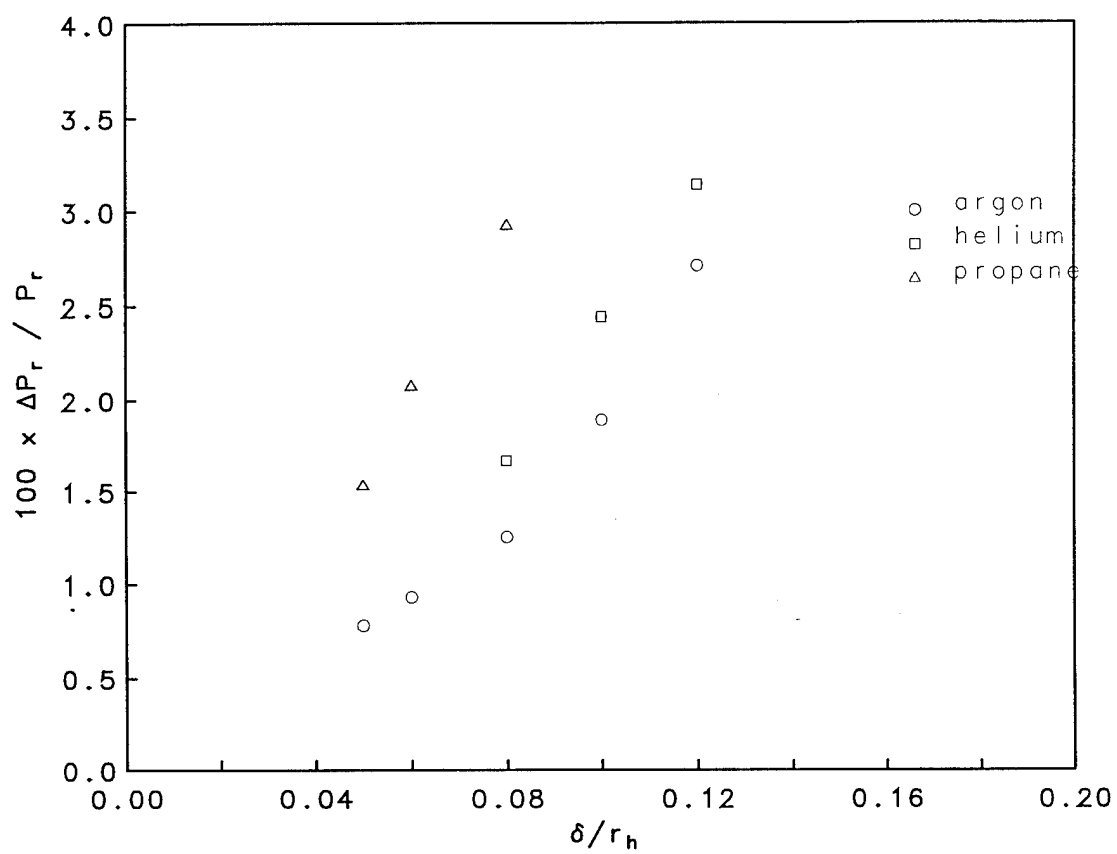
propane

Fig 4

Fig. 5

R&T Number:

Contract/Grant Number: G N00014-93-F-0101

Contract/Grant Title: Properties of Working Fluids for Thermoacoustic Refrigerators

Principal Investigator: M.R. Moldover and K.A. Gillis

Mailing Address: National Institute of Standards and Technology
Building 221, Room A111
Gaithersburg, MD 20899

Phone Number (with Area Code): (301)975-2459; (301)975-2468

E-Mail Address: Moldover@micf.nist.gov; kgillis@nist.gov

a. Number of Papers Submitted to Referred Journal but not yet published: __1__

b. Number of Papers Published in Referred Journals: __1__
   (list attached)

c. Number of Books or Chapters Submitted but not yet Published: __0__

d. Number of Books or Chapters Published: __0__
   (list attached)

e. Number of Printed Technical Report & Non-Referred Papers: __0__
   (list attached)

f. Number of Patents Filed: __0__

g. Number of Patents Granted: __0__
   (list attached)

h. Number of Invited Presentations at Workshops or Prof. Society Meetings: __0__

i. Number of Presentation at Workshop or Prof. Society Meetings: __3__

j. Honors/Awards/Prizes for Contract/Grant Employees: 1
   (list attached, this might Include Scientific Soc. Awards/Offices,
   Promotions, Faculty Award/Offices etc.)

k. Total number of Graduate Students and Post-Docs Supported at least 25%, this
   year on this contract,grant:
   Grad Students __0__ and Post Docs __0__

	[Grad Student Female	__0__
	] [	
How many of each are females or minorities?	] [Grad Student Minority	__0__
(These 6 numbers are for ONR's EEO/Minority	] [	
Reports; minorities Include Blacks, Aleuts	] [Grad Student Asian e/n	__0__
Amindians, etc and those of Hispanic or	] [	
Asian extraction/nationality. This Asians	] [Post-Doc Female	__0__
are singled out to facilitate meeting the	] [	
varying report semantics re "under-	] [Post-Doc Minority	__0__
represented")	] [	
	] [Post-Doc Asian e/n	__0__

IV. Publication/Patents/Presentation/Honors Report (continued)

Publication list

1.   R.A. Aziz, A.R. Janzen, and M.R. Moldover, "*Ab Initio* Calculations for Helium: a Standard for Transport Property Measurements," Phys. Rev. Lett. **74**, 1586 (1995).

List of Honors/Awards/Prizes

1.   M.R. Moldover, NIST Fellow

V. Appendices

Progress Report – Burnett $P\rho T$ Data
By James W. Schmidt

I. Results and Preliminary Analysis.

Vapor–phase $P\rho T$ measurements were made on helium, xenon, and mixtures of helium + xenon with the nominal compositions (expressed as mole fractions He/Xe) 75/25, 50/50, and 25/75. The Thermophysics Division Burnett apparatus was used for measurements which span a temperature range 273K to 373K, and a pressure range 0.5 to 5.0 MPa. Five isochors from each samples produced data, that can be represented by virial equations of the following form:

$$P(\rho,T) = RT\rho \left[1 + B(T)\rho + C(T)\rho^2 + D(T)\rho^3 + E(T)\rho^4 \right] \qquad , \quad \text{Eq. (1)}$$

where P is the pressure, $R = 8.314510$ J/mol·K is the universal gas constant, T is the kelvin temperature, and ρ is the molar density. The virial coefficients $B(T)$, $C(T)$, $D(T)$ and $E(T)$ were fitted to polynomial functions of the temperature of the forms:

$$
\begin{aligned}
B(T) &= b_0 + b_1/T + b_2/T^2 \\
C(T) &= c_0 + c_1/T \\
D(T) &= d_0 + d_1/T \\
E(T) &= e_0
\end{aligned}
\qquad . \qquad \text{Eq. (2)}
$$

where the b_i, c_i, d_i, and e_i, were the fitting parameters. Three parameters in addition to a run constant were used to fit the $P\rho T$ surface of pure helium. Five parameters in addition to a run constant were used to fit the $P\rho T$ surface for the 75/25 and 50/50 He/Xe mixtures. Seven parameters in addition to a run constant were used to fit the $P\rho T$ surface for the 25/75 He/Xe mixture. Eight parameters in addition to a run constant were used to fit the $P\rho T$ surface for xenon. Values for these parameters are given in Tables I(a–e).

Figures 1(a–e) show the deviations of the measured pressures from the fitted surfaces given by Eqs. 1–2 and Tables I(a–e). Tables II(a–e) give the $P\rho T$ data and their deviations from the fitted surface.

II. Materials and Handling

The mixtures were obtained from Matheson Gas Products.[1] A gas chromatograph indicated that the samples had a purity of approximately 99.994%. The mixtures were used without further purification. After the measurements with the Burnett apparatus were completed, some of the used sample was collected and reanalyzed with the gas chromatograph. No additional impurities were detected. The compositions of the three mixtures were analyzed by John Hurly via sound speed measurements. His analysis indicated compositions of 74.132/25.868, 47.331/52.669, and 20.129/79.871.

III. Future Analysis.

The present representation of the data uses 33 parameters of which 5 are "run" parameters that are not listed below and the remaining 28 are "thermodynamic" parameters. We will reanalyze all of the data applying physically reasonable constraints and including the low–temperature speed–of–sound data that we are now acquiring.

The reanalysis of the Burnett data will use the constraints: 1. Two run constants will be used instead of five run constants. One run constant will be used for the pure xenon data and the second will be used for the rest of the data. The apparatus was overhauled between the acquisition of the xenon data and the acquisition of the rest of the data requiring the introduction of a second run constant. 2. The values of $B_{he}(T)$ and $B_{xe}(T)$ are known very well from other experiments and from *ab initio* calculations. Thus, information from the literature will replace the five fitted parameters that represent $B_{he}(T)$ and $B_{xe}(T)$. 3. For binary mixtures, $B(T)$ has the functional form

$$B(T)_{mix} = B_{he}(T)x_{he}^2 + B_{hexe}(T)x_{he}x_{xe} + B_{xe}(T)x_{xe}^2 \quad .$$

Thus, a single the function $B_{hexe}(T)$ using 2 or 3 parameters will replace the 9 parameters used to represent the three functions $B(T)$ for the three mixtures. 4. For binary mixtures, $C(T)$ has the functional form

$$C(T)_{mix} = C_{he}(T)x_{he}^3 + C_{hehexe}(T)x_{he}^2x_{xe} + C_{hexexe}(T)x_{he}x_{xe}^2 + C_{xe}(T)x_{xe}^3.$$

Thus, two functions $C_{hehexe}(T)$ and $C_{hexexe}(T)$ will replace the three functions $C(T)$ for the three mixtures. This change will replace 6 parameters with either 3 or 4 parameters. In summary, 28 thermodynamic parameters will be replaced with 13 to 15 parameters.

---

[1]In order to describe materials and experimental procedures adequately, it is occasionally necessary to identify commercial products by manufacturer's names or labels. In no instance does such identification imply endorsement by NIST, nor does it imply that the particular product or equipment is necessarily the best available for the purpose.

Table I(a). **Fitting parameters** Helium

	b_0, c_0	b_1
$B(T)/(\text{mol/L})$	$1.10743{\times}10^{-2}$	0.190775 K
$C(T)/(\text{mol/L})^2$	$8.16508{\times}10^{-2}$	

Table I(b). **Fitting parameters** He/Xe 75/25

	b_0, c_0	b_1, c_1	b_2
$B(T)/(\text{mol/L})$	$2.00409{\times}10^{-2}$	$5.45926{\times}10^{-2}$ K	$1.04332{\times}10^{4}$ K^2
$C(T)/(\text{mol/L})^2$	$-1.68418{\times}10^{-3}$	0.663494 K	

Table I(c). **Fitting parameters** He/Xe 50/50

	b_0, c_0	b_1, c_1	b_2
$B(T)/(\text{mol/L})$	$3.10923{\times}10^{-2}$	-6.79584 K	$-2.41985{\times}10^{4}$ K^2
$C(T)/(\text{mol/L})^2$	$-1.55805{\times}10^{-3}$	0.847894 K	

Table I(d). **Fitting parameters** He/Xe 25/75

	b_0, c_0, d_0	b_1, c_1, d_0	b_2
$B(T)/(\text{mol/L})$	$4.84516{\times}10^{-2}$	-19.3586 K	$-4.98942{\times}10^{3}$ K^2
$C(T)/(\text{mol/L})^2$	$-1.92411{\times}10^{-2}$	6.80292 K	
$D(T)/(\text{mol/L})^3$	$7.50388{\times}10^{-3}$	-2.34137 K	

Table I(e). **Fitting parameters** Xenon

	b_0, c_0, d_0, e_0	b_1, c_1, d_1	b_2
$B(T)/(\text{mol/L})$	$2.43224{\times}10^{-2}$	-15.8491 K	$-8.42082{\times}10^{3}$ K^2
$C(T)/(\text{mol/L})^2$	$2.53341{\times}10^{-4}$	-1.62404 K	
$D(T)/(\text{mol/L})^3$	$4.03573{\times}10^{-3}$	1.04594 K	
$E(T)/(\text{mol/L})^4$	$-1.90974{\times}10^{-3}$		

Table II α

Vapor Phase PVT data   - Helium

	Temp/C	Press/MPa	density/(mol/L)	((P-Pfit)/P) x100%
1	0.001	3.41262	1.47681	-0.008
2	19.963	3.65913	1.47557	0.005
3	40.010	3.90600	1.47432	0.010
4	60.017	4.15172	1.47308	0.009
5	79.991	4.39633	1.47185	0.001
6	100.000	4.64083	1.47060	-0.007
7	99.991	4.64093	1.47060	-0.003
8	99.991	4.64092	1.47060	-0.003
9	99.994	4.64095	1.47060	-0.003
10	100.002	2.58603	0.82557	0.000
11	100.002	2.58605	0.82557	0.001
12	0.046	1.90143	0.82905	-0.012
13	19.964	2.03852	0.82835	0.001
14	40.008	2.17609	0.82766	0.005
15	59.969	2.31280	0.82696	0.007
16	79.997	2.44962	0.82626	0.004
17	99.977	2.58567	0.82557	-0.007
18	99.969	2.58587	0.82557	0.003
19	99.969	2.58589	0.82557	0.003
20	99.968	1.44555	0.46346	0.002
21	99.968	1.44556	0.46346	0.002
22	0.042	1.06279	0.46541	-0.017
23	19.962	1.13942	0.46502	-0.007
24	40.009	1.21636	0.46463	-0.001
25	59.972	1.29279	0.46424	-0.001
26	79.997	1.36934	0.46385	0.001
27	100.017	1.44575	0.46346	0.003
28	100.006	1.44571	0.46346	0.003
29	100.006	1.44565	0.46346	-0.001
30	100.006	0.80964	0.26017	-0.002
31	100.006	0.80963	0.26017	-0.003
32	0.045	0.59527	0.26127	-0.005
33	20.008	0.63819	0.26105	-0.010
34	40.000	0.68122	0.26083	0.003
35	40.001	0.68121	0.26083	0.001
36	59.969	0.72399	0.26061	-0.004
37	79.994	0.76689	0.26039	0.000
38	99.974	0.80957	0.26017	-0.002
39	99.966	0.80955	0.26017	-0.003
40	99.966	0.80955	0.26017	-0.003
41	99.966	0.45389	0.14606	0.003
42	99.966	0.45388	0.14606	0.000
43	0.029	0.33380	0.14667	0.025
44	19.999	0.35791	0.14655	0.026
45	39.999	0.38201	0.14643	0.028
46	60.006	0.40590	0.14630	-0.014
47	79.980	0.42990	0.14618	-0.007
48	100.001	0.45394	0.14606	0.004
49	99.988	0.45393	0.14606	0.006
50	99.988	0.45398	0.14606	0.017
51	99.990	0.25457	0.08199	-0.022

Table II b

Vapor Phase PVT data   - He-Xe 75/25

	Temp/C	Press/MPa	density/(mol/L)	((P-Pfit)/P) x100%
1	0.033	3.47048	1.51108	-0.002
2	19.998	3.72982	1.50981	0.001
3	39.993	3.98834	1.50854	0.001
4	39.995	3.98837	1.50854	0.001
5	59.928	4.24504	1.50728	-0.001
6	79.980	4.50231	1.50600	-0.004
7	100.010	4.75877	1.50473	-0.001
8	99.994	4.75868	1.50473	0.001
9	99.993	4.75874	1.50473	0.003
10	99.993	4.75874	1.50473	0.003
11	99.996	2.64899	0.84473	-0.003
12	99.996	2.64902	0.84473	-0.002
13	0.032	1.93808	0.84829	0.002
14	39.984	2.22357	0.84686	0.006
15	19.988	2.08088	0.84758	0.003
16	59.959	2.36537	0.84615	-0.004
17	79.977	2.50728	0.84544	-0.007
18	100.007	2.64891	0.84473	-0.009
19	100.002	2.64912	0.84473	0.001
20	100.002	2.64912	0.84473	0.001
21	100.005	1.48021	0.47421	0.002
22	100.005	1.48020	0.47421	0.002
23	0.030	1.08506	0.47621	0.001
24	19.998	1.16437	0.47581	0.002
25	39.993	1.24359	0.47541	0.003
26	59.954	1.32247	0.47501	0.002
27	79.980	1.40147	0.47461	0.006
28	99.955	1.48003	0.47421	0.004
29	100.002	1.48022	0.47421	0.004
30	100.000	1.48021	0.47421	0.004
31	100.000	1.48017	0.47421	0.001
32	99.998	0.82875	0.26621	0.002
33	99.998	0.82874	0.26621	0.001
34	0.028	0.60817	0.26734	-0.014
35	19.995	0.65234	0.26711	-0.021
36	39.987	0.69658	0.26689	-0.010
37	59.933	0.74069	0.26666	0.007
38	79.976	0.78485	0.26644	0.012
39	100.004	0.82886	0.26621	0.014
40	99.998	0.82877	0.26621	0.004
41	99.998	0.82871	0.26621	-0.003
42	99.999	0.46455	0.14945	0.002
43	99.999	0.46454	0.14945	0.000
44	0.023	0.34108	0.15008	-0.032
45	19.992	0.36581	0.14995	-0.031
46	39.984	0.39057	0.14982	-0.019
47	59.961	0.41519	0.14970	-0.023
48	79.993	0.44000	0.14957	0.010
49	99.966	0.46459	0.14945	0.019
50	99.957	0.46453	0.14945	0.008
51	99.957	0.46446	0.14945	-0.008
52	99.957	0.26049	0.08390	-0.019

Table II c
Vapor Phase PVT data   - He-Xe 50/50

|	Temp/C	Press/MPa	density/(mol/L)	((P-Pfit)/P) x100%
1	99.952	4.90697	1.59025	0.004
2	99.955	4.90702	1.59025	0.004
3	99.955	4.90683	1.59025	0.000
4	0.033	3.48965	1.59695	-0.004
5	19.997	3.77671	1.59561	0.001
6	39.991	4.06198	1.59427	0.004
7	59.958	4.34452	1.59293	-0.005
8	79.974	4.62660	1.59159	-0.003
9	99.959	4.90672	1.59025	-0.003
10	99.957	4.90691	1.59025	0.001
11	99.957	4.90695	1.59025	0.002
12	99.958	2.75979	0.89273	-0.004
13	99.958	2.75983	0.89273	-0.002
14	0.037	1.99116	0.89650	0.008
15	20.003	2.14622	0.89574	0.008
16	39.995	2.30074	0.89499	0.010
17	59.962	2.45412	0.89424	0.002
18	79.984	2.60725	0.89349	-0.008
19	100.020	2.76008	0.89273	-0.010
20	100.006	2.76018	0.89273	-0.003
21	100.006	2.76022	0.89273	-0.001
22	100.003	1.55177	0.50116	0.007
23	100.003	1.55190	0.50116	0.015
24	0.034	1.12839	0.50327	-0.010
25	19.997	1.21353	0.50285	-0.004
26	39.992	1.29847	0.50243	0.000
27	59.956	1.38280	0.50201	-0.011
28	79.973	1.46739	0.50158	-0.001
29	100.005	1.55147	0.50116	-0.013
30	99.988	1.55172	0.50116	0.007
31	99.988	1.55174	0.50116	0.009
32	99.991	0.87191	0.28134	0.012
33	99.991	0.87190	0.28134	0.011
34	0.029	0.63689	0.28253	-0.024
35	19.997	0.68408	0.28229	-0.016
36	39.990	0.73120	0.28205	-0.008
37	60.007	0.77825	0.28182	-0.001
38	79.982	0.82507	0.28158	0.003
39	100.016	0.87186	0.28134	0.000
40	100.010	0.87196	0.28134	0.014
41	100.010	0.87194	0.28134	0.011
42	100.006	0.48973	0.15794	0.010
43	100.006	0.48970	0.15794	0.003
44	0.033	0.35857	0.15861	-0.055
45	20.000	0.38488	0.15847	-0.039
46	39.995	0.41119	0.15834	-0.020
47	60.001	0.43750	0.15821	0.008
48	79.983	0.46362	0.15807	0.010
49	100.015	0.48969	0.15794	-0.001
50	100.014	0.48975	0.15794	0.012
51	100.014	0.48973	0.15794	0.007
52	100.009	0.27496	0.08866	-0.008

Table II d

Vapor Phase PVT data   - He-Xe 25/75

	Temp/C	Press/MPa	density/(mol/L)	((P-Pfit)/P) x100%
1	100.009	4.21332	1.43677	0.001
2	100.009	4.21331	1.43677	0.001
3	100.008	4.21320	1.43677	-0.002
4	-0.012	2.88250	1.44283	-0.004
5	19.995	3.15459	1.44162	0.005
6	39.992	3.42298	1.44040	0.005
7	60.010	3.68858	1.43919	-0.004
8	79.971	3.95124	1.43798	-0.007
9	99.992	4.21297	1.43677	-0.002
10	99.988	4.21310	1.43677	0.002
11	99.988	4.21313	1.43677	0.003
12	99.988	4.21313	1.43677	0.003
13	99.984	2.42309	0.80657	0.002
14	0.032	1.71248	0.80997	-0.002
15	19.996	1.85639	0.80929	0.000
16	39.994	1.99942	0.80861	0.001
17	60.039	2.14174	0.80793	-0.002
18	79.978	2.28249	0.80725	-0.002
19	99.959	2.42271	0.80657	-0.007
20	99.955	2.42295	0.80657	0.004
21	99.955	2.42299	0.80657	0.006
22	99.957	1.37953	0.45279	-0.001
23	99.957	1.37951	0.45279	-0.003
24	-0.017	0.99190	0.45470	0.011
25	39.994	1.14807	0.45394	0.003
26	59.988	1.22557	0.45356	0.003
27	79.976	1.30273	0.45317	0.002
28	99.992	1.37962	0.45279	-0.004
29	99.994	1.37965	0.45279	-0.003
30	99.991	1.37968	0.45279	0.000
31	99.991	1.37967	0.45279	-0.001
32	99.995	0.78080	0.25419	0.011
33	-0.021	0.56668	0.25526	0.001
34	19.997	0.60984	0.25505	0.006
35	39.997	0.65279	0.25483	0.008
36	59.946	0.69531	0.25462	-0.017
37	79.994	0.73808	0.25440	-0.014
38	99.959	0.78052	0.25419	-0.016
39	99.949	0.78069	0.25419	0.009
40	99.949	0.78063	0.25419	0.001
41	99.948	0.44028	0.14270	0.023
42	99.948	0.44023	0.14270	0.013
43	0.034	0.32122	0.14330	-0.044
44	19.998	0.34508	0.14318	-0.042
45	39.997	0.36901	0.14306	-0.016
46	59.959	0.39271	0.14294	-0.023
47	79.978	0.41652	0.14282	-0.007
48	99.957	0.44015	0.14270	-0.007
49	99.954	0.44029	0.14270	0.024
50	99.954	0.44031	0.14270	0.028
51	99.954	0.44026	0.14270	0.018
52	99.951	0.24775	0.08011	0.011

Table II e

Vapor Phase PVT data   - Xenon - Boyes & Gillis

	Temp/C	Press/MPa	density/(mol/L)	((P-Pfit)/P) x100%
1	0.000	2.75793	1.56662	-0.002
2	0.000	1.73889	0.87911	-0.001
3	0.000	1.03875	0.49331	0.001
4	0.000	0.60306	0.27682	0.009
5	0.000	0.34470	0.15534	-0.005
6	0.000	1.96115	1.01383	0.001
7	0.000	1.18353	0.56891	-0.002
8	0.000	0.69086	0.31924	0.000
9	15.000	1.92238	0.91231	0.001
10	15.000	1.14298	0.51194	0.003
11	15.000	0.66193	0.28727	-0.003
12	15.000	0.37788	0.16120	-0.018
13	15.000	2.50226	1.24772	0.001
14	15.000	1.52152	0.70016	0.000
15	15.000	0.89205	0.39289	-0.001
16	15.000	2.57276	1.29120	0.002
17	15.000	1.56900	0.72456	0.000
18	15.000	0.92134	0.40658	-0.003
19	15.000	2.87987	1.48891	0.003
20	15.000	1.78032	0.83550	-0.002
21	15.000	1.05309	0.46884	-0.005
22	15.000	0.60826	0.26309	0.001
23	30.000	3.14773	1.51784	0.000
24	30.000	1.92796	0.85173	-0.001
25	30.000	1.13528	0.47795	-0.001
26	30.000	0.65421	0.26820	0.006
27	30.000	0.37248	0.15050	0.000
28	30.000	2.79694	1.31248	-0.005
29	30.000	1.69227	0.73649	0.002
30	30.000	0.98983	0.41328	0.003
31	30.000	0.56827	0.23191	0.008
32	30.000	1.54660	0.66711	-0.001
33	30.000	0.90099	0.37435	0.001
34	30.000	0.51612	0.21006	0.006
35	30.000	0.29287	0.11788	-0.013
36	85.000	3.35255	1.25848	0.000
37	85.000	1.97557	0.70620	0.003
38	85.000	1.13964	0.39628	-0.006
39	85.000	0.64950	0.22237	0.001
40	85.000	0.36761	0.12478	0.003
41	85.000	3.01369	1.11733	0.000
42	85.000	1.76641	0.62699	0.001
43	85.000	1.01586	0.35183	-0.003
44	85.000	0.57793	0.19743	0.002
45	85.000	0.32678	0.11079	0.004

Fig 1

Helium

$(P_{meas} - P_{fit})/Pa$

Temp/C

Fig 16

He-Xe 50/50

Temp/C

$(P_{meas} - P_{fit})/Pa$
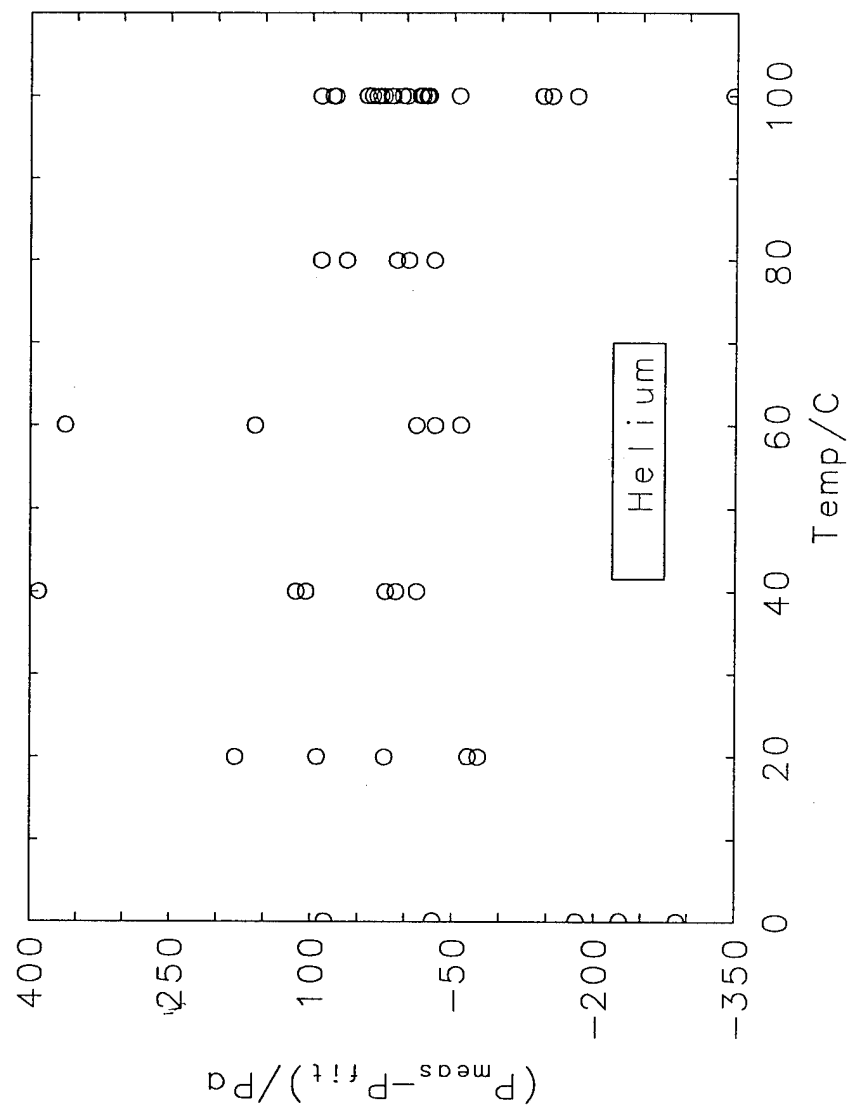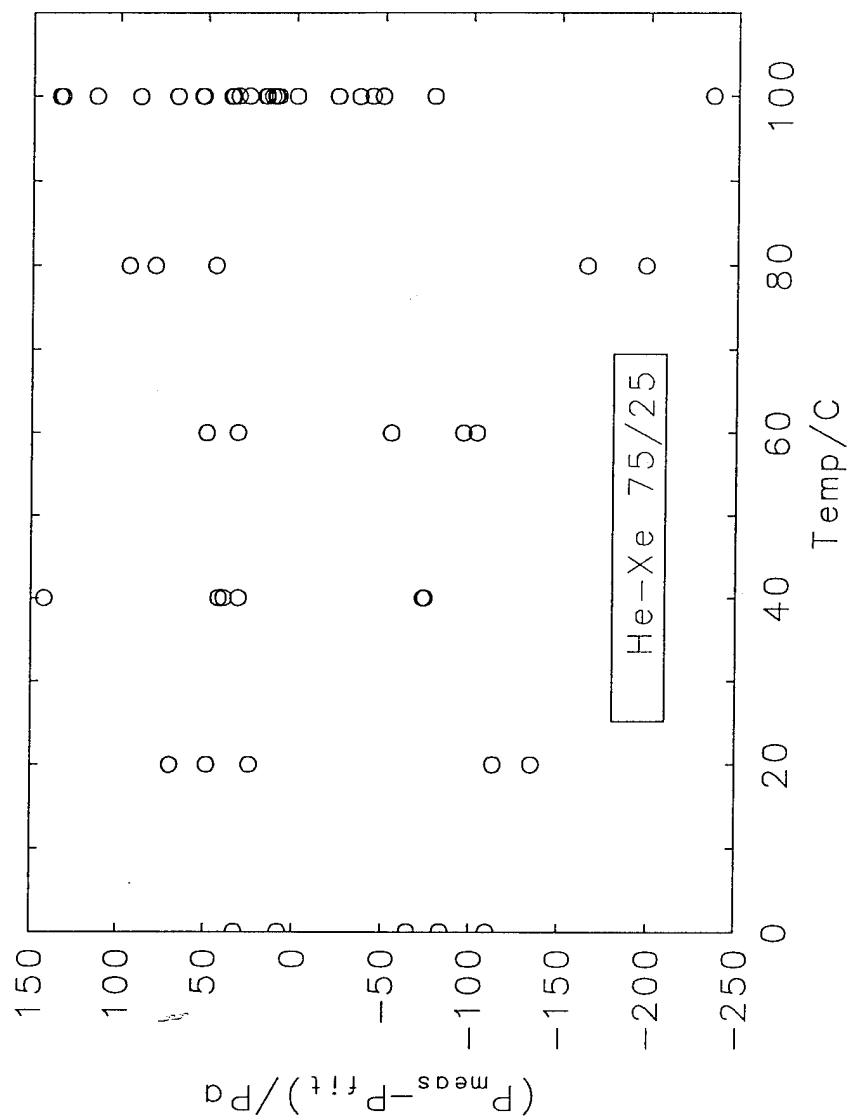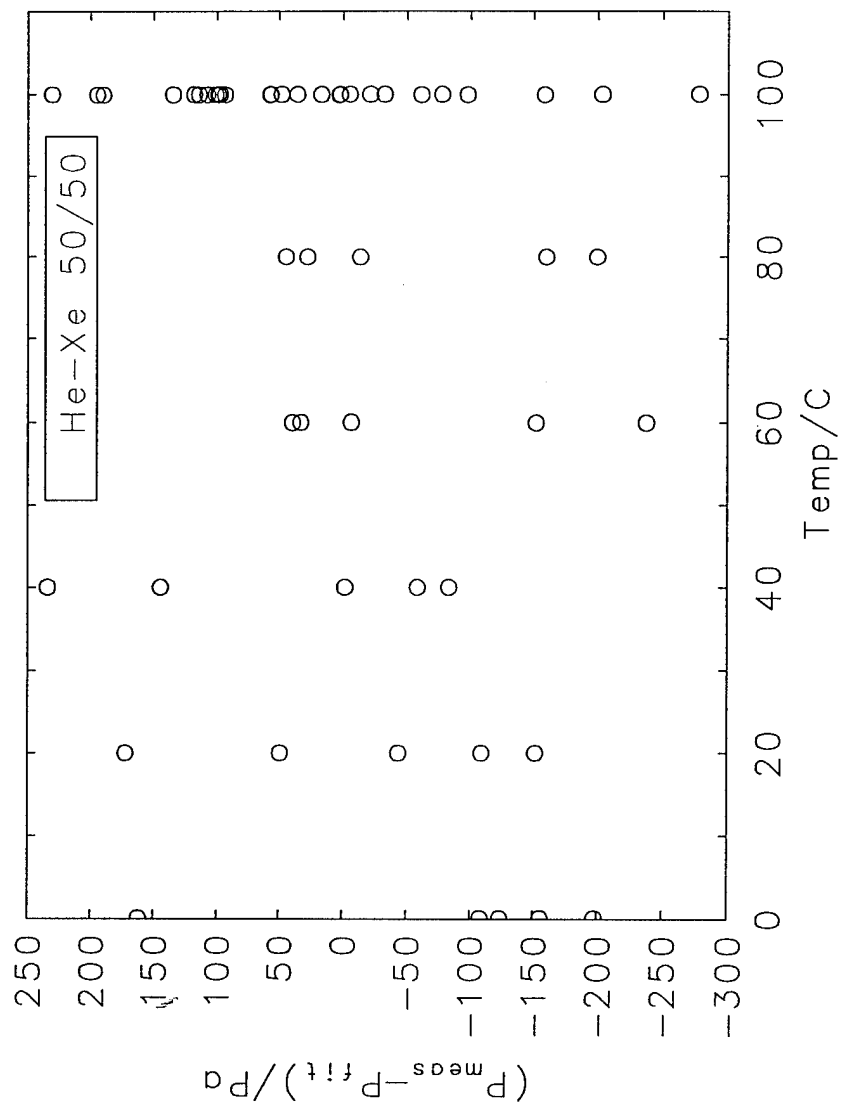
Fig. 1c
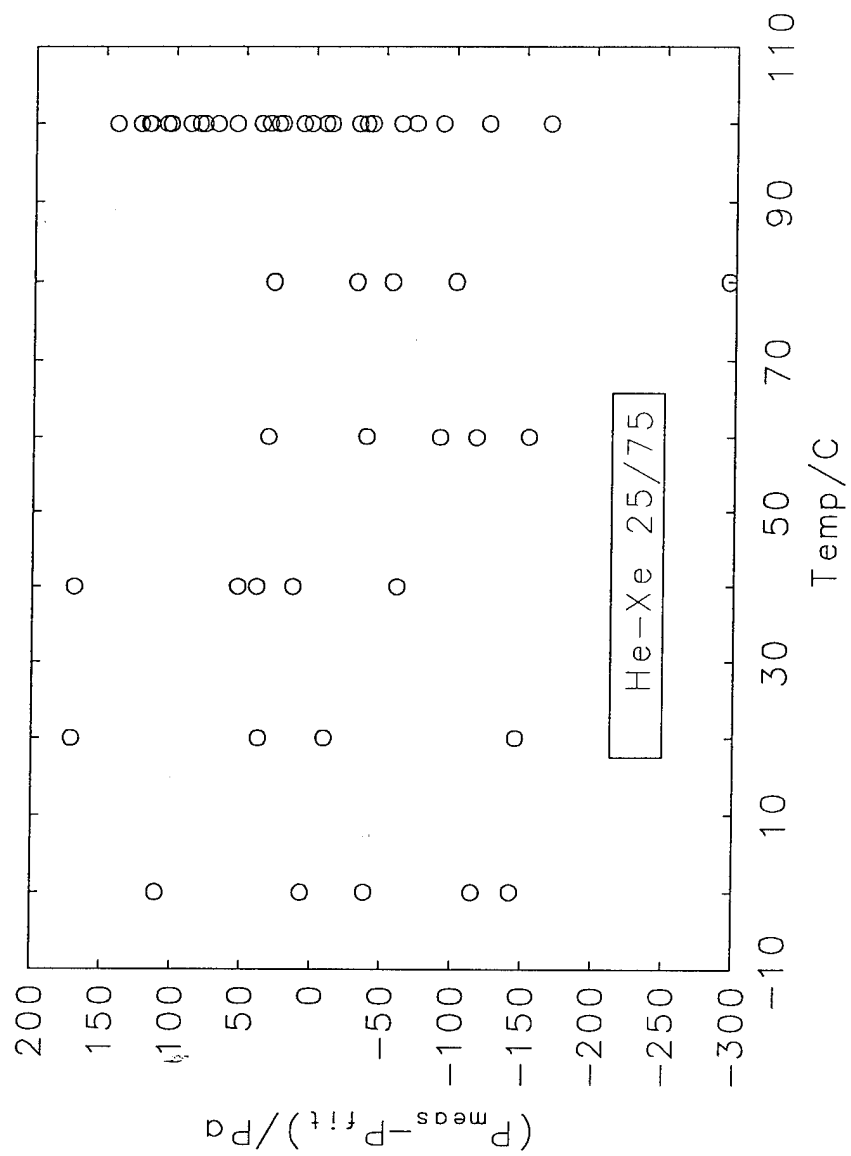
Fig 1d
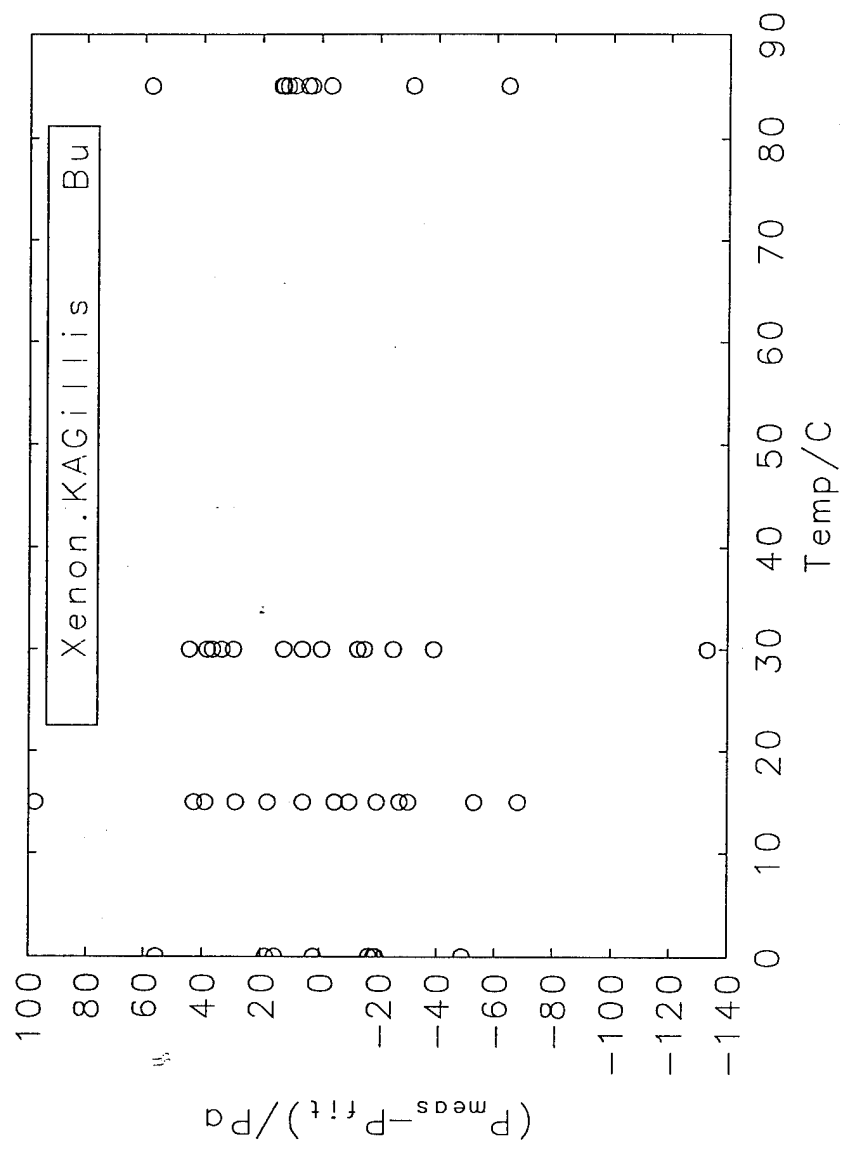
Fig 1e

July 11, 1995

Greenspan acoustic viscometer for gases

K. A. Gillis, J.B. Mehl, and M.R. Moldover

Thermophysics Division, National Institute of Standards and Technology, Gaithersburg MD 20899

Double Helmholtz acoustic resonators, first proposed by Greenspan for measuring the viscosity of gases, were tested with helium, argon, and propane. Two different resonators were tested extensively with all three gases. For each of these instruments, the results for the viscosities of the three gases were consistent within ± 0.5 % at pressures spanning the range 25 kPa - 1000 kPa. Without calibration, the viscosities deduced from one viscometer were systematically 1% larger than data from the literature; the viscosities from the second viscometer were systematically 3% larger than data from the literature. If the systematic differences were removed for each viscometer by calibration with a single gas at a single temperature and pressure, then nearly all the results for both instruments would have fallen within ± 0.5% of the data from the literature. In these viscometers, the test gases are in contact with robust metal parts only; thus, these instruments are applicable to a very wide variety of gases over a very wide range of temperatures.

I. INTRODUCTION

Double Helmholtz acoustic resonators can be designed to have large viscous losses in the duct connecting the two chambers. (See Fig. 1.) When this is done, the frequency response of these resonators becomes a sensitive function of the viscosity of the gas within the resonator. We call such resonators "Greenspan viscometers" in honor of Greenspan's conception of this method of measuring the viscosity of a gas[1].

In 1953, Greenspan and Wimenitz[1] tested double Helmholtz acoustic resonators as viscometers. Their results for the kinematic viscosity of air differed from the literature values by as much as 38% and they concluded "the method described does not at present offer a satisfactory basis for an instrument for the measurement of viscosity." In this work, we revisit the method using improved instrumentation, modeling, and control of the properties of the test gases. We now conclude that with calibration, the method is capable of yielding state-of-the art results under a wide range of conditions. We suggest that further study of the method is warranted for developing a primary standard Greenspan viscometer. Such a standard would be a robust instrument that could be used to check the oscillating disk viscometer that is now used as a standard.

Our optimism is based on measurements of the frequency responses of four Greenspan viscometers, each tested with three gases (helium, argon, and propane) at pressures spanning the range 25 kPa - 1000 kPa. Although all of the data were taken at ambient temperature (22° C), they span a factor of 350 in viscous diffusivity. This range 7×10^{-7} m$^2 \cdot$s$^{-1} < D_\mathrm{v} < 2 \times 10^{-4}$ m$^2 \cdot$s^{-1} is displayed graphically in Fig 2. (Here, $D_\mathrm{v} \equiv \eta/\rho$, where η is the viscosity and ρ is the mass density.)

Of the four Greenspan viscometers, two were studied more extensively than the others. One, designated "viscometer 1" was the "best." The other, designated "viscometer 0" was the "worst." The dimensions of these viscometers were accurately determined with a coordinate measuring machine. Thus, the viscosity could be deduced from these two viscometers without calibration. For each of these viscometers, the viscosities of all three

2

gases were consistent within ± 0.5 % except at the very lowest pressures. Without calibration, the viscosities from viscometer 1 were systematically 1% larger than data from the literature; the viscosities from viscometer 0 were systematically 3% larger than data from the literature. If the systematic differences were removed by calibration of each viscometer with a single gas at a single temperature and a single pressure above 100 kPa, then nearly all the results for both instruments would have fallen within ± 0.5% of the data from the literature.

To put the performance of these Greenspan viscometers in perspective, we note that an uncertainty of ± 1 % is near the state of the art in gas viscometry. In a recent publication based on *ab initio* calculations for helium, Aziz *et al.*[2] argued that the viscosity of helium as determined by the best measurement to date was systematically in error by 0.3%. The inconsistencies among gas viscometers from various laboratories are usually much larger than 0.3%.

In the Greenspan viscometer, an acoustic transducer coupled to the chamber V_1 forces the test gas to oscillate through a duct leading to a second chamber V_2. The oscillations are driven at frequencies near the Helmholtz resonance, which, in the lowest approximation is:

$$\omega_0^2 = \frac{c_0^2 A_d}{L_d} \left[\frac{1}{V_1} + \frac{1}{V_2} \right] \quad .$$

(1)

Here, c_0 is the speed of sound in the gas, A_d is the cross sectional area of the duct, and L_d is the length of the duct. In the instruments described here, $f_0 = \omega_0/(2\pi)$ falls in the range 100 Hz $\leq f_0 \leq$ 200 Hz when $c_0 \approx$ 300 m/s. This frequency range is a factor of 10 to 100 below the frequencies of other resonances that might complicate the analysis of the frequency response data; other resonances include acoustic resonances of the gas in the chambers, mechanical resonances in the transducers, and resonances in the mechanical structure of the Greenspan viscometer itself.

Most of the viscous dissipation occurs within the duct where the velocity of the gas is

highest. Thus, the duct in the oscillating flow of the Greenspan viscometer plays a role analogous to that of the capillary tube in the unidirectional flow of the familiar Ubbelohde or Cannon-Fenske viscometers[3]. In particular, the duct's dimensions must be well known; the duct must be kept clean, and the effects of converging and diverging flows near the ends of the duct must be accounted for in the analysis of the data.

The viscosity is deduced from measurements of the frequency dependence of the acoustic pressure detected by an acoustic transducer coupled to the chamber V_2 as the frequency of the acoustic source in V_1 is scanned through the Helmholtz resonance. (See Fig. 3.) Thus, the frequency responses of the electroacoustic transducers must be linear (or known) in the frequency range of interest. However, the transducers need not be calibrated. Indeed, they need not be stable for intervals longer than the minute or so required to measure the viscosity at a given temperature and pressure. In contrast, the differential pressure transducers used to determine the viscosity in unidirectional flow viscometers must be stable and calibrated.

To date, our experience indicates that the Greenspan viscometer operates well with Qs of 10 or larger. (When the losses are not too large, the amplitude–vs–frequency response function is approximately Lorentzian. The Q is defined as $f_0 \, / \, (2g)$, where $2g$ is the full resonance width at $1/\sqrt{2}$ of the maximum amplitude.) Thus, the transducers need to be characterized over a comparatively narrow frequency range. This easy-to-meet requirement together with the small values of f_0 will facilitate the operation of future Greenspan viscometers with remote acoustic transducers coupled to the test gas *via* acoustic wave guides and diaphragms such as those described by Gillis *et al*[4].

Below, we provide a heuristic model useful for designing and understanding the operation of the viscometer. We report the results of a more detailed model that will be described elsewhere. We shall describe the test viscometers, the measurement procedures, and the test results. We conclude by discussing the potential for developing the Greenspan viscometer into a primary standard viscometer for gases.

4

II. HEURISTIC MODEL.

Here, we present a simple model for the Greenspan viscometer that is useful for insight and design purposes, but not for the most accurate analysis of data. When this model is applicable, the resonance frequency of the double Helmholtz resonator is simply related to the speed of sound in the test gas and the half-width of the resonance is simply related to the viscosity of the test gas. The model is approximately correct for the experimentally important conditions in which both the viscous penetration length δ_v and the thermal penetration length δ_t are much smaller than the radius of the duct r_d. The penetration lengths are given by the relations:

$$\delta_v \equiv \sqrt{2\eta/\rho\omega} \tag{2}$$

and

$$\delta_t \equiv \sqrt{2\lambda/\rho C_p\omega} \quad . \tag{3}$$

Here, λ is the thermal conductivity of the gas and ρC_p is the constant-pressure heat-capacity per unit volume of the gas.

We note that thermal effects within the duct are small because the acoustic temperature has a node in the duct that corresponds to the velocity antinode there. In some geometries, the thermal losses may be important; the detailed acoustic model shows this quantitatively.

In the lowest order approximation, one may consider the gas in the duct to be the inertial element of an oscillator and the pressure difference between the two chambers to provide the stiffness. In the vicinity of the Helmholtz resonance frequency, the duct is much shorter than the wavelength of sound; thus the gas moves uniformly in the duct along its length and the moving mass is $m = \rho A_d L_d$, where ρ is the density of the gas. The stiffness is the restoring force divided by the displacement of the inertial element. If the inertial element is displaced by Δx from chamber V_1 towards chamber V_2, a volume of gas $A_d \Delta x$ is removed from chamber V_1 and injected into chamber V_2. This produces a pressure

5

difference between the chambers given by

$$\Delta p = \frac{A_d \Delta x}{k_s} \left[\frac{1}{V_1} + \frac{1}{V_2} \right] \quad , \tag{4}$$

where $k_s \equiv - (\partial V / \partial p)_s / V$ is the adiabatic compressibility of the gas. The corresponding

stiffness is $\Delta p A_d / \Delta x$; thus, the frequency of the oscillation is given by

$$\omega_0^2 = \frac{stiffness}{mass} = \frac{A_d}{k_s \rho L_d} \left[\frac{1}{V_1} + \frac{1}{V_2} \right] \quad . \tag{5}$$

Eq. (5) leads to Eq. (1) upon substitution of c_0^2 for $1/(k_s \cdot \rho)$.

To estimate the viscous energy loss in the duct, we assume, for simplicity, that the

duct is a circular cylinder with radius r_d. In the limit that $\delta_v \ll r_d$, the velocity of most

of the gas is uniform across the duct. However, in the boundary layer in contact with the

wall of the duct, the acoustic velocity v decays exponentially to zero with the characteristic

length δ_v. For the case of a plane surface with a tangential velocity v far from the surface,

the viscous dissipation rate per unit area is exactly $\frac{1}{2}(\eta / \delta_v) v^2$. Using this result as an

approximation for the cylindrical duct, the ratio of the viscous energy loss per cycle to the

stored energy is

$$\alpha_v = \frac{\frac{1}{2}(\eta / \delta_v) v^2 \cdot 2\pi r_d L_d \cdot (2\pi / \omega)}{\frac{1}{2}\rho v^2 \cdot \pi r_d^2 L_d} = 2\pi \frac{\delta_v}{r_d} \quad . \tag{6}$$

The ratio $\alpha_v \equiv 2\pi / Q_v$ is the most significant contribution to reducing the quality factor Q

of the Helmholtz oscillations.

To estimate the energy dissipated in the thermal boundary layer, we note that, the

temperature oscillates in phase with the pressure oscillation in each chamber of the

Greenspan viscometer. However, in the thermal boundary layer in contact with the metal

walls of the chambers, the temperature oscillations decay exponentially to zero with the

characteristic length δ_t. The ratio of the energy dissipated in the thermal boundary layer

to the energy stored by creating a pressure difference between the chambers $\alpha_t \equiv 2\pi / Q_t$ is

the second most important contribution to reducing the Q of the Helmholtz oscillations.

The heat transported from the gas to the boundary of a chamber during half of an acoustic

cycle is approximately the product: (acoustic temperature change) × (heat

6

capacity/volume) × (volume of the thermal boundary layer of the chamber). These terms are approximated by $(\gamma-1)p_a k_s/\beta$, ρC_p, and $\delta_t A_{ch}$, respectively. Here, $\gamma \equiv C_p/C_v$ is the heat capacity ratio; p_a is the amplitude of the acoustic pressure, A_{ch} is the surface area of a chamber, and $\beta \equiv (\partial V/\partial P)_p/V$ is the volume expansivity, respectively. Of this heat transported, a fraction on the order of (acoustic temperature change)/(temperature) is dissipated in the boundary layer. The potential energy stored is $\frac{1}{2}p_a^2 V_{ch} k_s$ where V_{ch} is the volume of one chamber. These estimates are combined to obtain:

$$\frac{\text{thermal dissipation}}{\text{potential energy}} = \frac{[(\gamma-1)k_s p_a/\beta]\cdot\rho C_p\cdot\delta_t A_{ch}}{\frac{1}{2}p_a^2 V_{ch} k_s}\cdot\frac{(\gamma-1)\,k_s p_a/\beta}{T} \tag{7}$$

and finally

$$\alpha_t = 2\frac{(\gamma-1)\,\delta_t A_{ch}}{V_{ch}} \tag{8}$$

In arriving at Eq. (8), we have used the thermodymamic relation $\rho C_p = T\beta^2/[k_s(\gamma-1)]$.

The viscous and thermal losses may be combined to estimate the Q of the Helmholtz resonance. The chambers of all of the viscometers were cylinders with lengths not very different from their diameters; thus, we estimate $A_{ch}/V_{ch} = 3/r_{ch}$, where r_{ch} is the radius of the chamber. We obtain the simple result:

$$\frac{2g}{f_0} = \frac{1}{Q} = \frac{\alpha_v}{2\pi} + \frac{\alpha_t}{2\pi} = \frac{\delta_v}{r_d} + (\gamma-1)\frac{3\delta_t}{\pi r_{ch}} \tag{9}$$

Eq. (9) implies that the Greenspan viscometer is indeed a viscometer because the viscous contribution to the losses is much greater than the thermal contribution to the losses. For dilute gases, δ_v and δ_t have similar magnitudes and $(\gamma-1)$ is at most 2/3, its value for dilute monatomic gases. (Near the critical point, γ becomes very large.) Under the conditions of the present measurements with propane, $(\gamma-1) \approx 0.1$ and $r_d/r_{ch} \approx 0.05$. Thus, the ratio of the thermal term in Eq. (9) to the viscous term in Eq. (9) is approximately 0.005.

A useful design equation is obtained by combining Eq. (2) for δ_v and the viscous term in Eq. (9):

$$D_v = \eta/\rho = \pi f_0(r_d/Q_v)^2 \tag{10}$$

7

Eq. (10) shows that D_v may be determined by combining a measurement of r_d with frequency-response data from which $f_0(1/Q)^2$ is obtained.

Even in the limit $\delta_v \ll r_d$, additions to the heuristic argument are required for accurate work. The viscous and thermal losses shift the resonance frequency from the result in Eq. (5); however, Eq. (9) is still correct to first order in δ_v/r_d and δ_t/r_{ch}. The converging and diverging flow in the transition regions where the duct joins the cavities increases the mass of the oscillating gas by a factor of approximately $(1 + 1.598\ r_d/L_d)$. (In this work, $0.02 \leq r_d/L_d \leq 0.04$.) The coefficient 1.598 was determined through numerical calculations[5] It depends weakly on the dimensions of the cavity and the duct, effects that were treated correctly in the analysis but neglected in the present discussion. Furthermore, there is excess viscous dissipation in the transition region both inside the duct orifice and in the chamber near the orifice. The excess dissipation increases α_v a factor of approximately $(1 + 1.6\ r_d/L_d)$. Finally, one must also account for the duct that is used to admit gas to the viscometer.

III. OUTLINE OF DETAILED MODEL.

In a more detailed calculation to be presented elsewhere[6] we assumed that the acoustic source strength q_s generated by the transducer in chamber V_1 is proportional to the voltage driving the source transducer. We also assumed that the complex voltage generated by the detector transducer is proportional to the pressure p_2 at the detector located in chamber V_2. A calculation showed that the pressure at the inlet of the duct is very well approximated by the average pressure in V_1 and that the pressure at the detector is similarly well approximated by the pressure at the outlet of the duct.

Our model of the Greenspan viscometer is the network of acoustic impedances shown schematically in Fig. 4. The ratio p_2/q_s is computed from this model. Here, we identify the elements in the network and the functional forms of their impedances.

The input impedance of each chamber Z_v is

$$Z_v = \rho c^2 / i\omega V \tag{11}$$

with

$$V = V_{ch} + (1 - i)(\gamma - 1)A_{ch}\delta_t/2 \quad . \tag{12}$$

The complex volume V differs from the geometrical volume by a term that accounts for the admittance of the thermal boundary layer on the surfaces of the chamber.

The impedances of ducts are modeled as transmission lines with a characteristic impedance Z_0 and a complex propagation parameter Γ for acoustic flow in the duct given by:

$$
\begin{aligned}
Z_0 &= (\rho c / A_d) / \sqrt{(1 - F_v) \cdot [1 + (\gamma - 1)F_t]} \\
\Gamma &= \frac{i\omega}{c} \sqrt{\frac{1 + (\gamma - 1)F_t}{1 - F_v}} \\
F &= \frac{2J_1(\zeta)}{\zeta J_0(\zeta)} .
\end{aligned}
\tag{13}
$$

where J_0 and J_1 are Bessel functions and $\zeta \equiv (1 - i)\delta_v/r_d$ for F_v and $\zeta \equiv (1 - i)\delta_t/r_d$ for F_t. The approximations

$$F_v \approx (1 - i)\delta_v/r_d, \qquad\qquad F_t \approx (1 - i)\delta_t/r_d \tag{14}$$

are useful for the comparatively small values of δ_v/r_d and δ_t/r_d encountered in this work.

The T–parameters (Fig. 4) for the duct are given by:

$$Z_1 = Z_0 \tanh(\Gamma L_d/2), \qquad\qquad Z_2 = Z_0 / \sinh(\Gamma L_d) \tag{15}$$

The inertial and dissipative end effects are described by

$$Z_{end} = (\rho\omega/A_d)(i\delta_i + 0.81\delta_v) \tag{16}$$

where δ_i is defined by Eq. (17) below and, in this work, $\delta_i \approx 0.8 r_d$.

The dissipative part of Z_{end} was computed from numerical solutions of the Helmholtz equation with Neumann boundary conditions and the geometry of the viscometers. The solutions provided a dissipation-free model for the acoustic pressure. The losses were determined by integrating the square of the tangential acoustic velocity. The coefficient 0.81 of δ_v in Eq. (16) is the sum of two terms: the first, 0.45, is the contribution of the

9

tangential flow on the chamber wall ("baffle"); the second, 0.36, is the contribution from the evanescent waves just inside the orifice.

There is an integrable singularity in the velocity at the sharp corner where the duct joins the chamber. If the corner is rounded with a radius equal to 0.1 r_d, the coefficient 0.81 in Eq. (16) is reduced to 0.74. This change is significant; it implies that chamfers often used in machine shop practice must be accounted for.

The reactive part of Z_{end} can be calculated from the numerical determinations of either the eigenvalue or the input impedance of the cavity. As noted above, the reactive term depends weakly on cavity dimensions. The results of the numerical calculations are accurately described by the function

$$\frac{\delta_i}{r_d} = 0.8215 - 1.107\frac{r_d}{r_{ch}} + \frac{L_{ch}r_d}{3r_{ch}^2} \tag{17}$$

The constant term in this expression agrees with the literature value obtained through solutions of the Laplace equation for a duct coupled to an infinite baffle.[7] The second term shows the effect of a chamber radius, in good agreement with the calculation of Ingard.[8] The third term comes from a correction to the chamber's input-impedance due to the finite length of the chamber. The sum of the three terms varies between 0.782 and 0.799 for the four viscometers used in the current work.

As shown in Fig. 4, the fill duct can be represented by an impedance Z_f in parallel with Z_v. To do this, the fill duct can be replaced with a second T-equivalent network with propagation parameters appropriate for its very small radius. In this case, the exact functional forms for F_t and F_v must be used. The complicated expression that results will not be reproduced here. The expression was included in the "working equation" used to analyze our data; however, the present results are not sensitive to the effects of our very long, thin fill duct.

A "working equation" was constructed that expresses the measured frequency-

dependent voltage ratio, $V_{detector}/V_{source}$, as the product:

$$\frac{V_{detector}}{V_{source}} = \frac{V_{detector}}{p_2} \times \frac{p_2}{p_2'} \times \frac{p_2'}{p_1'} \times \frac{p_1'}{p_1} \times \frac{p_1}{V_{source}}. \tag{18}$$

The acoustic pressure ratios in Eq. (18) were expressed as functions of the impedances defined above for the network in Fig. 4. The two ratios, $V_{detector}/p_2$ and p_1/V_{source}, that characterize the transducers were shown to be independent of frequency by auxiliary measurements using an acoustic coupler.

IV. APPARATUS AND MEASUREMENTS.

A. Construction of Viscometers

Fig. 1 shows a cross-section of viscometer 1. The body of the viscometer was turned on a lathe from a single piece of aluminum. The duct was drilled undersized and then reamed to its final size. The interior surfaces of the viscometer were not polished.

The dimensions of the viscometers' bodies were measured with a coordinate measuring machine. The machine logged the coordinates of surfaces that were contacted by a 1.4 mm diameter ruby ball. The internal diameters of the ducts were measured at 1 mm intervals along the axes of the ducts.

Table I summarizes the key dimensions of the viscometers. Except for their dimensions, all four viscometers were essentially identical.

Table I. Dimensions of the viscometer in mm.

Viscometer	L_d	r_d	L_{ch}	r_{ch}
0	38.092	0.7998	31.565	15.873
1	19.109	0.7976	15.749	15.875
2	28.586	0.7985	15.769	15.876
5	28.531	0.8267	31.582	15.876

11

B. Transducers

Two brass flanges containing transducers were used as interchangeable ends of all of the viscometers. These flanges were bolted to the body of the viscometer using blind tapped holes that are not shown in Fig. 1. The joints between the flanges and the body were sealed with a thin layer of organic grease. Efforts were made to avoid scratches and crevices that might attenuate the acoustic oscillations. (Scratches, pits, *etc.* with at least one dimension much smaller than δ_v are probably not important to the operation of Greenspan viscometers.)

Both transducers were installed in ports machined out of each flange. The acoustic source was a "stack" of coin–shaped piezoelectric transducers (PZT) connected mechanically in series and electrically in parallel. The length of the stack changed in response to the applied voltage. The stack was separated from the test gas in chamber V_1 by a 0.1 mm (0.004 in.) thick × 15 mm diameter stainless–steel foil that had been soldered into a slight recess in the interior face of the flange. The acoustic detector was a thin cylindrical bimorph PZT that had been removed from a commercial buzzer. The detector was sealed behind a foil that faced the inside surface of V_2. Thus, the test gas within the viscometers was in contact with robust metal parts only: the viscometer body, the flanges, and the foils.

Under typical operating conditions (viscometer 1, argon, 100 kPa), the source was driven at 46 V (rms), and it generated an acoustic pressure on the order of 0.4 Pa (rms). Allowing for the Q of the double Helmholtz resonator and the volume of chamber V_1, we estimated that the volume displaced by the source transducer was 0.014 mm³.

Under a variety of conditions, we reduced the drive voltage by a factor of 10 and repeated the measurements of the frequency response. No changes were detected confirming that during normal operation, the Greenspan viscometer can be described by linear acoustics despite the presence of fairly sharp corners at the ends of the duct.

In common with other studies of acoustic resonators[9] the signal-to-noise ratio varied

12

as $P^{3/2}$. To understand this, we note that, to a good approximation, the displacement produced by the source transducer was independent of P. Thus, well below f_0, the acoustic pressure p_a in chamber V_1 was proportional to P. Near resonance where the viscometer was used, p_a was amplified by a factor of Q which itself was proportional to $P^{1/2}$. Even at the lowest pressures studied, the signal-to-noise ratio was not a factor limiting the accuracy of the determination of the viscosity.

C. Test Conditions

To test several viscometers with several gases, we constructed a pressure vessel with an interior volume of approximately 1800 cm^3. The viscometer under test was suspended inside the pressure vessel. This isolated the viscometer from ambient acoustic noise and relieved us of the necessity of making every viscometer pressure-tight.

The temperature of the viscometer under test was determined by a calibrated thermistor that had been inserted into a blind hole drilled into the viscometer's body. When the viscometer was suspended in the pressure vessel the thermal relaxation time between the viscometer and the ambient air was 5 hours. In effect, the viscometer was thermally isolated from the room on the time scale of the viscosity measurements.

For a typical test run, the pressure vessel was filled with the test gas at the highest pressure to be studied (1 MPa for helium and argon; 600 kPa for propane), 15 minutes were allowed to elapse for thermal equilibration, and then the frequency response, temperature, and pressure were measured. Then some of the test gas in the pressure vessel was removed and the operations were repeated. As the measurements progressed, the temperature of the viscometer decreased several tenths of a degree because of the adiabatic cooling of the test gas as the pressure was reduced. The thermometer in the body of the viscometer enabled us to measure this effect.

D. Fill Capillary

A fill capillary led from chamber V_1 to the interior of the pressure vessel. If the flow impedance of the capillary had not been sufficiently great near the Helmholtz resonance frequency, the capillary would have functioned as a second duct in parallel with the duct between the two chambers. The second duct would have greatly altered the frequency response of the viscometer and a second Helmholtz resonance might have appeared. To achieve a high impedance, we used a stainless-steel capillary with an O.D. of 0.029" (0.74 mm), an I.D. of 0.016" (0.41 mm), and a length of 10 cm. The capillary was sealed into a hole that had been drilled through the body of the viscometer.

E. Frequency Response Measurements.

For each viscometer, gas, and thermodynamic state, the complex frequency response of the viscometer was measured at 21 equally spaced frequencies that spanned the range $f_m \pm 2g$, where f_m was the frequency at which the detected signal attained its maximum amplitude. These measurements were made with a computer-controlled frequency synthesizer, lock-in amplifier, and digital voltmeter, using techniques that we have described elsewhere[10] Because the step-up transformer connected between the frequency synthesizer and the source transducer did not have a flat frequency response at low frequencies, one change was required. The detector output voltage was divided by the voltage measured at the source transducer at each frequency.

The real and imaginary parts of the measured frequency response, such as that displayed in Fig. 3, were simultaneously fit by Eq. (18) with the addition of a complex background term which was either a constant or a linear function of frequency. (A constant background term was adequate for all the data except the helium data taken with viscometer 0.) Thus, either 6 or 8 parameters were fitted to the data. Two parameters characterize the frequency and width of the Helmholtz resonance; two comprise a complex amplitude that accounts for the gain of the electronics and transducers; and the two or four

14

background parameters account for electrical and mechanical crosstalk between the transducers.

Fig. 3 displays a typical example of the measured frequency response of viscometer 1 together with the deviations of the data from our model. The model represents the data with very small systematic fractional deviations on the order of ± 0.0005. The fit defines values of g and f_m with fractional imprecisions of 0.0005 and $0.0005 \times g/f_m \approx 3.5 \times 10^{-5}$, respectively. The resonance frequency is mainly sensitive to the viscometer's dimensions and the speed of sound c_0; the half-width is mainly sensitive to D_v. If the model for the viscometer were perfect, the corresponding fractional uncertainties in D_v and c_0 would be 0.001 and 3.5×10^{-5}, respectively.

V. RESULTS.

Fig. 5 displays the results for D_v obtained with viscometer 1, the "best" viscometer. In each case, the plot shows the fractional deviations of the measured values of D_v from values taken from the literature. Nearly all the results for helium, argon, and propane fall within a band ± 0.005 wide centered 0.010 above the data from the literature. The ordinate for Fig. 5 is $\delta_v/r_d \approx 1/Q$, which is the most important parameter that determines the frequency response function. Remarkably, for the smallest values of δ_v/r_d that occur at the highest pressures, the data for argon and the data for propane track within 0.3%. At the larger values of δ_v/r_d the data for the different gases diverge. The larger values of δ_v/r_d occur at low pressures where the viscous boundary layer fills the duct nearly completely. Under these conditions, the Qs of the resonances are low and the requirement of properly accounting for the frequency responses of the transducers becomes severe. Thus, we do not recommend using Greenspan viscometers at larger values of δ_v/r_d.

Fig. 6 displays the results for D_v obtained with viscometer 0, the "worst" viscometer. Again, nearly all the results for helium, argon, and propane fall within a band ± 0.005 wide; however, for this viscometer the data are centered approximately 0.025 above the data

15

from the literature.

At present, we have no certain explanation for why the data from the viscometers differ from each other. The data for the other viscometers that we have studied fall between the data for viscometer 1 and viscometer 0. In the future, we shall report the results of systematic investigations of the effects of surface finish and of the "end corrections" for the converging/diverging flow fields near the ends of the duct. The ducts of all of our viscometers had crude chamfers at their ends that were not considered when analyzing the data.

In order to construct Figs. 5 and 6, we used information from the literature for D_v. For argon, the zero-density viscosity was calculated for the HFD–B3 potential of Aziz and Slaman,[11] and the density dependence was taken from Maitland et al.[2] For helium, the zero-density viscosity was calculated from the potential of Ref. 2 and the density dependence was taken from Ref. 12. For propane, the correlation by Vogel[13] was used. Because Vogel calibrated his viscometer with the data of Kestin et al., his correlation (at low pressures) agrees within ±0.1 % with the data of Kestin et al.[14] Thus, the literature values of the viscosity for the three different gases are ultimately traceable to the same laboratory and their mutual consistency is likely to be greater than their absolute accuracy. As mentioned above and in Ref. 2, the viscosity data for helium near ambient temperature appear to have a systematic error of only 0.3%.

If each viscometer had been calibrated with a single gas at a single temperature and at a pressure with a comparatively small value of δ_v/r_d, then nearly all the results for D_v from that viscometer for all three gases would have been within ±0.5 % of the data from the literature.

Fig. 7 shows the deviations of the fitting parameter f_0 for the frequency response data from viscometers 0 and 1 from the values predicted from the measured dimensions of the viscometers, the speed of sound in the test gases, and the model given by Eq. 18. The fractional deviations of f_0 from their expected values and the small inconsistencies of the

16

results among the three gases are very approximately the same size as the deviations of the values of D_v; the deviations may have the same, presently unknown, cause.

VI. PROSPECTS FOR A PRIMARY STANDARD GREENSPAN VISCOMETER.

As just mentioned, the results from the "best" viscometer contain several puzzles that we hope will be resolved by further research. If they are, the performance of the Greenspan viscometer will approach those of other standard viscometers. In this spirit we contrast the Greenspan viscometer with current standards and consider directions for further development.

The presently accepted instrument for making absolute measurements of the viscosity of gases is based upon a disk that oscillates between fixed plates while suspended from a delicate quartz fiber.[15] This instrument has a thoroughly developed theory that accounts for the "edge corrections" resulting from the finite dimensions of the disk. The geometry of the oscillating-disk viscometer is designed to inhibit secondary flow resulting from either the very low frequency ($\sim$ 0.1 Hz) oscillations or from temperature gradients. However, oscillating-disk viscometers are difficult to maintain. To the authors' knowledge, there is no longer a primary standard oscillating disk viscometer in operation. The oscillating disk viscometers are ordinarily excited with an impulse and the subsequent free decay of the oscillations is observed. In contrast with the present study of the Greenspan viscometer, we are not aware of studies of the frequency response of the oscillating disk viscometer directed towards testing the theory of its operation.

As indicated above, the Greenspan viscometer is rugged and prototypes are easily constructed. The theory for the Greenspan viscometer contains corrections for the acoustic flows near the ends of the ducts that are comparable in magnitude to the edge corrections need for the oscillating-disk viscometer. A comparatively simple modification of the present Greenspan viscometer will facilitate systematic studies of the effects of the flows at the ends of the duct. Such a modification is shown in Fig. 8, top.

17

Fig. 8, top shows a schematic drawing of a Greenspan viscometer with a removable duct. We are constructing such an instrument as a convenient platform for systematically testing the theory of "end" corrections that scale with r_d/L_d. Furthermore, the approach shown in Fig. 8 (top) is suitable for using very sophisticated cylinders as ducts. For example, precision cylinders manufactured for use in dead-weight pressure gages are lapped until their surfaces have scratches that are 50 nm or even finer. The deviations from roundness and internal diameters of such high-quality cylinders can be determined to several parts in 10^5. Such a cylinder could be used as the duct of a Greenspan viscometer. (The duct of an acoustic viscometer may have a diameter that is much larger than that of the capillary tube used in unidirectional flow viscometers. This design flexibility exists because the viscous dissipation in the acoustic viscometer occurs within a thin boundary layer of thickness δ_t surrounding the perimeter of the duct. In contrast, the dissipation in a unidirectional flow viscometer occurs throughout the capillary.)

Finally, we mention three ways in which the concepts of differential metrology can be applied to the Greenspan viscometer.

First, one can construct a Greenspan viscometer in which a solid rod, *i.e.* a piston, partially fills a duct. Fig. 8, bottom shows the design of such a viscometer. In this design, the gap between the rod and the duct is significantly larger than δ_v everywhere, and the rod can be supported in two or more configurations such that one end is within the duct and the other end is within one of the chambers. One would measure the frequency response of such a Greenspan viscometer when the rod occupies several different known positions along the axis of the cylinder. The converging/diverging flow fields near the ends of the duct and near the ends of the rod are unchanged upon displacing the rod axially; thus, the effects of these difficult-to-model portions of the flow field will cancel out of the difference measurements to a high degree. The differences could be more accurately related to the viscosity than any single measurement.

Second, one may use two acoustic detectors, one in V_1 and one in V_2. (See Fig. 8, bottom.) If the two detectors are sufficiently well-matched, neither one has to be calibrated, and the results of the measurements are not subject to errors resulting from imperfect modeling of the fill duct. One then measures a pressure ratio

$$(p_1 - p_2)/\, p_2 \;=\; Z_0 \,\Gamma\, L_d \,/(Z_v + Z_{end}) \qquad . \qquad\qquad (19)$$

that still involves "end" corrections but otherwise is related simply to the viscosity.

Third, if there is a second source transducer located in V_2 the roles of the two detectors may be interchanged without moving either one. Thus, the degree to which they are similar can be evaluated *in situ* and appropriate corrections can be made for their differences.

ACKNOWLEDGMENTS

REFERENCES

1 Martin Greenspan and Francis N. Wimenitz, "An Acoustic Viscometer for Gases — I," NBS Report 2658 (1953).

2 R.A. Aziz, A.R. Janzen, and M.R. Moldover, "*Ab Initio* Calculations for Helium: a Standard for Transport Property Measurements," Phys. Rev. Lett. **74**, 1586 (1995).

3 W.A. Wakeham, A. Nagashima, and J.V. Sengers, *Measurements of the Transport Properties of Fluids*, (Blackwell Scientific Publications, Oxford, 1991), Chapter 3.

4 K.A. Gillis, M.R. Moldover, and A.R.H. Goodwin, Rev. Sci. Instrum. **62**, 2213 (1991).

5 J.B. Mehl, J. Acoust. Soc. Am. **97**, 3327 (1995) and unpublished calculations.

6 J.B. Mehl, K.A. Gillis, and M.R. Moldover, to be published.

7 L.V. King, Phil. Mag. Series 7, **21**, 128 (1936).

8 U. Ingard, J. Acoust. Soc. Am. **25**, 1037 (1953).

9 M.R. Moldover, J.P.M. Trusler, T.J. Edwards, J.B. Mehl, and R.S. Davis, J. Research of NBS, **93**, 85 (1988).

10 M.R. Moldover, J.B. Mehl, and M. Greenspan, J. Acoust. Soc. Am. **79**, 253 (1986).

11 R.A. Aziz and M.J. Slaman, J. Chem. Phys. **92**, 1030 (1990).

12 G.C. Maitland, R. Rigby, E.B. Smith, and W.A. Wakeham, *Intermolecular Forces: Their Origin and Determination*, Appendix 4, Table A4.3 (Clarendon Press, Oxford, 1981).

13 E. Vogel, "The Viscosity of Gaseous Propane and its Initial Density Dependence," Proceedings of the 12th Symposium on Thermophysical Properties, Boulder, Colorado, June 19-24, 1994.

14 J. Kestin, S.T. Ro, and W.A. Wakeham, Trans. Faraday Soc. **67**, 2308 (1971).

15 Ref. 3, pp. 25 - 31.

CAPTIONS FOR FIGURES

FIG. 1.   Cross-section of Greenspan viscometer 1.

FIG. 2.   The viscous diffusivity $D_v \equiv \eta/\rho$ as a function of pressure for the gases studied. In some cases, data from several viscometers are superimposed.

FIG. 3.   Top: The real (u) and imaginary (v) components of $V_{detector}/V_{source}$ as a function of the excitation frequency. These representative data were taken with argon in viscometer 1 at 295.9 K and 300.3 kPa. Bottom: Deviations of u and v from a fit of Eq. 18 to the data shown above. The fractional deviations from the fit are all less than 0.0005.

FIG. 4.   Equivalent circuit of the Greenspan viscometer. The duct is represented by the "T" equivalent circuit for a transmission line shown within the dashed box. The T-parameters Z_1 and Z_2 are defined in the text. The source q_s drives the three parallel impedances: (1) the cavity impedance Z_v, (2) the duct represented as an end impedance Z_{end} in series with the T-equivalent circuit, and (3) a parallel duct Z_f representing the fill capillary.

FIG. 5.   Values of $D_v \equiv \eta/\rho$ measured with viscometer 1 minus the values from the literature for three gases as a function of δ_v/r_d, the ratio (viscous penetration length)/(radius of duct). The data for the three gases cluster about $\Delta D_v/D_v = 0.01$, except for the data at the lowest pressures ($\delta_v/r_d > 0.22$) where the Qs of the resonances are smallest.

FIG. 6.   Values of $D_v \equiv \eta/\rho$ measured with viscometer 0 minus the values from the literature for three gases as a function of δ_v/r_d, the ratio (viscous penetration length)/(radius of duct). The data for the three gases cluster about $\Delta D_v/D_v = 0.025$.

FIG. 7.   Deviations of the fitted resonance frequencies f_0 from those calculated from Eq. (18). Top: Results from viscometer 0; bottom: results from viscometer 1.

FIG. 8.   Top: Cross-section of Greenspan viscometer with removable duct. An accurately characterized cylinder such as those used in dead-weight pressure gages could be used as the duct. Bottom: Cross-section of Greenspan viscometer with a movable rod partially inserted into the duct and with matched sources and detectors.
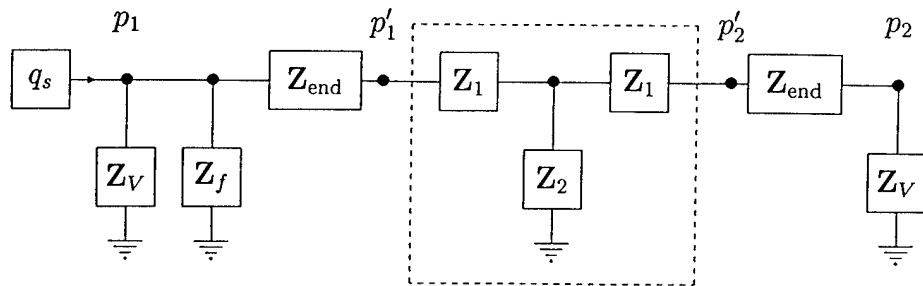
Fill Capillary

Duct

Source

Detector

V_1

V_2

51 mm
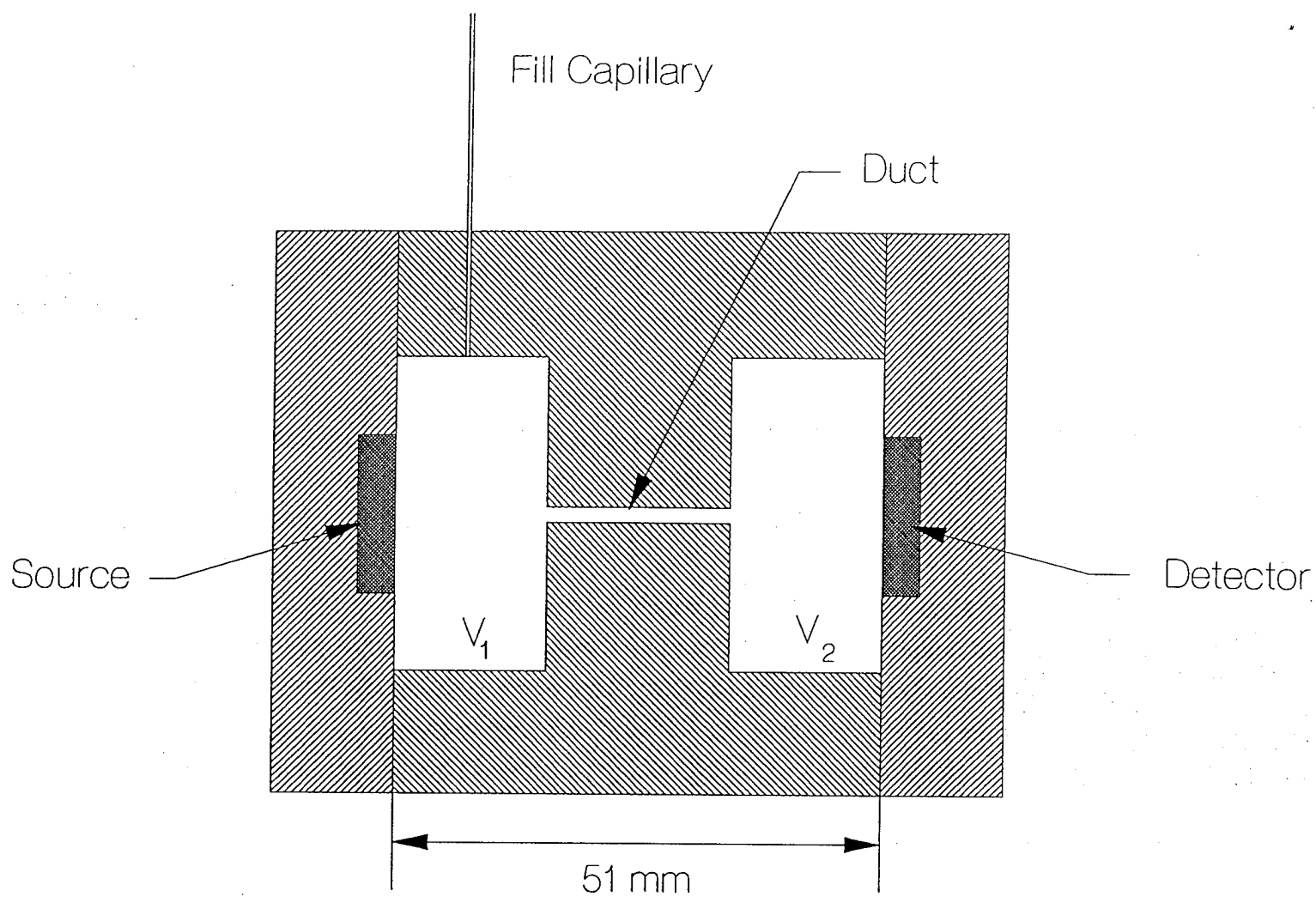
Fig 1

Fig 1
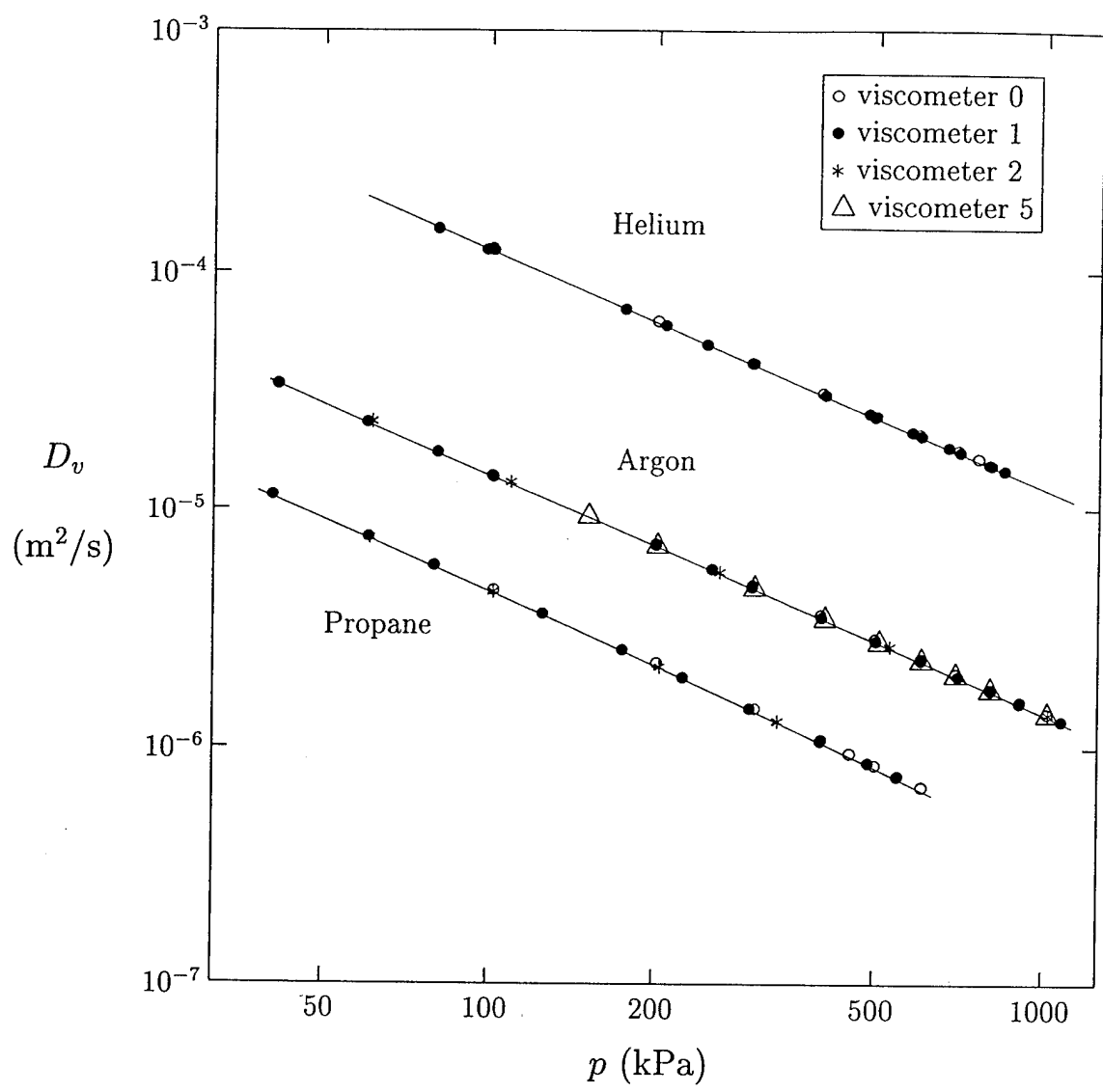
Fig. 2
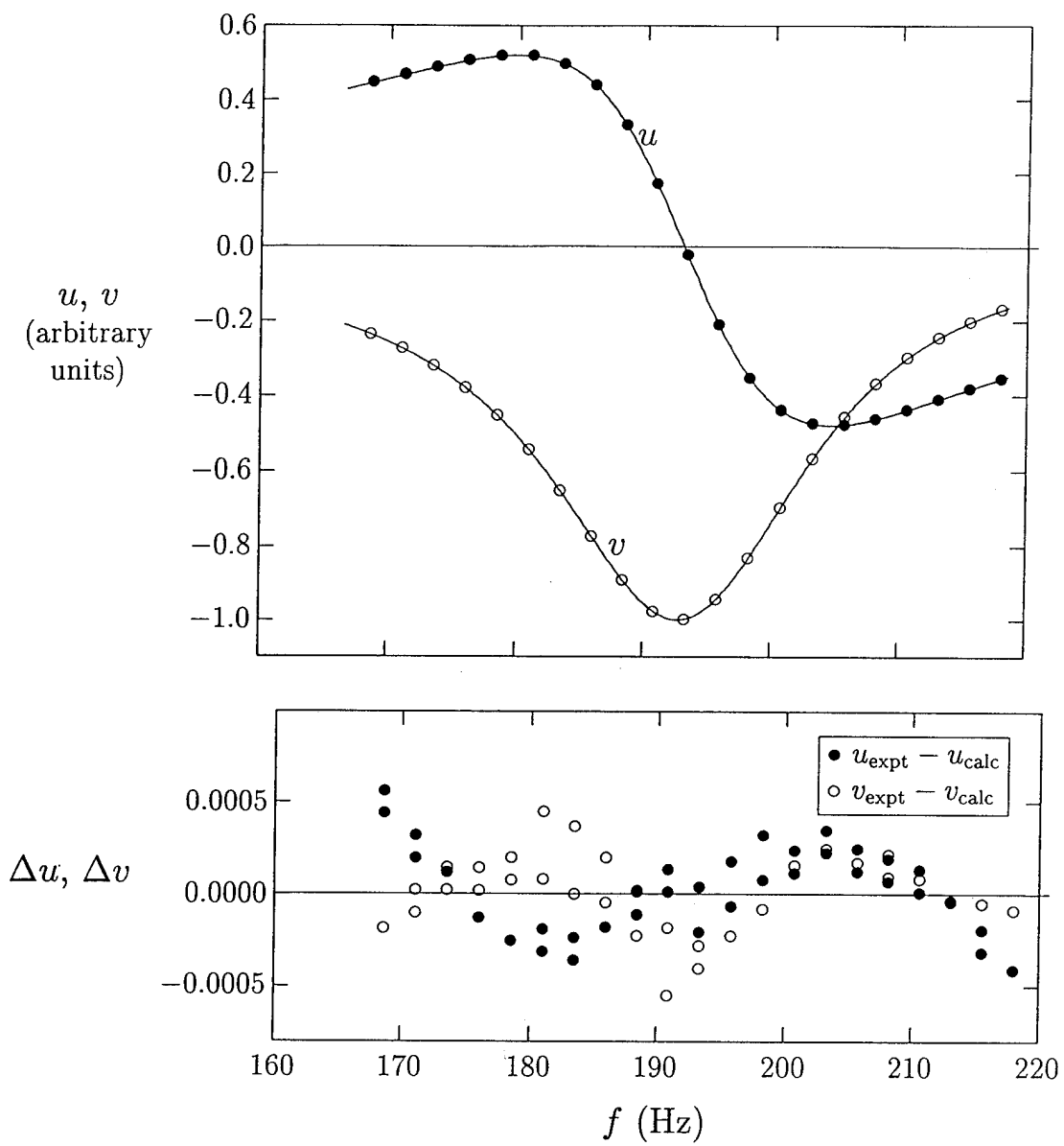
Fig 3

Fig 4

Fig 5

Fig 6

Fig 7

Fill Capillary

Duct

Source

Detector

V_1

V_2

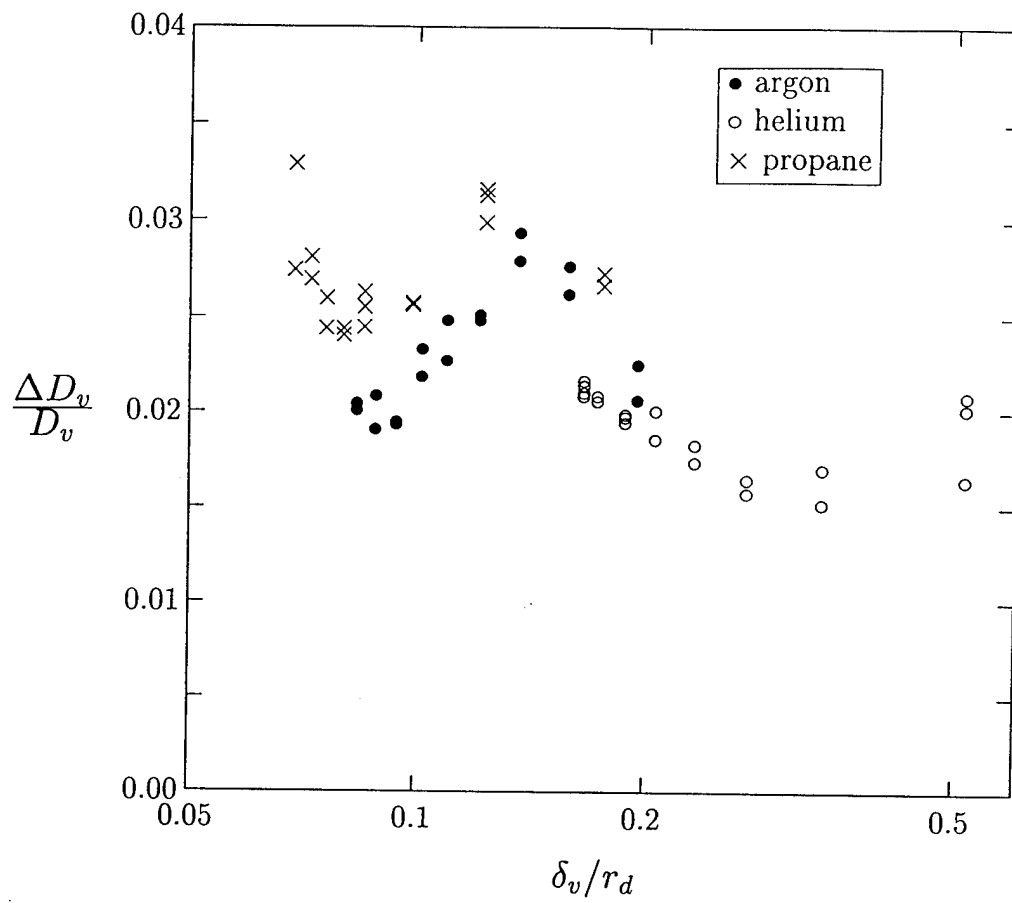Fill Capillary

Duct

"Piston"

Source
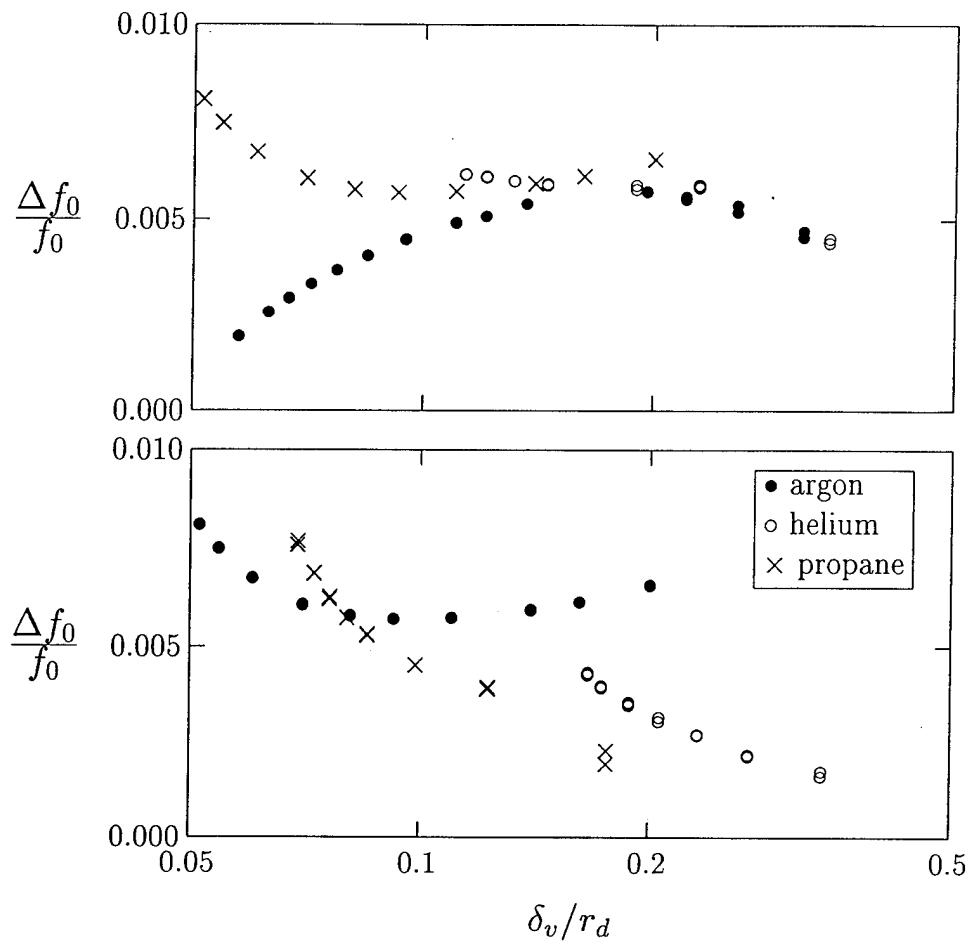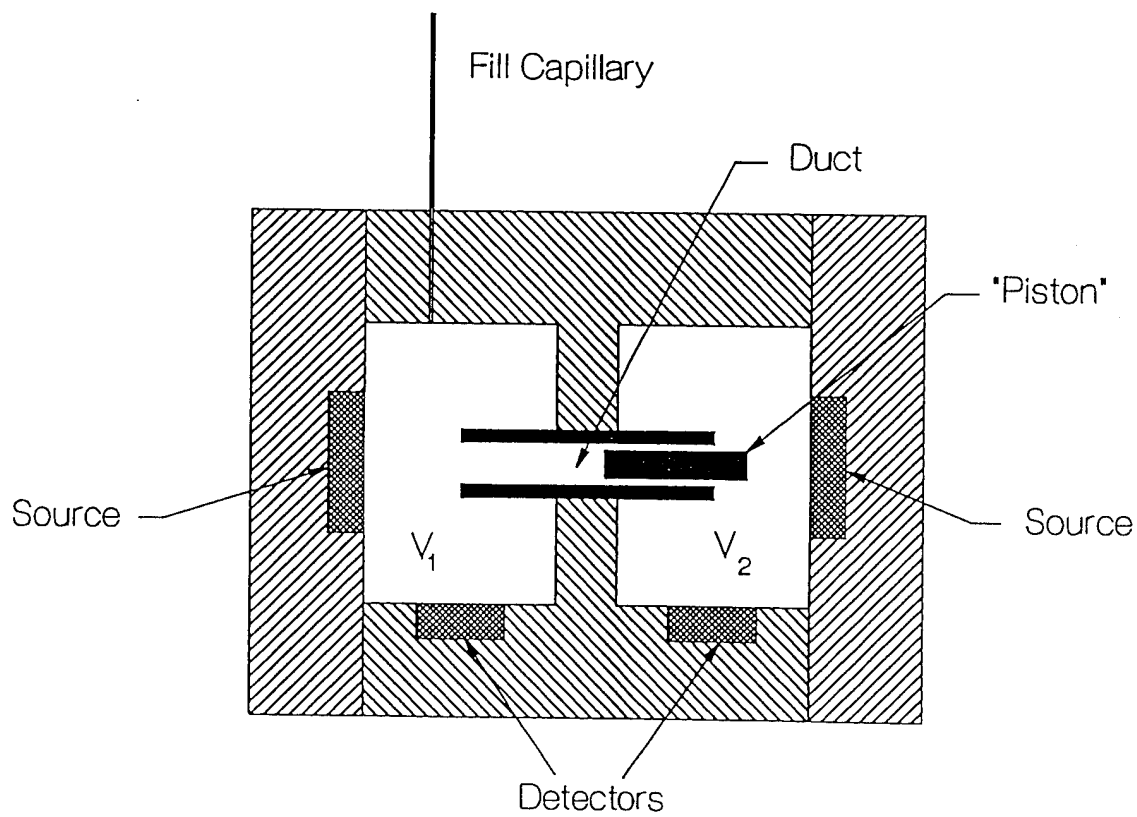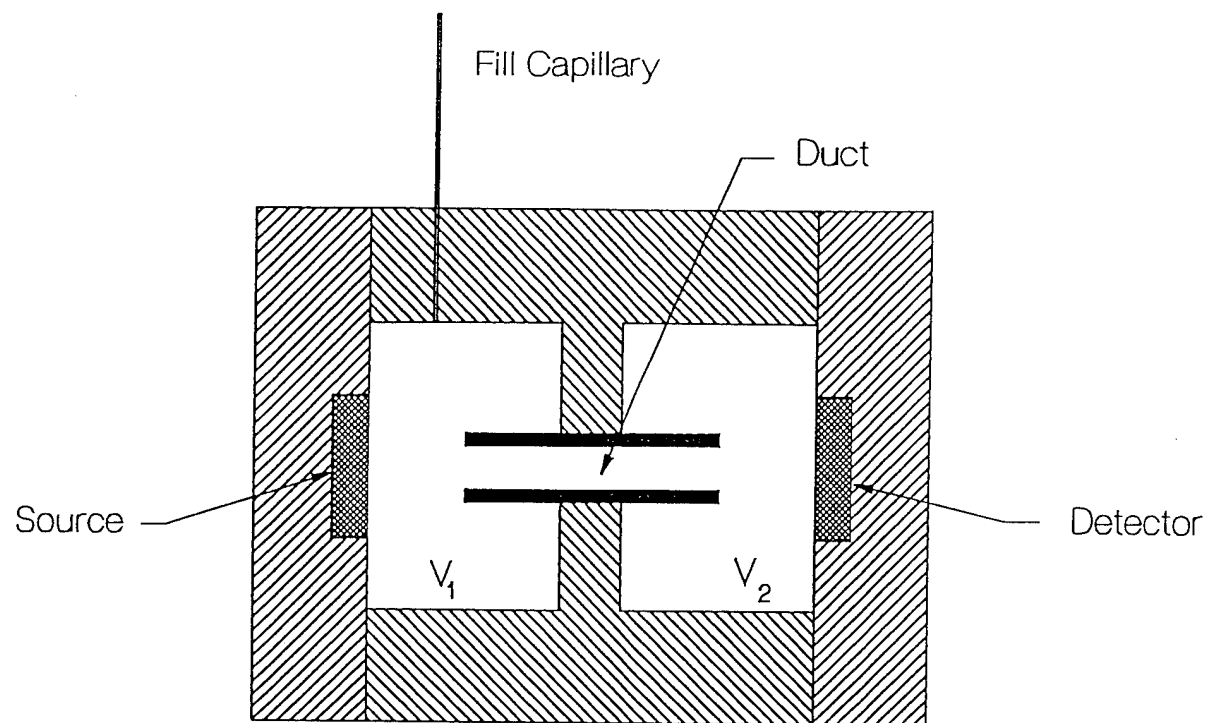
Source

V_1

V_2

Detectors
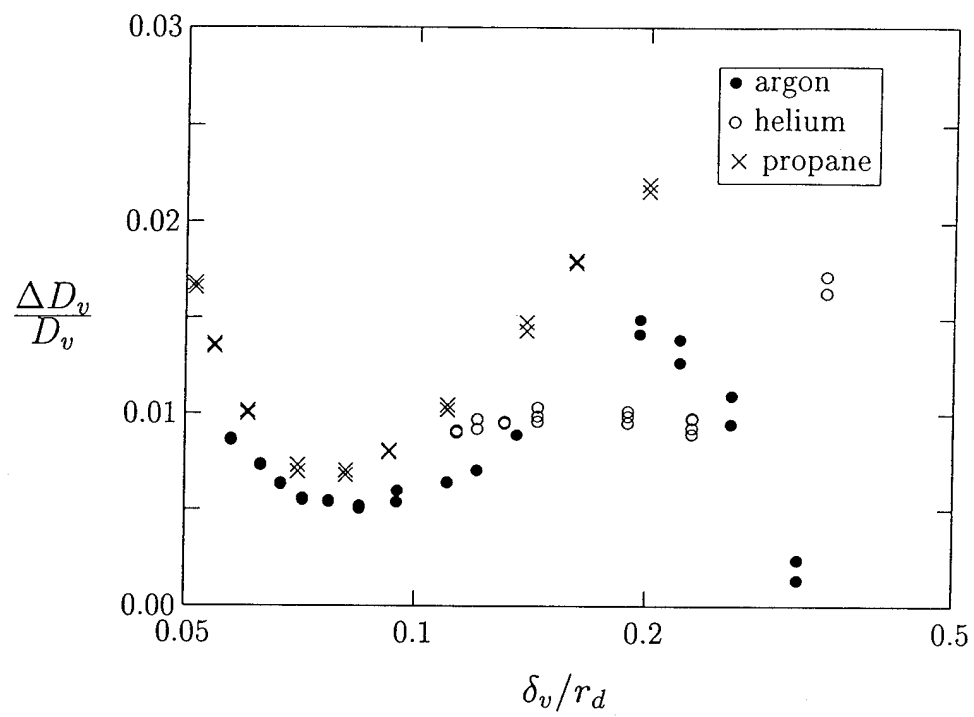
Fig 8

Design of acoustic devices for the accurate and precise measurement of transport properties of pure and mixed gases
Part I
Greenspan Viscometer:
Numerical Calculations

Report to
National Institute of Standards and Technology
Reference # 43NANB410297

by

James B. Mehl
1014 Baylor Drive
Nottingham Green
Newark, DE 19711-3130

28 September 1994
(Corrected printing of 23 March 1995)

1

Abstract

This report summarizes numerical calculations of the pressure and velocity fields in a Greenspan viscometer, *i.e.* a double-Helmholtz cavity resonator. The computational technique is the boundary integral-equation (BIE) method in which the eigenvalue problem is expressed as a surface integral equation. For axisymmetric cavities the integral equation becomes one-dimensional and high-accuracy calculations can be carried out at moderate cost. The geometries explored consist of a cylindrical duct coupled to coaxial cylindrical cavities at the ends. The pressure and velocity fields and the eigenvalues were calculated for several configurations. The major results are (1) calculation of the ratio of losses on the baffle surrounding the duct orifice to losses in the duct, (2) validation of theories of the mass end correction for the duct, and (3) studies of the effect of duct-orifice edge rounding on the velocity fields near the orifice.

Contents

ω	$2\pi\times$ frequency
ρ	density of the gas
c	speed of sound in the gas
k	ω/c
r_d	duct radius
$A = \pi r_d^2$	cross-sectional area of duct
L_d	duct length
$V = \pi r_c^2 L_c$	cavity volume (one cavity)
L_c	cavity length
r_c	cavity radius

Table 1: Notation

1 Introduction

An acoustic viscometer based on a double-Helmholtz resonator was described by Greenspan and Wimenitz in 1953.[1] The geometry is defined in Fig. 1.
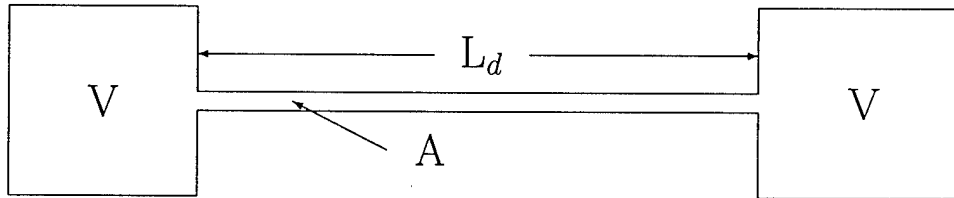
Figure 1: Schematic representation of a Greenspan viscometer.

This report summarizes numerical calculations of the pressure and velocity fields in a Greenspan viscometer for the non-dissipative case. (Dissipative effects are treated in Part II of this report.)

A theoretical model of the resonator for the non-dissipative case is useful for defining terms and establishing the magnitudes of quantities. This model

---

[1]Martin Greenspan and Francis N. Wimenitz, *An Acoustic Viscometer for Gases – I*, NBS Report 2658 (1953).

is extended further in a later section dealing with the effective length of the duct. The duct has a series acoustic impedance equal to

$$\mathbf{Z}_d = i\omega\rho L_d/A. \tag{1}$$

Each cavity has an acoustic impedance (in the low-frequency limit)

$$\mathbf{Z}_V = \frac{\rho c^2}{i\omega V}. \tag{2}$$

The input impedance of a duct terminated by a cavity is given by

$$\frac{\mathbf{Z}_{\text{in,d}}}{\mathbf{Z}_0} = \frac{\mathbf{Z}_V/\mathbf{Z}_0 + i\tan kL_d}{1 + (\mathbf{Z}_V/\mathbf{Z}_0)i\tan kL_d}, \tag{3}$$

where $\mathbf{Z}_0 = \rho c/A$ is the characteristic impedance of the duct. The resonance condition for the duct terminated by cavities at each end is

$$\mathbf{Z}_V + \mathbf{Z}_{\text{in,d}} = 0. \tag{4}$$

This has a solution

$$k^2 = \frac{2A}{VL_d}\left[\frac{kL_d}{\tan kL_d} + \frac{AL_d}{2V}\right] \tag{5}$$

which approximately equals

$$k_0^2 = \frac{2A}{VL_d} \tag{6}$$

in the limit of small kL_d. Note that Eq. (5) has two small correction terms. The second is explicitly equal to the ratio of the duct volume to the total cavity volume. The other correction, from the ratio of the tangent to its argument, is approximately $(k_0 L_d)^2/3 = 2AL_d/3V$, hence of the same magnitude.

2   Numerical calculations

2.1   Boundary value problem

The acoustical modes of a rigid cavity are closely related to the solution of the Neumann boundary-value problem for the Helmholtz equation. For a

cavity C bound by a surface S the problem is defined by

$$
\begin{aligned}
(\nabla^2 + k^2)\Phi(\mathbf{r}) &= 0, \quad \mathbf{r} \in C \\
\mathbf{n} \cdot \nabla\Phi(\mathbf{r}) &= 0, \quad \mathbf{r} \in S,
\end{aligned}
\tag{7}
$$

where $\mathbf{n}$ is the outward normal at $\mathbf{r}$. An equivalent form of the same boundary-value problem is the integral equation

$$
\Phi(\mathbf{r}') \, \Omega(\mathbf{r}') = -\int \Phi(\mathbf{r}) \, \mathbf{n} \cdot \nabla G(\mathbf{r}', \mathbf{r}) \, dS,
\tag{8}
$$

where $\mathbf{r}$ and $\mathbf{r}'$ are both on S, and $\Omega(\mathbf{r}')$ is the solid angle subtended by S at $\mathbf{r}'$, and the fundamental solution, or Green's function, is

$$
G(\mathbf{r}', \mathbf{r}) = \frac{e^{ikR}}{R}, \quad R = |\mathbf{r} - \mathbf{r}'|.
\tag{9}
$$

The kernel of the integral equation (8) can be integrated over the azimuthal coordinate ϕ for axisymmetric cavities. For such geometries the resulting integral equation is one-dimensional. Solutions yield both the eigenvalue k and the eigenfunction Φ on the surface. Eigenfunctions can be calculated for $\mathbf{r}$ within the cavity using Green's formula and the surface values. However, such calculations have not been carried out in this work.

Let the shape of an axisymmetric cavity be defined by the parametric equations $r(t)$, $z(t)$ in cylindrical coordinates. The one-dimensional form of Eq. (8) is

$$
-\Omega(t')\Phi(t') = \int K(t', t)\Phi(t)h(t) \, dt,
\tag{10}
$$

where

$$
K(t', t) = rn_r \frac{\partial}{\partial r} G(r', z'; r, z) + rn_z \frac{\partial}{\partial z} G(r', z'; r, z).
\tag{11}
$$

2.2 Numerical approximation and solution

A summary of the numerical method is presented in this section. The objective is to present sufficient detail so as to provide a context for interpreting the numerical results. Details of the implementation will be published elsewhere.

The integral equation (10) can be approximated by the following procedure. Divide the arc into N intervals, where N is even. Let the jth interval correspond to $t_{j-1} \leq t < t_j$, for $j = 1, 2, \ldots, N$. The values of $\Phi(t')$ at the end points of the intervals then satisfy the exact equation

$$-\Omega_{i'}\Phi(t_{i'}) = \sum_{j=1}^{N/2} \int_{t_{2j-2}}^{t_{2j}} \Phi(t)K(t_i, t)h(t)\, dt \tag{12}$$

for $0 \leq i \leq N$.

It is convenient to let the parameter t vary from 0 to N, and to let the length of each interval $t_{i+1} - t_i$ equal unity, so that $t_i = i$. The integral in Eq. (12) must be handled carefully when the range of integration includes the logarithmic singularity at $t' = t$. Atkinson[2] suggested the method of product integration for weakly-singular kernels. For the interval $2j - 2 \leq t \leq 2j$ let the unknown eigenfunction be approximated by an interpolating polynomial

$$\begin{aligned}
\Phi(t) \approx\ &\tfrac{1}{2}(t - 2j + 1)(t - 2j)\Phi(2j - 2) \\
&- (t - 2j + 2)(t - 2j)\Phi(2j - 1) \\
&+ \tfrac{1}{2}(t - 2j + 2)(t - 2j + 1)\Phi(2j).
\end{aligned} \tag{13}$$

The singular integrals in Eq. (12) can then be approximated by

$$\begin{aligned}
&\int_{2j-2}^{2j} \Phi(t)K(t_i, t)h(t)\, dt \\
&\approx \tfrac{1}{2}\Phi(2j - 2) \int_{2j-2}^{2j} (t - 2j + 1)(t - 2j)K(t_i, t)h(t)\, dt \\
&\quad - \Phi(2j - 1) \int_{2j-2}^{2j} (t - 2j + 2)(t - 2j)K(t_i, t)h(t)\, dt \\
&\quad + \tfrac{1}{2}\Phi(2j) \int_{2j-2}^{2j} (t - 2j + 2)(t - 2j + 1)K(t_i, t)h(t)\, dt.
\end{aligned} \tag{14}$$

---

[2] K. E. Atkinson, *A Survey of Numerical Methods for the Solution of Fredholm Integral Equations of the second kind*, Society for Industrial and Applied Mathematics, Philadelphia, (1976) pp. 117–119.

With this approximation for the integrals Eq. (12) becomes a system of $N + 1$ linear equations in the $N + 1$ unknowns $\Phi(i) \equiv \Phi_i$. This system of equations can be written in the vector form

$$\widetilde{\mathbf{W}(k)}\widetilde{\Phi} = -\widetilde{\mathbf{\Omega}}\widetilde{\Phi}, \tag{15}$$

where $\widetilde{\Phi}$ is a vector with $N+1$ elements, $\widetilde{\mathbf{W}(k)}$ is a square matrix of dimension $N + 1$, and $\widetilde{\mathbf{\Omega}}$ is a diagonal matrix with the ii-element equal to the negative of the interior angle subtended by the surface at point i. The eigenvalues are determined by the condition that the determinant vanish:

$$|\widetilde{\mathbf{W}(k)} + \widetilde{\mathbf{\Omega}}| = 0. \tag{16}$$

The eigenvalues can be determined from the linear equations once the eigenvalues are known. Rather than simply using the solutions of the linear equations, refined estimates of the eigenfunctions were obtained by using the power-method.[3]

In summary, the numerical technique yields estimates of the eigenvalues k and associated eigenfunctions ϕ on the boundary. The eigenfunction representation corresponds to piece-wise quadratic approximations on a mesh of $N/2$ elements. On each element the eigenfunction has a quadratic representation defined by the center and end values. The eigenfunctions are continuous from one element to the next. The derivatives of the eigenfunction with respect to arc length are linear with the elements and in general discontinuous on the boundaries between elements.

2.3 Viscometer shapes and mesh configurations

Calculations were carried out for the five viscometer shape configurations shown in Fig. 2. A typical mesh configuration is defined in Fig. fig:viscometer1. Because of the symmetry it is sufficient to define the mesh for a quarter of the cross-section of the viscometer.

Most calculations were carried out with the following mesh assignments:

---

[3]See, *e.g.* Germund Dahlquist and Åke Björk, *Numerical Methods,* (Prentice-Hall, Englewood Cliffs, N.J., 1974), Section 5.8.1.
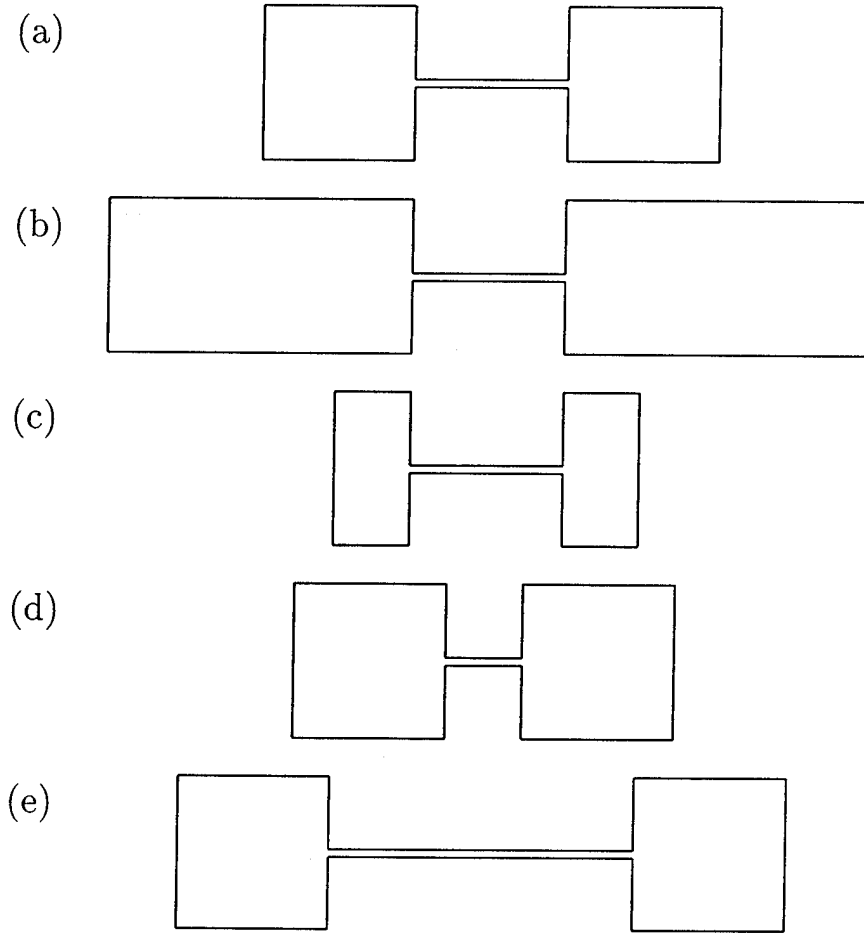
Figure 2: The five viscometer configurations used in numerical calculations reported here. The viscometers have the same cavity radius r_c and cavity lengths equal to r_c (c), $2r_c$ (a, d, e) and $4r_c$ (b). The duct lengths equal r_c (d), $2r_c$ (a, b, c), and $4r_c$ (e). Variable duct radii r_d in the range $0.02 \leq r_d/r_c \leq 0.5$ were studied.
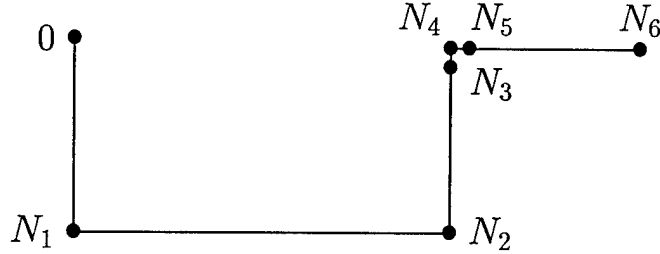
Figure 3: Mesh specification; the solid dots indicate node indices where the mesh size changes. A typical choice used was $N_1 = 40$, $N_2 = 120$, $N_3 = 160$, $N_4 = 220$, $N_5 = 280$, and $N_6 = 320$. This choice gives higher resolution in the region near the duct orifice.

j	N_j	$N_j - N_{j-1}$	$20h/r_c$
1	40	40	0.5
2	120	80	0.5
3	160	40	0.45
4	220	60	1/60
5	280	60	1/60
6	320	40	0.5

The mesh size h is specified in units of $r_c/20$ for the case $L_d = L_c = 2r_c$. Note that the mesh size is fairly uniform except for higher resolution regions near the duct edge.

Geometries with rounded orifice edges were also studied. The shape was modified as follows: In the cross-section of the orifice, the lines representing the duct wall and the baffle surrounding the orifice were joined by a 90° arc of radius $r_d/5$. Ten half-elements from each of the fine-mesh strips adjacent to the edge were assigned to the circular arc, so that the overall number of elements remained the same.

2.4   Dependence of eigenvalues on mesh size

Solutions were found for two sets of grids for cavity configuration (a) of Fig. 2. The total number of half-elements used was 320 for one case, distributed as

described in the table of the previous section, and 160 for the second case. The coarser mesh was obtained by halving the number of elements assigned to each region. As summarized in Table 2, the eigenvalues are determined with excellent accuracy for both mesh sizes. Further studies are advisable, however, to investigate the effects of the distribution of mesh sizes on the eigenvalues.

Unless otherwise noted, all results in this report were calculated with $N = 320$ half-elements.

r_d/r_c	k/k_0 ($N = 160$)	k/k_0 ($N = 320$)	% difference
0.05	0.980429	0.980407	0.002
0.10	0.962569	0.962548	0.002
0.15	0.946249	0.946231	0.002
0.20	0.931278	0.931263	0.002
0.25	0.917469	0.917456	0.001
0.30	0.904647	0.904636	0.001
0.35	0.892642	0.892632	0.001
0.40	0.881292	0.881283	0.001
0.45	0.870439	0.870431	0.0009
0.50	0.859927	0.859920	0.0008

Table 2: Calculations with configuration (a): $L_c = L_d = 2r_c$ and r_d variable; carried out with the total number of half-elements equal to 160 and 320, distributed as described in the text.

2.5   Eigenfunctions

The eigenfunctions for five values of r_d for the configuration (a) with $N = 320$ are shown in Fig. 4. (The eigenfunctions have been normalized to unity at maximum.) For the smallest duct radius the eigenfunction is nearly constant in the cavity, with a sharp transition to a linear region within the duct. As the duct radius is increased greater variation is seen within the cavity. Similar curves were observed for all geometries. Detailed comparisons of the eigenfunctions in the cavities and theory are presented in Part II of this report.

3   Velocity near orifice

The acoustic velocity field near the orifice is of great interest. The eigenfunctions can be interpreted as velocity potentials, so that the tangential velocity fields equal the derivatives of the eigenfunctions as functions of arc length. Figure 5 shows the derivative near the orifice of a configuration (a) resonator with $r_d/r_c = 1/20$. The figure shows plots for two shapes. The "sharp-edge" case is the standard $N = 320$ configuration (a). This plot has the expected cusp at the edge. The second plot corresponds to a rounded orifice. The numerical results indicate that the velocity cusp is smoothed by this procedure. Similar smoothing was obtained when the radius of curvature of the arc was reduced to $r_d/10$.

The smooth line in Fig. 5 has the expected theoretical form for solutions of the Helmholtz equation in two-dimensions near a 90° corner. Assume, for example, that a solid wall extends along the positive x-axis and the negative y-axis. Solutions expanded about the origin have the form

$$\Phi(r,\theta) = \sum_{m=1}^{\infty} A_m J_{2m/3}(kr) e^{2im\theta/3}. \tag{17}$$

The exponents of the angular function here are required to have a fractional form in order to satisfy a Neumann boundary condition on the surfaces $\theta = 0$ and $\theta = 3\pi/2$; from the separation of variables the same fractions must equal the orders of the Bessel functions. The leading term of the lowest-order Bessel function is proportional to $(kr)^{2/3}$. Here the polar coordinate r corresponds to the magnitude of the arc length s measured from the edge
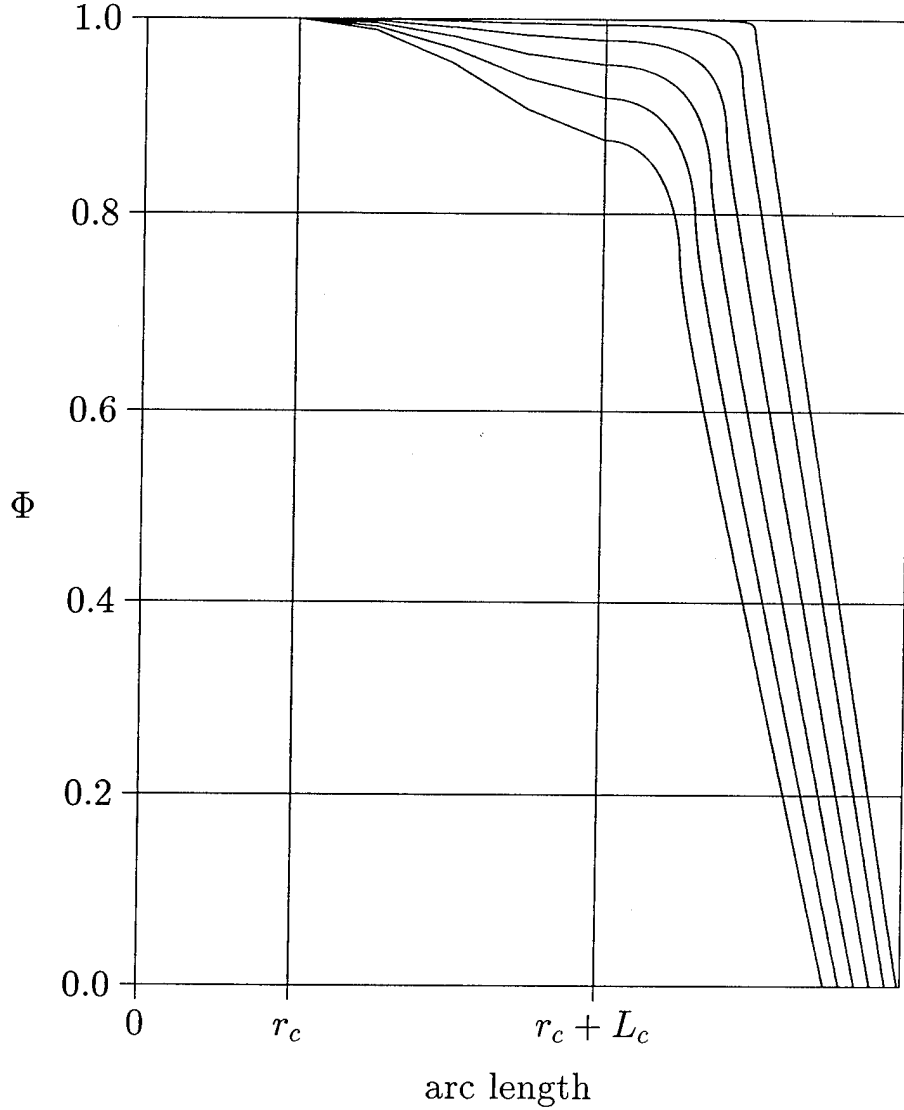
Figure 4: Eigenfunctions for viscometer configuration (a), computed with 320 half-elements and values of r_d/r_c equal to 0.02, 0.1, 0.2, 0.3, 0.4, and 0.5, corresponding to the curves from top to bottom. The eigenfunctions are normalized to unity at maximum, and plotted as a function of arc length within the cross-section of the viscometer, starting from 0 at the center of the cavity, to r_c at the rear edge, increasing by the cavity length L_c to the front corner, then increasing by $r_c - r_d$ to the duct orifice. The latter position varies with the curves and is not indicated. The right linear portions correspond to approximately uniform acoustic velocity within the duct.
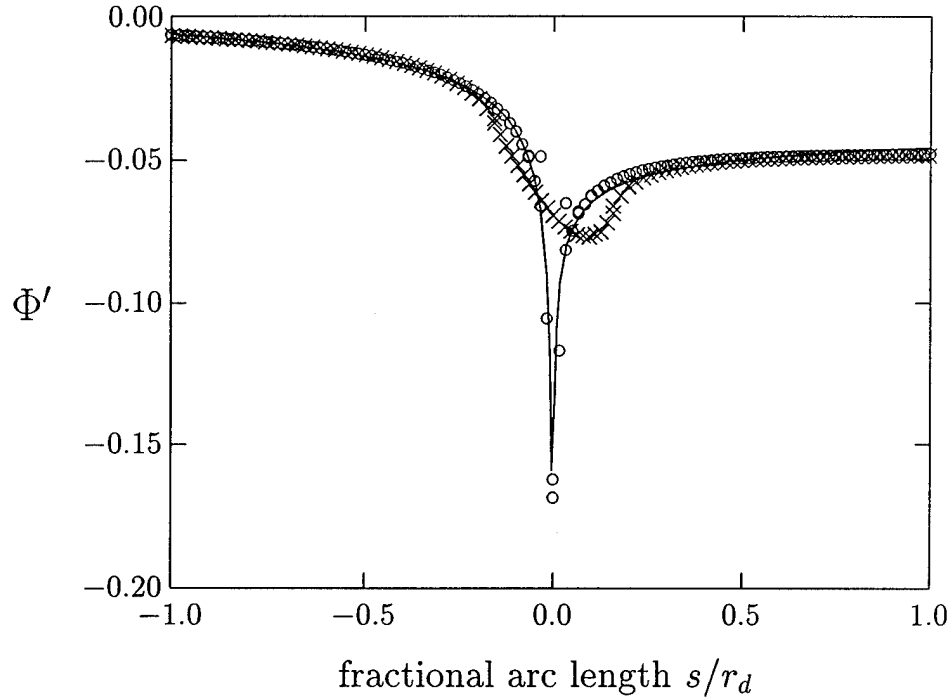
Figure 5: Numerical derivatives of the eigenfunction with respect to arc length, plotted in arc-length units relative to the duct edge. The smooth curves were separate fits to the $s > 0$ and $s < 0$ data with the form $A + B|s|^{-1/3}$. The points are for ducts with sharp edges ($\circ$) and ducts with edges rounded to $r_d/5$ ($\times$). The abscissae are measured from the orifice edge in the case when the latter is sharp, and from the mid-point of the arc in the rounded case. The latter convention is somewhat arbitrary and affects the position of the minimum in the figure.

of the orifice. Thus the eigenfunctions near the edge are expected to have a term proportional to $|s|^{2/3}$, and Φ' is accordingly expected to have a singular term proportional to $|s|^{-1/3}$. The smooth curve in the figure was obtained by separate fits to the form

$$\Phi'(s) = A + B|s|^{-1/3} \tag{18}$$

for the regions within the duct and on the baffle. The numerical calculations

clearly show that a cusp is present, but confined to a region within a small fraction of r_d from the edge.

4   Viscous losses

Dissipative effects have not been included in the numerical model presented here. However, some inferences can be drawn from the behavior of the computed eigenfunctions. Viscous losses on a surface are proportional to the square of the tangential velocity at the surface as long as the viscous penetration length is small compared with other dimensions, *e.g.* the duct radius. Thus the ratio of the surface integrals

$$\frac{\int_{\text{baffle}} \Phi'^2 \, dS}{\int_{\text{duct}} \Phi'^2 \, dS} = \frac{\int_{r=r_d}^{r_c} \Phi'^2 r \, dr}{\int_{z=0}^{L_d/2} \Phi'^2 r_d \, dz} \tag{19}$$

is an estimate of the relative importance of losses on the baffle surrounding the orifice to losses within the duct. These quantities can be evaluated numerically. Somewhat arbitrarily, the "edge" of the orifice for the rounded case has been defined to be the 45° point on the arc. With this definition, the ratios determined with sharp and rounded orifices are very consistent, as shown in Fig. 6. Both sets of data are approximately linear in r_d/L_d with a slope of approximately 0.4. [4]

---

[4]Later work revealed that there is an approximately equal contributionto the orifice resistance from the region just inside the duct. The total orifice resistance is thus approximately double the amount shown in the figure. (JBM, 23 March 1995).
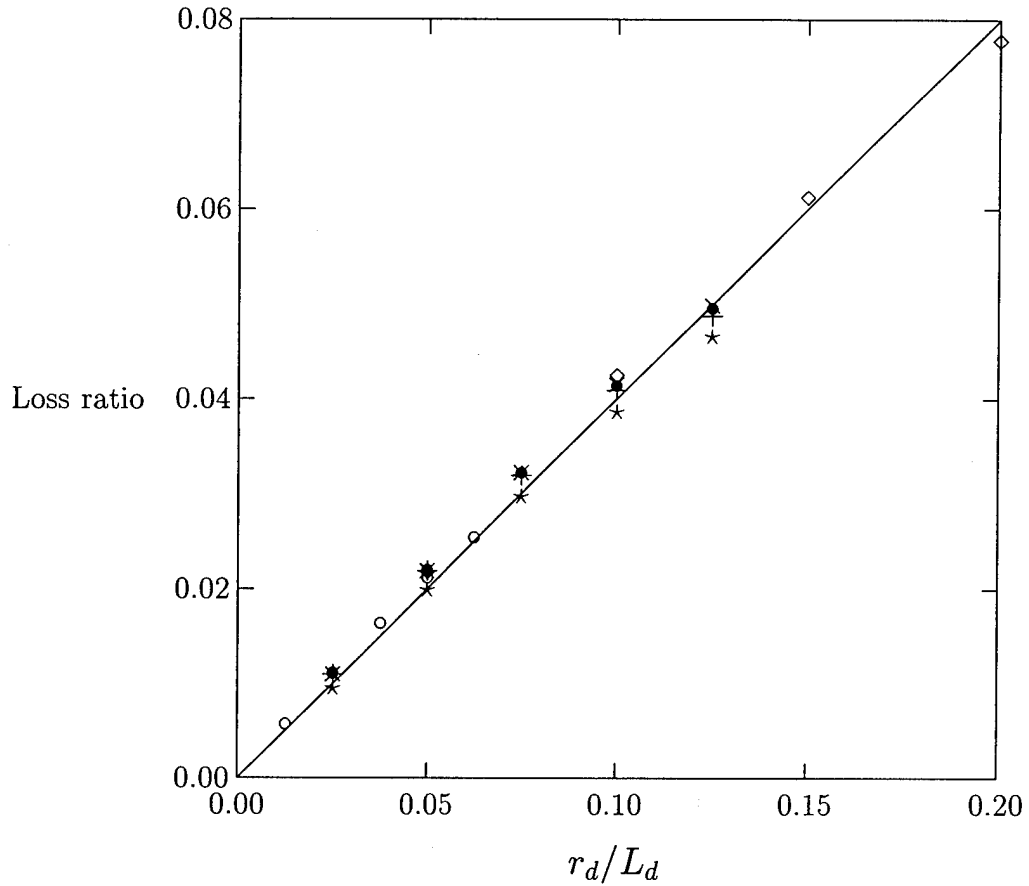
Figure 6: Ratio of viscous losses on baffle to those in duct as determined by numerical integration for orifices with sharp and rounded edges. The line has a slope of 0.793, an approximate fit to the sharp-edge data. The symbols correspond to numerical results for sharp-edged orifices with cavity dimensions: $L_c = L_d = 2r_c$ ($\bullet$); $L_c = r_c$, $L_d = 2r_c$ (+); $L_c = 4r_c$, $L_d = 2r_c$ ($\times$); $L_c = 2r_c$, $L_d = 4r_c$ ($\circ$); $L_c = 2r_c$, $L_d = r_c$ ($\diamond$). Rounded-edge orifice calculations were only carried out for the case $L_c = L_d = 2r_c$ ($\star$)

5 Mass end corrections

It is conventional to correct the lengths of ducts by a "mass end correction" δ to account for the inertial effects of the fluid just outside the orifice. Frequently the theoretical value $\delta = 8r_d/3\pi$, valid for radiation into a semi-infinite space from a duct with an infinite baffle, is also used for ducts terminating in cavities. Ingard's[5] extensive theoretical and experimental investigation of Helmholtz resonators includes a calculation of the "internal" mass end correction δ_i for a duct terminated by a cavity. This calculation is reconsidered in Part II of this report. Ingard's calculations showed that δ_i/r_d approximately equals $8/3\pi$ for small r_d/r_c, and decreases approximately linearly with increasing r_d/r_c. The present numerical calculations provide a means of testing the accuracy of Ingard's calculations.

An accurate comparison requires a careful analysis of the viscometer resonances. In Part II of this report it is shown that the input impedance of the cavities can be written, for the non-dissipative case, as

$$\mathbf{Z}_{\text{cavity}} = \frac{\rho c^2}{i\omega V}\frac{kL_c}{\tan kL_c} + \frac{i\omega\rho}{\pi r_d^2}\delta_i. \tag{20}$$

An improved resonance condition is obtained by replacing the cavity impedance $\mathbf{Z}_V$ in Eqs. (3) and (4) by $\mathbf{Z}_{\text{cavity}}$. The mass end-corrections can be calculated from numerical values of k/k_0 and this resonance condition. To obtain acceptable accuracy it is necessary to do this calculation carefully. Note that the tangent correction to the volume compliance term, when expanded to second order in kL_c, has the same order of magnitude as the mass end correction. Figure 7 shows results computed for the five resonator configurations. The numerical data overlap for small r_d/r_c and diverge slightly for larger ducts. The smooth line represents the theoretical values based on Ingard's theory. The theoretical values depend only weakly on cavity dimensions other than r_d/r_c; the differences are invisible in the graph. Figure 8 shows the difference between the theoretical and numerical values of δ_i/r_d. The theoretical values are all high by amounts which which lie in the range 0.02-0.03, varying weakly with r_d/r_c.

The difference between the theoretical and numerical values of δ_i/r_d for may be due to the assumption of a uniform velocity within the duct orifice.

---

[5]K. Ingard, *J. Acoust. Soc. Am.*, **25**, 1037–1061 (1953).

Ingard,[6] referring to his experimental values of δ_i/r_d, commented: "The measured values are consistently somewhat smaller than the calculated. This is expected from the fact that any assumed velocity distribution different from the correct one gives an end correction which is always too big."

An improved theory of the viscometer could yield the theoretical velocity distribution in the orifice. Alternatively, the BIE numerical technique could be extended to calculate the velocity distribution in the orifice.[7] Either approach would probably be of little use in understanding practical viscometers, however, because the viscous effects on the velocity in the duct are likely to be much greater.

---

[6] *op. cit.*

[7] Subsequent to the original completion of this report, numerical calculations of the the z-component of the acoustic velocity in the orifice were made. The results show the expected singular behavior near the orifice edge. In future work this numerical velocity field will be used together with analytic expressions for the fields in the cavity to obtain improved estimates of the inertial end corrections. (JBM, 29 January 1995)
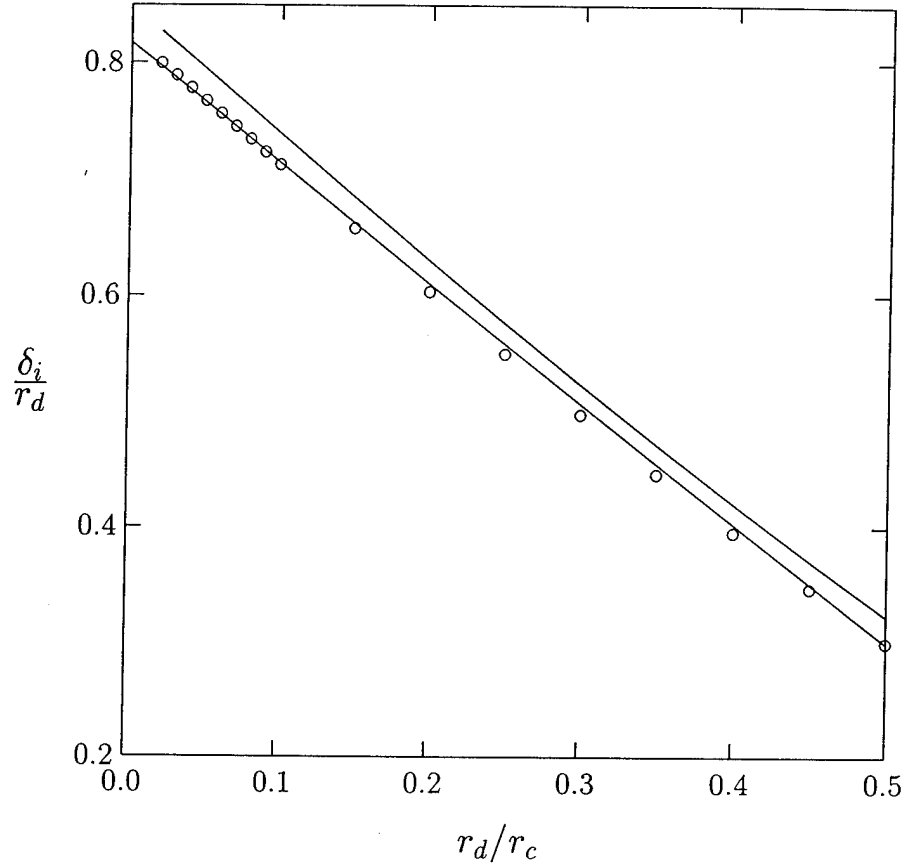
Figure 7: Mass end corrections for duct connected to cavity. The open symbols correspond to numerical results for all five cavities; small differences between the cavities cannot be differentiated on the scale of the graph either in the calculated line nor the numerical results. The lower line is a best fit to the numerical results, with an intercept 0.817 ± 0.003 and slope -1.053 ± 0.005.
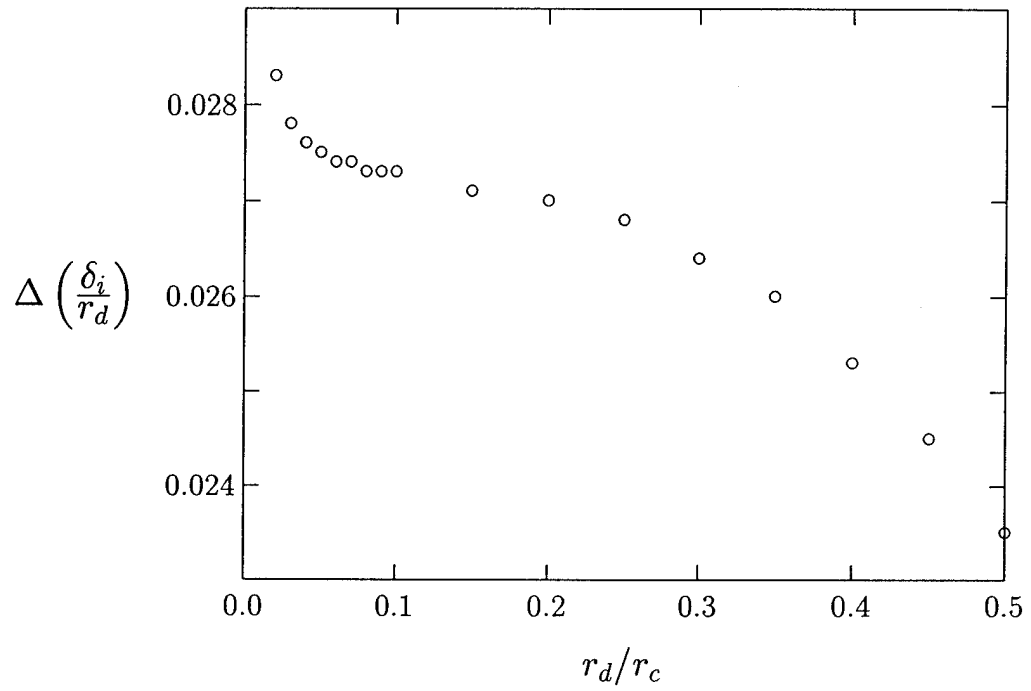
$$\Delta \left(\frac{\delta_i}{r_d} \right)$$

Figure 8: Mass end corrections for duct connected to cavity, plotted as theory minus numerical calculations. The symbols correspond to numerical results for all five cavities; small differences between the cavities cannot be differentiated on the scale of the graph.

6 Summary

The important numerical results of this work are:

- The ratio of viscous losses on the baffle around the duct orifice to losses within the duct has been calculated for both sharp and rounded edge orifices. Both sets of results are approximately described by a linear relationship

$$\text{loss ratio} \approx 0.79 r_d / L_d.$$

- The Ingard mass end correction has been shown to be higher than numerical values by an amount in the range 0.02–0.03. The difference, which depends weakly on the ratio of the duct radius to the cavity radius, may be due to Ingard's (and Rayleigh's) approximation of the field in the duct orifice as uniform (piston).

Design of acoustic devices for the accurate and precise measurement of transport properties of pure and mixed gases
Part II
Greenspan Viscometer:
Improved Theory

by

James B. Mehl
1014 Baylor Drive
Nottingham Green
Newark, DE 19711-3130

1

Abstract

An acoustic viscometer based on a double-Helmholtz resonator was described by Greenspan and Wimenitz in 1953.[1] This report describes new theoretical results for interpretation of measurements with this type of resonator, for which the name *Greenspan viscometer* has been proposed. A Green's function formalism has been used to calculate the pressure and velocity fields in the viscometer cavities. The fields are shown to be in excellent agreement with numerical calculations. The input impedance of the cavity was calculated and shown to equal the sum of a volume compliance term and a mass end correction. The effects of viscous and thermal boundary layer effects on these terms was calculated.

Contents

---

[1]Martin Greenspan and Francis N. Wimenitz, *An Acoustic Viscometer for Gases – I*, NBS Report 2658 (1953).

1   Introduction

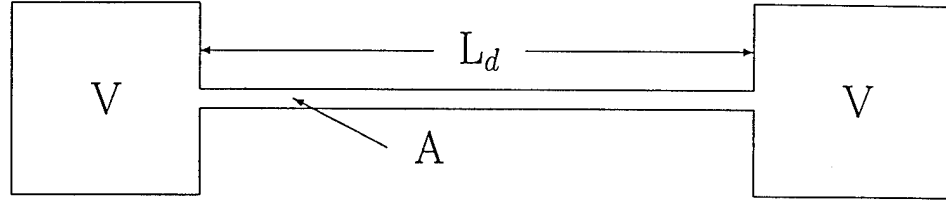The geometry is defined in Fig. 1. The theory of the viscometer is described

Figure 1: Schematic representation of a Greenspan viscometer.

by first presenting a simple model to introduce notation and characteristic dimensions. Subsequent sections deal separately with better models of the flow in the coupling duct and the cavities. A final section updates the theory of viscometer resonances. Table 1 summarizes the notation.

In the lowest order of approximation the duct can be treated as a uniformly moving mass of gas with an acoustic impedance equal to the product of $i\omega$ and the mass per unit cross-sectional duct area of the gas: $\mathbf{Z}_d = i\omega\rho L_d/A$. Each cavity has an acoustic impedance $\mathbf{Z}_V = \rho c^2/(i\omega V)$. A resonance condition is obtained by setting the total series impedance of the viscometer equal to zero

$$2\mathbf{Z}_V + \mathbf{Z}_d = 2\rho c^2/(i\omega V) + i\omega\rho L_d/A = 0. \tag{1}$$

The resonances occur at $\omega = ck_0$, where

$$k_0^2 = \frac{2A}{VL_d} = \frac{2r_d^2}{r_c^2 L_c L_d}. \tag{2}$$

Under typical conditions the duct radius is much smaller than the other dimensions, so that products like $k_0 r_c$, $k_0 L_c$, and $k_0 L_d$ are small compared with unity.

2   Acoustic flow in ducts

A more complete account of the acoustic flow in the duct is based on the fourth-order partial differential equation for the temperature introduced by

ω	$2\pi \times$ frequency
ρ	density of the gas
c	speed of sound in the gas
C_P, C_V	specific heats per unit mass of gas
$\gamma = C_P/C_V$	specific heat ratio
η	viscosity of the gas
κ	thermal conductivity of the gas
$\delta_v = \sqrt{\eta/\rho}$	viscous penetration length
$\delta_t = \sqrt{\kappa/\rho C_P}$	thermal penetration length
r_d	duct radius
$A = \pi r_d^2$	cross-sectional area of duct
L_d	length of duct
$V = \pi r_c^2 L_c$	cavity volume (one cavity)
L_c	cavity length
r_c	cavity radius
S	surface area of cavity

Table 1: Notation

Kirchhoff.[2] It is convenient to use the equivalent circuit parameters $\mathcal{Z}$ and $\mathcal{Y}$, and the related propagation parameter $\boldsymbol{\Gamma}$ and characteristic impedance $\mathbf{Z}_0$. These quantities are defined in the literature.[3] The series impedance $\mathcal{Z}$ and shunt admittance $\mathcal{Y}$ equal

$$\mathcal{Z} = \frac{i\omega\rho}{A}\frac{1}{1-F_v}, \qquad \mathcal{Y} = \frac{i\omega A}{\rho c^2}[1+(\gamma-1)F_t], \qquad (3)$$

where the functions F_v and F_t are defined to be

$$F = \frac{2J_1(\zeta)}{\zeta J_0(\zeta)}. \qquad (4)$$

---

[2]G. Kirchhoff, Über den Einfluss der Wärmeleitung in einem Gase auf die Schallbewegung, *Ann. Physik Chem. (Fifth Ser.)*, 134:177–193, 1868; English translation "On the Influence of Heat Conduction in a Gas on Sound Propagation," by R. B. Lindsay in *Benchmark Papers in Acoustics: Physical Acoustics*, R. B. Lindsay, Ed., Dowden, Hutchinson, & Ross, Stroudsburg, Pennsylvania (1974), pp. 7–19.

[3]For a recent review see Douglas H. Keefe, *J. Acoust. Soc. Am.* **75**, 58–62 (1984).

Here $\zeta = (1-i)r_d/\delta_v$ for F_v and $(1-i)r_d/\delta_t$ for F_t, and J_0 and J_1 are Bessel functions. For small values of δ_v/r_d the approximations

$$F_v \approx (\delta_v/r_d)(1-i), \quad F_t \approx (\delta_t/r_d)(1-i) \tag{5}$$

are adequate.

The characteristic impedance $\mathbf{Z}_0$ and propagation parameter $\boldsymbol{\Gamma}$ for acoustic flow in the duct are

$$\mathbf{Z}_0 = \sqrt{\mathcal{Z}/\mathcal{Y}} = \frac{\rho c}{A} \frac{1}{\sqrt{(1-F_v)[1+(\gamma-1)F_t]}}$$

$$\boldsymbol{\Gamma} = \sqrt{\mathcal{Z}\mathcal{Y}} = \frac{i\omega}{c}\sqrt{\frac{1+(\gamma-1)F_t}{1-F_v}}. \tag{6}$$

The relations

$$\mathcal{Z} = \mathbf{Z}_0 \boldsymbol{\Gamma} \quad \text{and} \quad \mathcal{Y} = \boldsymbol{\Gamma}/\mathbf{Z}_0 \tag{7}$$

are also useful.

3 Acoustic cavity coupled to duct

Consider a cylindrical cavity of radius r_c and length L_c concentric with a cylindrical coordinate system. Let the cavity be coupled to a circular duct of radius r_d in the $z = 0$ plane. The objective of this section is calculation of the pressure and velocity fields in the cavity, and the acoustic impedance of the duct orifice, when the cavity is excited by acoustic flow in the duct.

3.1 Formal solution

Let the cavity C be bound by a rigid surface S. Consider the Green's function describing non-dissipative acoustic fields

$$G(\mathbf{r}, \mathbf{r}') = \sum_N \frac{\Phi_N(\mathbf{r})\Phi_N(\mathbf{r}')}{V\Lambda_N(k_N^2 - k^2)}, \tag{8}$$

where $k = \omega/c$. The eigenfunctions Φ_N are a complete orthogonal set satisfying

$$(\nabla^2 + k_N^2)\Phi_N(\mathbf{r}) = 0, \quad \mathbf{r} \in C$$

$$\frac{\partial \Phi_N}{\partial n} = 0, \quad \mathbf{r} \in S, \tag{9}$$

where C represents the cavity bound by a surface S. The Green's function satisfies

$$(\nabla^2 + k^2)G(\mathbf{r}, \mathbf{r}') = -\delta(\mathbf{r} - \mathbf{r}'), \quad \mathbf{r} \in C$$

$$\frac{\partial G}{\partial n} = 0, \quad \mathbf{r} \in S. \tag{10}$$

The acoustic pressure in the cavity is assumed to satisfy

$$(\nabla^2 + k^2)p(\mathbf{r}) = 0, \quad \mathbf{r} \in C$$

$$\frac{\partial p}{\partial n} = -i\omega\rho u_n, \quad \mathbf{r} \in S, \tag{11}$$

where u_n is the outward velocity of the surface at $\mathbf{r}$, assumed to be zero everywhere except over the duct orifice, where it will be approximated by a constant value $-u_0$. The acoustic pressure can be expressed in terms of the Green's function as

$$p(\mathbf{r}') = i\omega\rho u_0 \int_{\text{orifice}} G(\mathbf{r}, \mathbf{r}') \, dS. \tag{12}$$

This integral will vanish for all modes Φ_N except the radially symmetric ones given by

$$\Phi_{nl} = J_0(z_{0n}r/r_c)\cos(l\pi z/L_c), \tag{13}$$

where z_{0n} is the nth root of $J_0'(z) = -J_1(z) = 0$. The normalization integral is

$$V\Lambda_{nl} = \pi r_c^2 L_c[J_0(z_{0n})]^2/\epsilon_l \tag{14}$$

where $\epsilon_l = 2 - \delta_{l0}$ is the Neumann symbol and the eigenvalues are

$$k_{nl}^2 = (z_{0n}/r_c)^2 + (l\pi/L_c)^2. \tag{15}$$

The integral needed for the pressure is

$$\int_0^{r_d} J_0(z_{0n}r/r_c)\, 2\pi r \, dr = 2\pi J_1(z_{0n}r_d/r_c)r_d r_c/z_{0n}, \tag{16}$$

where r_d is the duct radius. The pressure in the cavity is thus

$$p(r, z) = \frac{2i\omega\rho u_0 r_d}{L_c r_c} \sum_{nl} \frac{J_1(z_{0n}r_d/r_c)J_0(z_{0n}r/r_c)\cos(l\pi z/L_c)\epsilon_l}{z_{0n}[J_0(z_{0n})]^2[(z_{0n}/r_c)^2 + (l\pi/L_c)^2 - k^2]}. \tag{17}$$

3.2 Pressure and velocity fields

Expressions for the pressure and velocity fields in the region surrounding the orifice and along the cylindrical walls are useful for comparison with numerical calculations. It is convenient to separate off the contribution of the $0n$-modes in Eq. (17), for which the Bessel terms should be replaced by the limiting forms

$$\lim_{\zeta \to 0} \frac{J_1(\zeta r_d/r_c) J_0(\zeta r/r_c)}{\zeta [J_0(\zeta)]^2} = \frac{r_d}{2r_c}. \tag{18}$$

In convenient dimension-less units, the pressure is thus

$$\frac{p(r,z)}{\rho c u_0} = \frac{ikr_d^2}{L_c r_c^2} \sum_{l=0}^{\infty} \frac{\epsilon_l \cos(l\pi z/L_c)}{(l\pi/L_c)^2 - k^2}$$

$$+ \frac{2ikr_d}{L_c r_c} \sum_{n=1}^{\infty} \frac{J_1(z_{0n}r_d/r_c) J_0(z_{0n}r/r_c)}{z_{0n}[J_0(z_{0n})]^2} \sum_{l=0}^{\infty} \frac{\epsilon_l \cos(l\pi z/L_c)}{[(z_{0n}/r_c)^2 + (l\pi/L_c)^2 - k^2]}. \tag{19}$$

The sums over l can be evaluated in closed form using[4]

$$\sum_{l=0}^{\infty} \frac{\epsilon_l \cos(\beta l)}{l^2 + \alpha^2} = \frac{\pi \cosh[\alpha(\pi - \beta)]}{\alpha \sinh(\pi\alpha)}. \tag{20}$$

For the first sum $\alpha = ikL_c/\pi$ and $\beta = \pi z/L_c$, so that

$$\sum_{l=0}^{\infty} \frac{\epsilon_l \cos(l\pi z/L_c)}{(l\pi/L_c)^2 - k^2} = L_c \frac{\cosh[ikL_c(1 - z/L_c)]}{ik \sinh(ikL_c)} = -L_c \frac{\cos k(L_c - z)}{k \sin kL_c}. \tag{21}$$

In the second sum $\alpha = (z_{0n}L_c/\pi r_c)\eta_n$, where $\eta_n = \sqrt{1 - (kr_c/z_{0n})^2} \approx 1$, and β is unchanged. The sum is

$$\sum_{l=0}^{\infty} \frac{\epsilon_l \cos(l\pi z/L_c)}{[(z_{0n}/r_c)^2 + (l\pi/L_c)^2 - k^2]} = L_c r_c \frac{\cosh[z_{0n}\eta_n(L_c - z)/r_c]}{z_{0n}\eta_n \sinh(z_{0n}\eta_n L_c/r_c)}. \tag{22}$$

---

[4]V. Mangulis, *Handbook of Series for Scientists and Engineers*, Academic (1965), pp. 99–100; Eldon Hansen, *A table of series and products*, Prentice-Hall (1975), p. 243.

The pressure simplifies to

$$\frac{p(r,z)}{\rho c u_0} = -i\frac{r_d^2}{r_c^2}\frac{\cos k(L_c - z)}{\sin kL_c}$$
$$+ 2ikr_d \sum_{n=1}^{\infty} \frac{J_1(z_{0n}r_d/r_c)J_0(z_{0n}r/r_c)}{[z_{0n}J_0(z_{0n})]^2}\frac{\cosh[z_{0n}\eta_n(L_c - z)/r_c]}{\eta_n \sinh(z_{0n}\eta_n L_c/r_c)}. \tag{23}$$

The pressure on the $z = 0$ surface is

$$\frac{p(r,0)}{\rho c u_0} = -\frac{ir_d^2}{r_c^2 \tan kL_c} + 2ikr_d \sum_{n=1}^{\infty} \frac{J_1(z_{0n}r_d/r_c)J_0(z_{0n}r/r_c)}{[z_{0n}J_0(z_{0n})]^2}\frac{\coth[(z_{0n}\eta_n L_c/r_c)}{\eta_n}. \tag{24}$$

For values of k near k_0 the quantity η_n is on the order of $1 - 2r_d^2/(L_cL_dz_{0n}^2)$, which typically differs from unity by a negligible amount. Noting further that $z_{01} \approx 3.83$ and that $\tanh(3.83) \approx 0.999$, the hyperbolic cotangent term can generally be approximated by unity for cavities with $L_c > r_c$. In the limit where both η_n and the hyperbolic cotangent are approximated by unity the sum in Eq. (24) is independent of k. While in practice there is no need to make the approximation in computer calculations, the calculations reported here the approximations are excellent in nearly all cases. The simplified expression for the pressure is

$$\frac{p(r,0)}{\rho c u_0} = -\frac{ir_d^2}{r_c^2 \tan kL_c} + 2ikr_d \sum_{n=1}^{\infty} \frac{J_1(z_{0n}r_d/r_c)J_0(z_{0n}r/r_c)}{[z_{0n}J_0(z_{0n})]^2}. \tag{25}$$

The radial velocity at $z = 0$ is

$$\frac{u_r(r,0)}{u_0} = \frac{i}{\rho c k u_0}\frac{\partial p}{\partial r} = \frac{2r_d}{r_c}\sum_{n=1}^{\infty} \frac{J_1(z_{0n}r_d/r_c)J_1(z_{0n}r/r_c)}{z_{0n}[J_0(z_{0n})]^2}. \tag{26}$$

The pressure along the cavity sides is (in the same limits)

$$\frac{p(r_c,z)}{\rho c u_0} = -\frac{ir_d^2}{r_c^2}\frac{\cos k(L_c - z)}{\sin kL_c} + 2ikr_d \sum_{n=1}^{\infty} \frac{J_1(z_{0n}r_d/r_c)}{z_{0n}^2 J_0(z_{0n})}\frac{\cosh[z_{0n}(L_c - z)/r_c]}{\sinh(z_{0n}L_c/r_c)}. \tag{27}$$

The tangential velocity along the edge is thus

$$\frac{u_z(r_c, z)}{u_0} = \frac{r_d^2}{r_c^2} \frac{\sin k(L_c - z)}{\sin k L_c} + \frac{2r_d}{r_c} \sum_{n=1}^{\infty} \frac{J_1(z_{0n} r_d/r_c)}{z_{0n} J_0(z_{0n})} \frac{\sinh[z_{0n}(L_c - z)/r_c]}{\sinh(z_{0n} L_c/r_c)}.$$

(28)

3.3 Numerical tests

It is useful to compare the theoretical representation of the fields described here with the BIE numerical results. Except when noted otherwise, all numerical results will refer to cavities with $r_d/r_c = 1/20$, and $L_d = L_c = 2r_c$. Numerical calculations were carried out for duct orifices with sharp edges and with rounded edges. Consider the cross-section where the duct intersects the cavity. The rounding corresponds to a $90°$ circular arc connecting the duct wall with the plane cavity wall. The results referred to here correspond to an arc radius equal to $r_d/5$. (Similar results were obtained with other arc sizes.)

The numerical calculations yield values of the velocity potential Φ on the cavity boundary. These values permit the velocity potential to be determined within the cavity as well. However, such calculations will not be described here. In addition to the velocity potential it is possible to obtain the velocity by numerical differentiation. A convenient dimension-less ratio for the pressure is the quantity $k\Phi/\Phi_0' = -p/(i\rho c u_0)$, where Φ_0', the derivative in the duct, corresponds to the source velocity u_0. The numerical calculations show that Φ' is vary accurately linear in the axial displacement from the duct center, except for deviations near the orifice. (Because of the symmetry of the calculated models, and the emphasis in this section on a single cavity, the singular will be used to refer to the cavity, the orifice, etc.) For both the sharp-edged and rounded orifices, over 95% of the duct length the agreement of Φ with the best lines through the origin is better than 0.01%; near the orifice the departures from linearity remain less than 0.8%. Thus reasonably well-defined values of Φ_0' can be obtained from these fits. Figure 2 shows the acoustic pressure on the cavity wall at the orifice. The numerical results agree very well with calculations, except that both the sharp- and rounded-edge numerical data fall slightly (about 0.05%) below the theoretical curves. This is within the range of variation of Φ' in the duct, and may be related to the non-uniformity of the source velocity within the orifice. Figure 3 shows
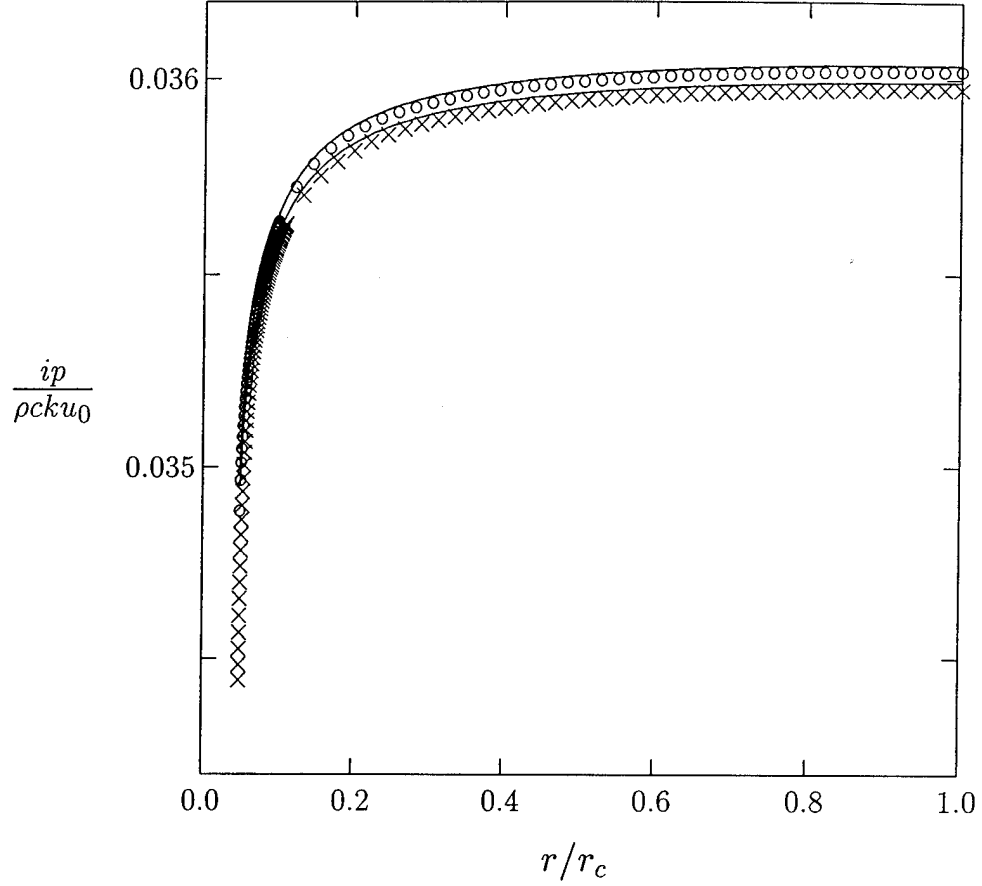
Figure 2: Pressure field at the "baffle" end of a cylindrical cavity with a radius r_c, as a function of the fractional radial coordinate r/r_c. The smooth line was calculated for a uniform source of velocity u_0 in the range $r \leq r_d$, with $r_d/r_c = 0.05$. The discrete points are for numerical calculations of the field in a Greenspan viscometer with a cavity length $L_c = 2r_c$ and a duct orifice with (o) sharp edges, and (×) edges rounded to a radius of curvature $r_d/5$. The numerical data fall about 0.05% below the calculated curve for larger values of r/r_c. This may be due to the choice of Φ_0' used in the analysis or to the assumption of a uniform source velocity.

that the numerical and theoretical values of the radial velocity $u_r(r,0)$ agree over nearly five orders of magnitude. Little difference is seen between the results for sharp and rounded edges.

Greater insight is obtained by considering a model based on the assumption of radial flow at moderate distances from the orifice. The volume flux at the orifice is $\pi r_d^2 u_0$. A transition to approximate radial flow over a length scale on the order of r_d is a plausible assumption, as suggested by Moldover.[5] For radial flow into a solid angle 2π the expected velocity is $u_0 r_d^2/(2r^2)$. As a test of this hypothesis the quantity $2u_r r^2/(u_0 r_d^2)$ is plotted in Fig. 4. Small differences between the sharp- and rounded-edge cases can be observed just outside the orifice (at $r_d/r_c = 0.05$); a transition to radial flow occurs within one or two duct radii of the orifice. Eventually the velocity goes to zero to satisfy the boundary condition at $r = r_c$.

Finally, Figs. 5 and 6 show that the numerical and calculated pressure and velocity fields agree along the cylinder wall. In summary, noting that there are no free parameters in the comparisons of the pressure and velocity fields in the cavity, one can conclude that the theory described in this section gives an excellent account of the cavity behavior.

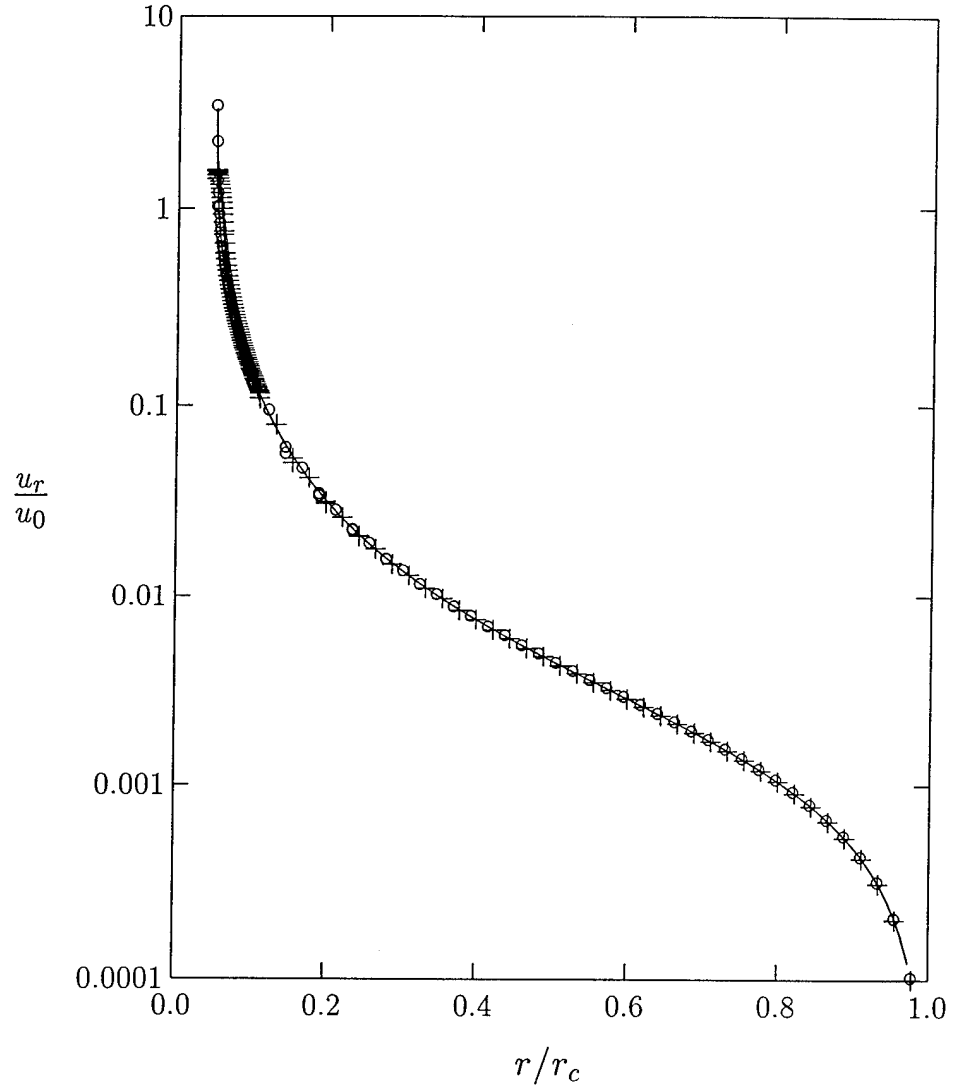[5]Michael R. Moldover, private communication.

Figure 3: Radial velocity fields on the "baffle" end of a cylindrical cavity with a radius r_c as a function of the fractional radial coordinate r/r_c. The smooth line was calculated for a uniform source of velocity u_0 in the range $r \leq r_d$, with $r_d/r_c = 0.05$. The discrete points are for numerical calculations of the fields in Greenspan viscometers with cavities of length $L_c = 2r_c$: $\circ$, duct orifice with sharp edge; $+$, duct orifice with edges rounded to a radius of curvature $r_d/5$.
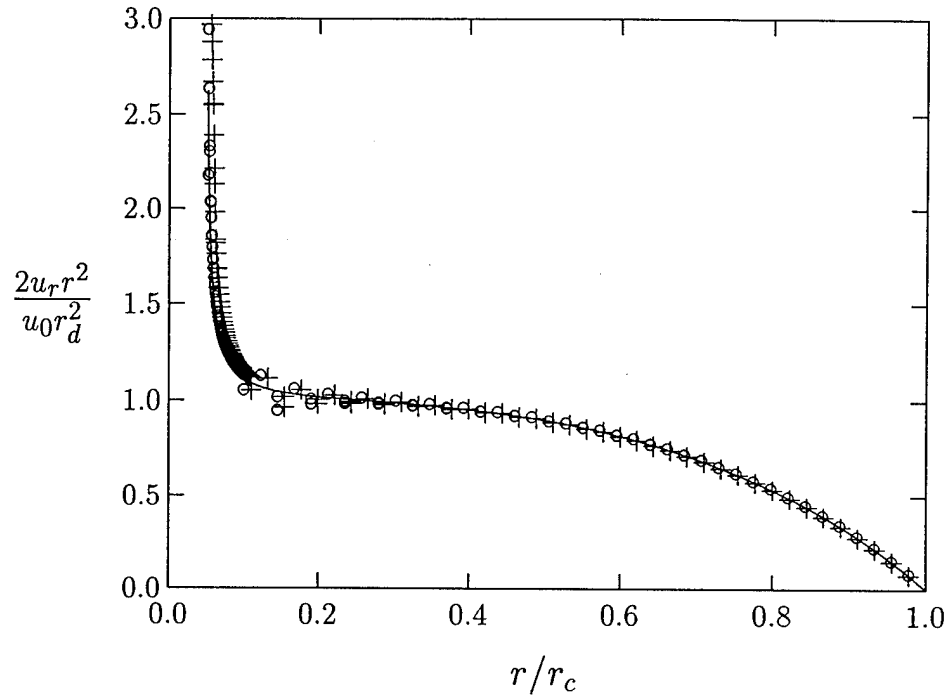
Figure 4: Radial velocity fields on the "baffle" end of a cylindrical cavity with a radius r_c, weighted by a factor $2(r/r_d)^2/u_0$, as a function of the fractional radial coordinate r/r_c. The smooth line was calculated for a uniform source of velocity u_0 in the range $r \leq r_d$, with $r_d/r_c = 0.05$. The discrete points are for numerical calculations of the fields in Greenspan viscometers with cavities of length $L_c = 2r_c$: o, duct orifice with sharp edge; +, duct orifice with edges rounded to a radius of curvature $r_d/5$.
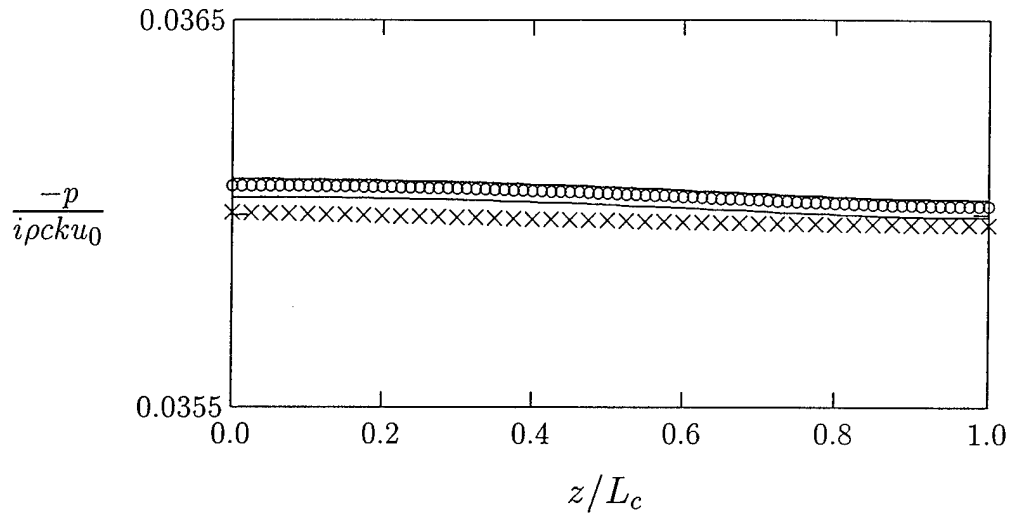
Figure 5: Pressure field on the cylindrical surface $r = r_c$ of a cavity as a function of the fractional axial coordinate z/L_c. The smooth line was calculated for a uniform source of velocity u_0 in the range $r \leq r_d$, with $r_d/r_c = 0.05$. The discrete points are for numerical calculations of the fields in a Greenspan viscometer with a cavity length $L_c = 2r_c$ cavities of length $L_c = 2r_c$: ○, duct orifice with sharp edge; ×, duct orifice with edges rounded to a radius of curvature $r_d/5$. As in Fig. 2, the numerical data fall about 0.05% below the calculated lines.
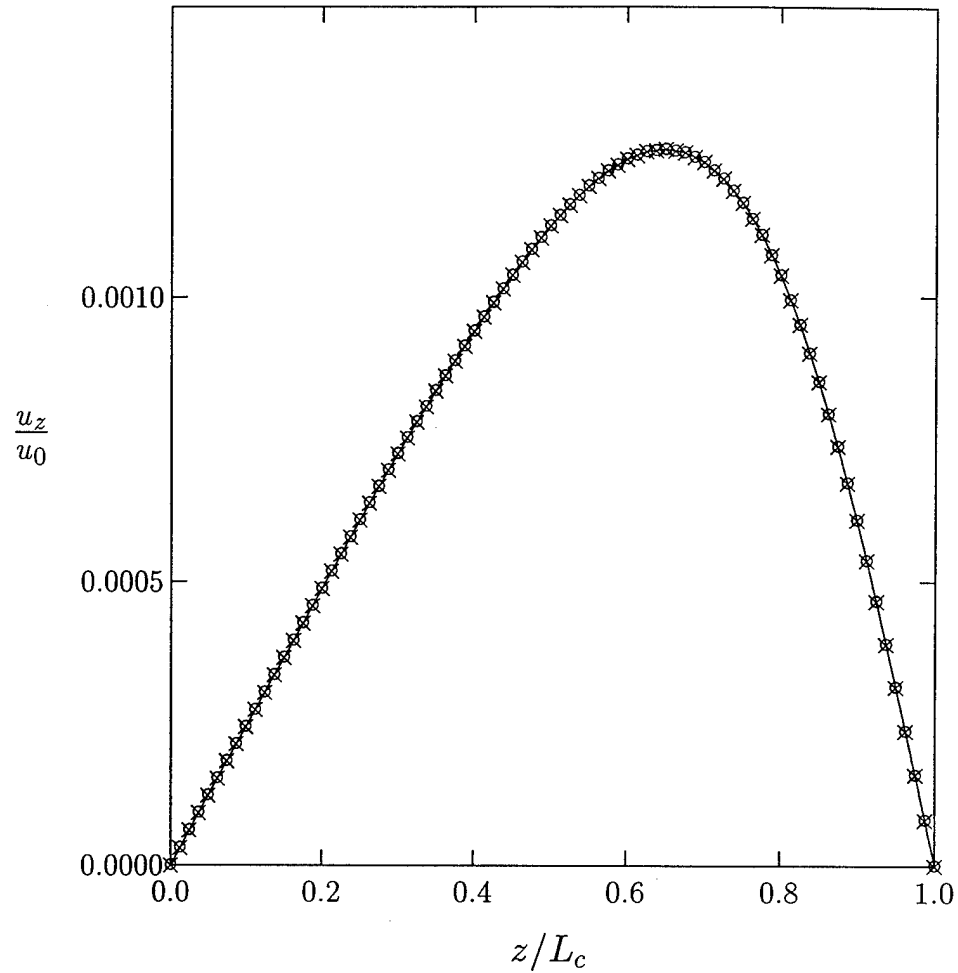
Figure 6: Axial velocity fields on the surface $r = r_c$ of a cylindrical cavity of radius r_c as a function of the fractional coordinate z/L_c. The smooth line was calculated for a uniform source of velocity u_0 at $z = 0$ in the range $r \leq r_d$, with $r_d/r_c = 0.05$. The discrete points are for numerical calculations of the fields in Greenspan viscometers with cavities of length $L_c = 2r_c$: $\circ$, duct orifice with sharp edge; $\times$, duct orifice with edges rounded to a radius of curvature $r_d/5$. Note that the maximum velocity is relatively small, comparable with the value of u_r in $0.75r_c \leq r \leq r_c$.

3.4   Cavity input impedance

The input impedance of the cavity is important for modeling the viscometer. The mean pressure at the orifice is given by

$$
\frac{\bar{p}}{\rho c u_0} = \frac{1}{\rho c u_0 \pi r_d^2} \int_0^{r_d} p(r,0) 2\pi r \, dr
$$

$$
= \frac{r_d^2}{i r_c^2 \tan k L_c} + 4ikr_c \sum_{n=1}^{\infty} \left[\frac{J_1(z_{0n} r_d/r_c)}{z_{0n} J_0(z_{0n})} \right]^2 \frac{\coth[(z_{0n}\eta_n L/r_c)}{\eta_n}. \tag{29}
$$

The acoustic input impedance of the cavity (pressure/volume velocity) is

$$
\mathbf{Z}_{\mathrm{in}} = \frac{\bar{p}}{\pi r_d^2 u_0}
$$

$$
= \frac{\rho c}{i \pi r_c^2 \tan k L_c} + \frac{4i\rho c k r_c}{\pi r_d^2} \sum_{n=1}^{\infty} \left[\frac{J_1(z_{0n} r_d/r_c)}{z_{0n} J_0(z_{0n})} \right]^2 \frac{\coth[(z_{0n}\eta_n L/r_c)}{\eta_n}. \tag{30}
$$

The first term is

$$
\mathbf{Z}_{\mathrm{in}}^{(n=0)} = \frac{\rho c^2}{i\omega V} \frac{k L_c}{\tan k L_c}, \tag{31}
$$

equal to the zero-order expression for the input impedance of the cavity modified by a frequency-dependent factor

$$
k L_c / \tan(k L_c) = 1 - (k L_c)^2/3 + O(k L_c)^4. \tag{32}
$$

Following Ingard,[6] the other terms in the sum can be interpreted in terms of an effective specific acoustic inertance $i\omega\rho\delta_i$, where δ_i is an effective length correction for a duct terminated by the cavity, i.e. an internal end correction, given by

$$
\delta_i = 4r_c \sum_{n=1}^{\infty} \left[\frac{J_1(z_{0n} r_d/r_c)}{z_{0n} J_0(z_{0n})} \right]^2 \frac{\coth[(z_{0n}\eta_n L/r_c)}{\eta_n}. \tag{33}
$$

This differs from Ingard's expression only in the hyperbolic cotangent and η_n factors. As noted previously, the hyperbolic cotangent function is already nearly unity for the $n = 1$ term, and $\eta_n \approx 1$ to a very high degree of accuracy. Thus the two expressions are in practice nearly identical.

---

[6]Uno Ingard, "On the Theory and Design of Acoustic Resonators," J. Acoust. Soc. Am., **25** 1037–1061 (1953).

The separation of the cavity impedance into a compliance term and an effective mass term is not unique. For example, the first correction term Eq. (32) has the same frequency signature as a constant effective mass term. However, the chosen formulation has the advantage of the correct limiting behavior as $r_d \rightarrow r_c$.

3.5 Dissipative effects

Dissipative effects owing to the viscous and thermal boundary layers in the cavity can be included by using the Green's function satisfying viscothermal boundary conditions.

The perturbed eigenfunctions and eigenvalues can be written

$$\Psi_{nl} = J_0(q_n r) \cos(\kappa_l z + \theta_l), \qquad k_{nl}^2 = q_n^2 + \kappa_l^2, \tag{34}$$

where q_n, κ_l, and θ_l are complex parameters determined by the boundary condition

$$\frac{\partial \Psi_{nl}}{\partial n} = -ik\beta \Psi_{nl}. \tag{35}$$

According to viscothermal boundary-layer theory, the specific acoustic impedance ratio β satisfies

$$2ik\beta = (-1 + i)k^2[(\gamma - 1)\delta_t + (k_t^2/k^2)\delta_v], \tag{36}$$

where k_t^2 is the transverse component of k_{nl} for the mode under consideration, *i.e.* $k_t^2 = -\nabla_t^2 \Psi_{nl}/\Psi_{nl}$. Appropriate expressions for the cylindrical sides and plane ends of the cavity are

$$2ik\beta_{\text{side}} = (-1 + i)[(\gamma - 1)k^2\delta_t + (l\pi/L_c)^2\delta_v]$$
$$2ik\beta_{\text{ends}} = (-1 + i)[(\gamma - 1)k^2\delta_t + (z_{0n}/r_c)^2\delta_v]. \tag{37}$$

Approximate solutions for the eigenvalues components are

$$q_0^2 = 2ik\beta_{\text{side}}/r_c$$

$$q_n = \frac{z_{0n}}{r_c} + \frac{ik}{z_{0n}}\beta_{\text{side}}, \quad n \geq 1$$

$$\kappa_0^2 = 2ik\beta_{\text{ends}}/L_c \tag{38}$$

$$\kappa_l = \frac{l\pi}{L_c} + \frac{2ik}{l\pi}\beta_{\text{ends}}, \quad l \geq 1.$$

Also, the phase constant θ_l equals $-ik\beta_{\text{ends}}/\kappa_l$. a result useful in demonstrating that the normalization of the eigenfunctions is not altered to first order in β.

The following abbreviations will be useful in expressions for the perturbed eigenvalues:

$$\chi_1 = (-1+i)\delta_v/r_c, \quad \chi_3 = (-1+i)(\gamma-1)\delta_t/r_c,$$
$$\chi_2 = (-1+i)\delta_v/L_c, \quad \chi_4 = (-1+i)(\gamma-1)\delta_t/L_c. \tag{39}$$

In this notation, the following are correct to order χ^2, where $O(\chi^2)$ means any combination of products of the χ_j:

$$k_{00}^2 = k^2(\chi_3 + \chi_4)$$
$$k_{l0}^2 = (l\pi/L_c)^2(1+\chi_1) + k^2(\chi_3 + 2\chi_4)$$
$$k_{0n}^2 = (z_{0n}/r_c)^2(1+\chi_2) + k^2(\chi_3 + \chi_4) \tag{40}$$
$$k_{ln}^2 = (l\pi/L_c)^2(1+\chi_1) + (z_{0n}/r_c)^2(1+2\chi_2) + k^2(\chi_3 + 2\chi_4).$$

A generalized expression for the input impedance requires the square of the integral of the eigenfunction over the duct orifice

$$2\pi \int_0^{r_d} J_0(q_n r) r\, dr = 2\pi r_d J_1(q_n r_d)/q_n. \tag{41}$$

The input impedance is thus

$$\mathbf{Z}_{\text{in}} = \frac{4i\omega\rho}{\pi r_d^2 L} \sum_{nl} \left[\frac{J_1(q_n r_d)}{q_n r_c J_0(z_{0n})}\right]^2 \frac{\epsilon_l}{k_{nl}^2 - k^2}. \tag{42}$$

In the non-dissipative case the quantity q_n equals z_{0n}/r_c and the sum over l yielded an additional factor of z_{0n} in the denominator, so that the convergence was governed by a factor

$$\left[\frac{J_1(z_{0n} r_d/r_c)}{z_{0n} J_0(z_{0n})}\right]^2 \frac{1}{z_{0n}}.$$

Numerical investigation shows that the sum is dominated by terms for which $z_{0n} r_d/r_c < \pi/2$. For the dissipative case, the series expansion

$$\frac{2J_1(\zeta)}{\zeta} = 1 - \frac{\zeta^2}{8} + O(\zeta^4) \tag{43}$$

shows that this term is insensitive to the approximation $q_n \approx z_{0n}/r_c$ in this range. Accordingly, this approximation will be made within the square brackets. The main effects of dissipation come from the perturbation of the eigenvalue term in the denominator.

3.6 Complex effective volume

Consider the contributions of the $0n$ modes to the input impedance

$$Z_{\text{in}}^{(n=0)} = \frac{i\omega\rho}{\pi r_c^2 L_c} \sum_{l=0}^{\infty} \frac{\epsilon_l}{k_{0l}^2 - k^2}. \tag{44}$$

Evaluation of the sum yields

$$
\begin{aligned}
Z_{\text{in}}^{(n=0)} &= \frac{\rho c^2}{i\omega V} \left[-\chi_4 + \frac{1}{1 - \chi_3 - 2\chi_4} \frac{kL_c\sqrt{(1 - \chi_3 - 2\chi_4)/(1 + \chi_1)}}{\tan[kL_c\sqrt{(1 - \chi_3 - 2\chi_4)/(1 + \chi_1)}]} \right] \\
&= \frac{\rho c^2}{i\omega V} \left[\frac{1}{1 - \chi_3 - \chi_4} - \frac{(kL_c)^2}{3(1 + \chi_1)} + O(kL_c)^4 + O(\chi^2) \right] \\
&= \frac{\rho c^2}{i\omega \mathbf{V}} + \frac{i\omega\rho L_c}{3\pi r_c^2(1 + \chi_1)} + O(kL_c)^4 + O(\chi^2).
\end{aligned}
\tag{45}
$$

Here the complex volume $\mathbf{V}$ equals $V + (1 - i)(\gamma - 1)\delta_t S/2$, a result in agreement with prior calculations. The next correction term is shown here in a form which more explicitly suggests its interpretation as an effective length correction, now corrected by the viscous term χ_1

3.7 Complex length correction

The effects of thermal and viscous corrections to the eigenvalues on the modes with $n \geq 1$ can be included in the formalism by introducing a complex effective length correction

$$\delta_i = \frac{4}{L_c} \sum_{n=1}^{\infty} \left[\frac{J_1(z_{0n} r_d/r_c)}{z_{0n} J_0(z_{0n})} \right]^2 \sum_{l=0}^{\infty} \frac{\epsilon_l}{k_{nl}^2 - k^2}. \tag{46}$$

Evaluation of the sum yields

$$\delta_i = 4r_c \sum_{n=1}^{\infty} \left[\frac{J_1(z_{0n}r_d/r_c)}{z_{0n}J_0(z_{0n})} \right]^2 \left[\frac{\coth(z_{0n}L_c/r_c)}{z_{0n}\sqrt{(1+\chi_1)(1+2\chi_2)}} + \frac{r_c\chi_2}{z_{0n}^2 L_c} \right] \quad (47)$$

where terms of order $(kr_c)^2$ and χ^2 have been dropped, and all corrections to the argument of the hyperbolic cotangent have been dropped. The major effect is that the previous expression for δ_i is multiplied by a factor of approximately $(1 - \chi_1/2 - \chi_2)$:

$$\delta_i = \delta_i \left[1 - (-1+i)\left(\frac{\delta_v}{2r_c} + \frac{\delta_v}{L_c} \right) \right] + \frac{4r_c^2(-1+i)\delta_v}{L_c^2} \sum_{n=1}^{\infty} \left[\frac{J_1(z_{0n}r_d/r_c)}{z_{0n}^2 J_0(z_{0n})} \right]^2 . \quad (48)$$

Here the second term has been simplified by the usual approximations. Owing to the additional z_{0n} in the denominator, it will converge much more rapidly than the series for δ_i.

The imaginary terms correspond to a specific acoustic resistance of the orifice equal to the product of the imaginary part of δ_i and $\rho\omega$. The effect on the imaginary part of the resonance frequency may be estimated by noting that the mass end correction alters the frequency by a fraction δ_i/L_d. For small duct radii the real part of δ_i is approximately $8r_d/3\pi$. The fractional eigenfrequency due to the imaginary part is thus

$$\frac{\Delta g}{f_0} \approx \frac{8}{3\pi} \frac{r_d}{L_d} \left(\frac{\delta_v}{2r_c} + \frac{\delta_v}{L_c} \right) . \quad (49)$$

This is a much smaller correction than those estimated numerically in Part I. Further work is required to clear this up.

4   Acoustic model of the viscometer

The formalism of the last section shows that the resonator input impedance can be written in the form

$$\mathbf{Z}_{\text{cavity}} = \frac{\rho c^2}{i\omega V} + \frac{i\omega \rho L_c}{3\pi r_c^2(1+\chi_1)} + \frac{i\omega\rho}{\pi r_d^2}\delta_i + O(kL_c)^2 + O(\chi^2), \quad (50)$$

the length correction term implicitly including the orifice equivalent resistance. For brevity in further development it will be convenient to group the

second term with a redefined effective length δ'_i, so that the cavity impedance is

$$\mathbf{Z}_{\text{cavity}} = \frac{\rho c^2}{i\omega \mathbf{V}} \left[1 - \frac{k^2 \mathbf{V} \delta'_i}{A} \right]. \tag{51}$$

The viscometer consists of a duct terminated at each end by a cavity. The impedance at one end of the duct due to the load $\mathbf{Z}_{\text{cavity}}$ at the other end is given by the transmission line equation as

$$\frac{\mathbf{Z}_{\text{duct}}}{\mathbf{Z}_0} = \frac{\mathbf{Z}_{\text{cavity}}/\mathbf{Z}_0 + \tanh(\boldsymbol{\Gamma} L_d)}{1 + (\mathbf{Z}_{\text{cavity}}/\mathbf{Z}_0) \tanh(\boldsymbol{\Gamma} L_d)}. \tag{52}$$

The resonance condition is that the sum of the impedances of the left cavity and the input impedance of the duct coupled to the cavity should be zero:

$$\mathbf{Z}_{\text{cavity}} + \mathbf{Z}_{\text{duct}} = 0. \tag{53}$$

This is equivalent to

$$\frac{2\mathbf{Z}_{\text{cavity}}}{\mathbf{Z}_0} + \left(1 + \frac{\mathbf{Z}_{\text{cavity}}^2}{\mathbf{Z}_0^2} \right) \tanh\left(\boldsymbol{\Gamma} L_d \right) = 0, \tag{54}$$

or more conveniently, to

$$\frac{2\mathbf{Z}_{\text{cavity}}}{\mathcal{Z} L_d} + \frac{\tanh\left(\boldsymbol{\Gamma} L_d \right)}{\boldsymbol{\Gamma} L_d} \left(1 + \frac{\mathbf{Z}_{\text{cavity}}^2}{\mathbf{Z}_0^2} \right). \tag{55}$$

These equations provide a theoretical basis for calculating the resonance frequencies of the Greenspan viscometer.

5 Summary

The major result of this report are the following:

- The pressure and velocity fields within the cavities of the Greenspan resonator have been calculated theoretically. The calculations are in excellent agreement with the numerical results reported in Part I. Thus either theoretical or numerical calculations can be used with confidence in calculating viscous and thermal losses in the cavities.

- The cavity input impedance has been calculated. The results can be described as the sum of a volume compliance term and a mass end correction term. The volume compliance must be calculated carefully in order to include effects of the same order of magnitude as the mass end correction.

- Viscous and thermal boundary-layer effects were introduced into the formalism. The modification of the volume compliance due to thermal terms agrees exactly with simpler models. The calculation of viscous effects are inconclusive; further work is needed to clarify the results.

Design of acoustic devices for the accurate and precise measurement of transport properties of pure and mixed gases
Part III
Resonator geometries optimized for measuring thermal conductivity

by

James B. Mehl
1014 Baylor Drive
Nottingham Green
Newark, DE 19711-3130

28 September 1994
(Corrected printing of 29 January 1995)

1

Contents

ω	$2\pi\times$ frequency
ρ	density of the gas
c	speed of sound in the gas
k	ω/c
r_d	duct radius
$A = \pi r_d^2$	cross-sectional area of duct
L_d	duct length
$V = \pi r_c^2 L_c$	cavity volume (one cavity)
L_c	cavity length
r_c	cavity radius

Table 1: Notation

1 Introduction

Consider an acoustic cavity resonator consisting of two cylindrical sections, each of length L_c, coupled by an array of circular ducts of length L_d. A simple geometric model for the duct array is a solid metal block drilled through by an array of circular holes. The density of holes is limited in the practical case to the "close-packed" configurations. Somewhat higher hole cross-sectional areas can be obtained by using close-packed hexagonal ducts. The theory outlined here will be approximately applicable to the latter case.

The model is based on a suggestion of Moldover[1] that placing a duct array at the center of a cavity will affect longitudinal modes differently, depending on the mode index. Modes with an odd number of half wavelengths in the cavity length have a velocity antinode at the (axial) center of the cavity so the interaction with the duct array will be primarily viscous. Even-numbered modes have a velocity node at the center so the viscous interaction will be weak. However, there will be a temperature (and pressure) antinode at the center so that thermal effects will dominate the interaction.

2 Acoustic model

Consider the following model: The geometry is approximately equivalent to a parallel set of cavities, each cavity consisting of similar units. Let z be the coordinate along any minicavity axis. From $z = 0$ to $z = L_c$ and from $z = L_c + L_d$ to $z = 2L_c + L_d$ a slip boundary condition will be assumed, *i.e.* no viscous interaction with the walls; also the cross sectional area A' in these regions is taken equal to the geometric cross-section. From $z = L_c$ to $z = L_c + L_d$ assume the sound is propagated in a duct of cross-sectional area $A < A'$, with propagation parameters given by the circular duct model described in Part II of report. Circular ducts should be a good approximation to the hexagonal ducts. Comparisons between square and circular ducts have been made by Roh *et al*[2]

The resonator sections can be described in a transmission line model. The

---

[1] Michael R. Moldover, private communication

[2] H. S. Roh, W. P. Arnott, J. M. Sabatier, and R. Raspet, "Measurement and calculation of acoustic propagation constants in arrays of small air-filled rectangular tubes," *J. Acoust. Soc. Am.* **89**, 2617–2624 (1991).

relevant equations are

$$\frac{\partial p}{\partial z} = -\mathcal{Z}\mathbf{U} \tag{1}$$

$$\frac{\partial \mathbf{U}}{\partial z} = -\mathcal{Y}\mathbf{p} \tag{2}$$

$$\mathcal{Z} = \frac{i\omega\rho}{A}\frac{1}{1-F_v} = \text{series impedance} \tag{3}$$

$$\mathcal{Y} = \frac{i\omega A}{\rho c^2}[1 + (\gamma - 1)F_t] = \text{shunt admittance} \tag{4}$$

$$\mathbf{Z}_0 = \sqrt{\mathcal{Z}/\mathcal{Y}} = \text{characteristic impedance} \tag{5}$$

$$\Gamma = \sqrt{\mathcal{Z}\mathcal{Y}} = \text{propagation parameter} \tag{6}$$

$$F_v = 2J_1(\zeta)/[\zeta J_0(\zeta)], \quad \zeta = (1-i)r_d/\delta_v \tag{7}$$

$$F_t = 2J_1(\zeta)/[\zeta J_0(\zeta)], \quad \zeta = (1-i)r_d/\delta_t. \tag{8}$$

Consider the cavity in $0 \le z \le L_c$. If dissipation is neglected in this region the acoustic pressure and volume velocity are

$$p = p_0 \cos kz$$
$$U = \frac{A'p_0}{i\rho c}\sin kz. \tag{9}$$

The acoustic impedance at $z = L_c$, defined as the ratio of the pressure to the *volume* velocity, is

$$\mathbf{Z}(L_c)_- = \frac{i\rho c}{A'\tan(kL_c)}. \tag{10}$$

The fields in the viscometer as a whole must be either symmetric or antisymmetric. It is simpler to construct solutions by taking this symmetry explicitly into account. For the anti-symmetric solutions, with $z' = L_c + L_d/2 - z$, the pressure and volume velocity are

$$p = p_1 \sinh \Gamma z'$$
$$U = -\frac{p_1}{\mathbf{Z}_0}\cosh \Gamma z', \tag{11}$$

and for the symmetric case

$$p = p_1 \cosh \Gamma z'$$
$$U = \frac{p_1}{Z_0} \sinh \Gamma z'. \tag{12}$$

The impedance at $z = L_c$ for these solutions is

$$\mathbf{Z}(L_c)_+ = \begin{cases} -\mathbf{Z}_0 \tanh(\Gamma L_d/2), & \text{antisymmetric} \\ -\mathbf{Z}_0 \coth(\Gamma L_d/2), & \text{symmetric}. \end{cases} \tag{13}$$

The condition for resonance is that $\mathbf{Z}(L_c)_- + \mathbf{Z}(L_c)_+ = 0$, or

$$\frac{i\rho c}{A' \tan kL_c} = \mathbf{Z}_0 \begin{cases} \tanh(\Gamma L_d/2), & \text{antisymmetric} \\ +\coth(\Gamma L_d/2), & \text{symmetric}. \end{cases} \tag{14}$$

The antisymmetric case simplifies upon use of

$$\mathbf{Z}_0 \Gamma L_d = \mathcal{Z} L_d = \frac{i\omega\rho L_d}{A(1 - F_v)} \tag{15}$$

to

$$A' \tan kL_c = \frac{2A(1 - F_v)}{kL_d} \left[\frac{\Gamma L_d/2}{\tanh(\Gamma L_d/2)} \right]. \tag{16}$$

Similarly, the symmetric case simplifies upon use of

$$\frac{\Gamma L_d}{\mathbf{Z}_0} = \mathcal{Y} L_d = \left[\frac{\rho c^2}{i\omega A[1 + (\gamma - 1)F_t]} \right]^{-1} L_d \tag{17}$$

to

$$A' \tan kL_c = -\frac{1}{2} kL_d A[1 + (\gamma - 1)F_t] \left[\frac{\tanh(\Gamma L_d/2)}{\Gamma L_d/2} \right]. \tag{18}$$

For short ducts the ratios of the hyperbolic tangent to its argument can be approximated by unity. If in addition kL_d is small, the solutions for the symmetric case will have small values of $\tan kL_c$ determined primarily by thermal effects, and the solutions for the antisymmetric case will have large values of $\tan kL_c$ determined primarily by viscous effects.

To proceed further let

$$kL_c = \frac{l\pi}{2} + \Delta kL_c \tag{19}$$

so that

$$\tan(kL_c) = \begin{cases} -\cot(\Delta kL_c) & \text{for } l \text{ odd} \\ \tan(\Delta kL_c) & \text{for } l \text{ even.} \end{cases} \qquad (20)$$

The odd-l solutions have overall antisymmetry; the antisymmetric boundary condition requires

$$\Delta kL_c \approx \frac{-kL_d}{2} \frac{A'}{A} \frac{1}{1 - F_v}, \qquad (21)$$

i.e. the losses are dominated by viscous effects. Similarly, for the even-l symmetric cases

$$\Delta kL_c \approx \frac{-kL_d}{2} \frac{A}{A'} [1 + (\gamma - 1)F_t], \qquad (22)$$

i.e. the losses are dominated by thermal effects.

Numerical techniques may be more appropriate than an algebraic approach for the case where kL_d is not small. It may be simplest to handle this within a steady-state response calculation.

3   Improved model

An improved model is obtained by accounting for viscothermal boundary effects in the end cavities in the usual way. It is then appropriate to consider the array of ducts as a set of N parallel transmission lines. each of cross-sectional area A. The resonance condition is

$$\mathbf{Z}(L_c)_- + N\mathbf{Z}(L_c)_+ = 0 \qquad (23)$$

where $\mathbf{Z}(L_c)_-$ is similar to the previous expression

$$\mathbf{Z}(L_c) = \frac{i\rho c}{A' \tan(\theta_l + \kappa_l L_c)}. \qquad (24)$$

Here A' is now the total cross-sectional area of the cavity, and a complex propagation parameter and phase shift have been introduced in order to satisfy the visco-thermal boundary conditions in the cavity. The cavity impedance should also be modified by the addition of a mass end correction, as discussed in Parts I and II. However, this correction should be calculated based on the assumption that the wave field expands only from an area A to a fractional area A'/N. In such a case both the Ingard theory and numerical techniques show that the mass end correction is much smaller than $\sqrt{A}$.

4   Numerical test

A numerical test of the dissipation-free case was carried out with the BIE software. The cavity dimensions correspond to one of the experimental viscometers: $L_c/r_c = 39.776/20$, $L_d/r_c = 48/20$. Calculations were carried out for a large duct with $r_d/r_c = 0.8$. The eigenfunction is shown as a function of arc length measured from the center of the cavity in Fig. 1. Note that the eigenfunction varies with arc length along the baffle outside the duct. This shows up as a discontinuity in pressure when the same data are plotted as a function of z/L_c in Fig. 2. Theoretical lines corresponding to the waveguide formalism are also shown. The two lines were calculated with the numerical value of k and the value determined from Eq. (15), which was about 1.4% higher. The effects on the eigenfunction are minimal.
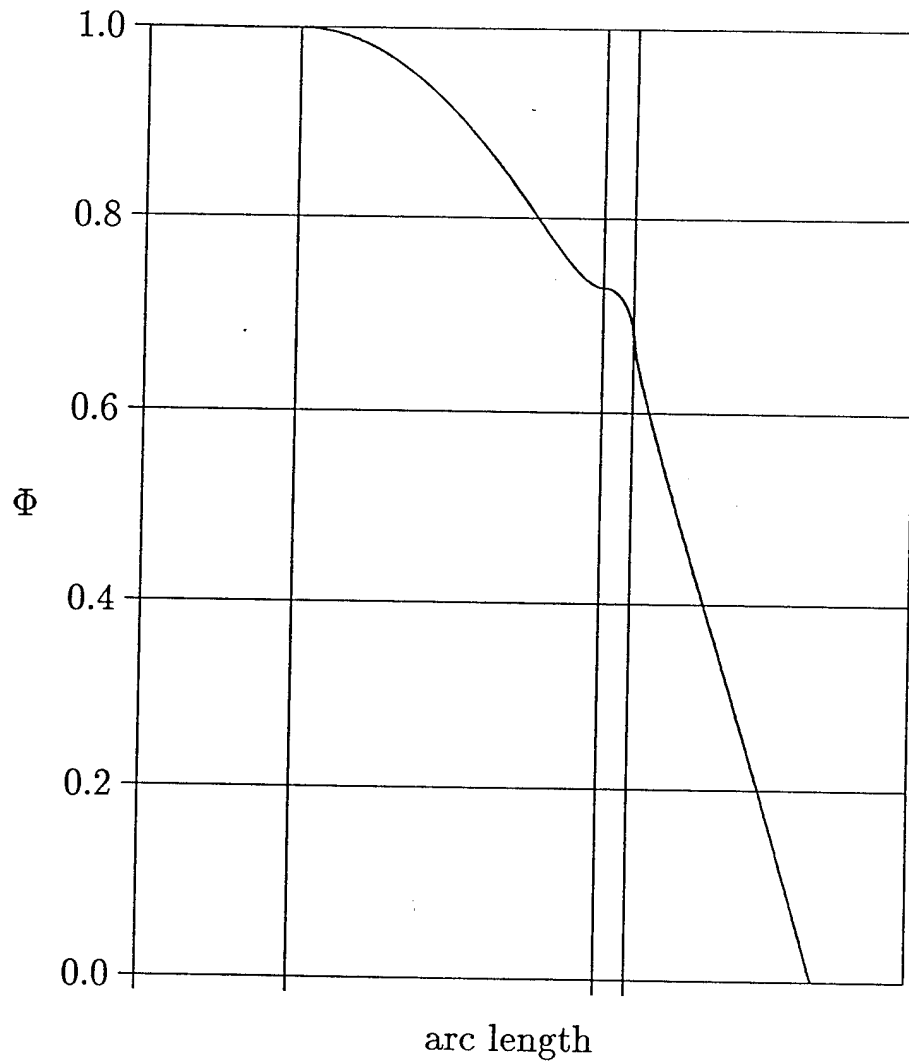
Figure 1: Numerical calculation of the eigenfunction for the dissipation-free case. The vertical lines mark the positions of the corner at $z = 0$, $r = r_c$, the corner at $z = L_c$, $r = r_c$, and the entrance to the duct.
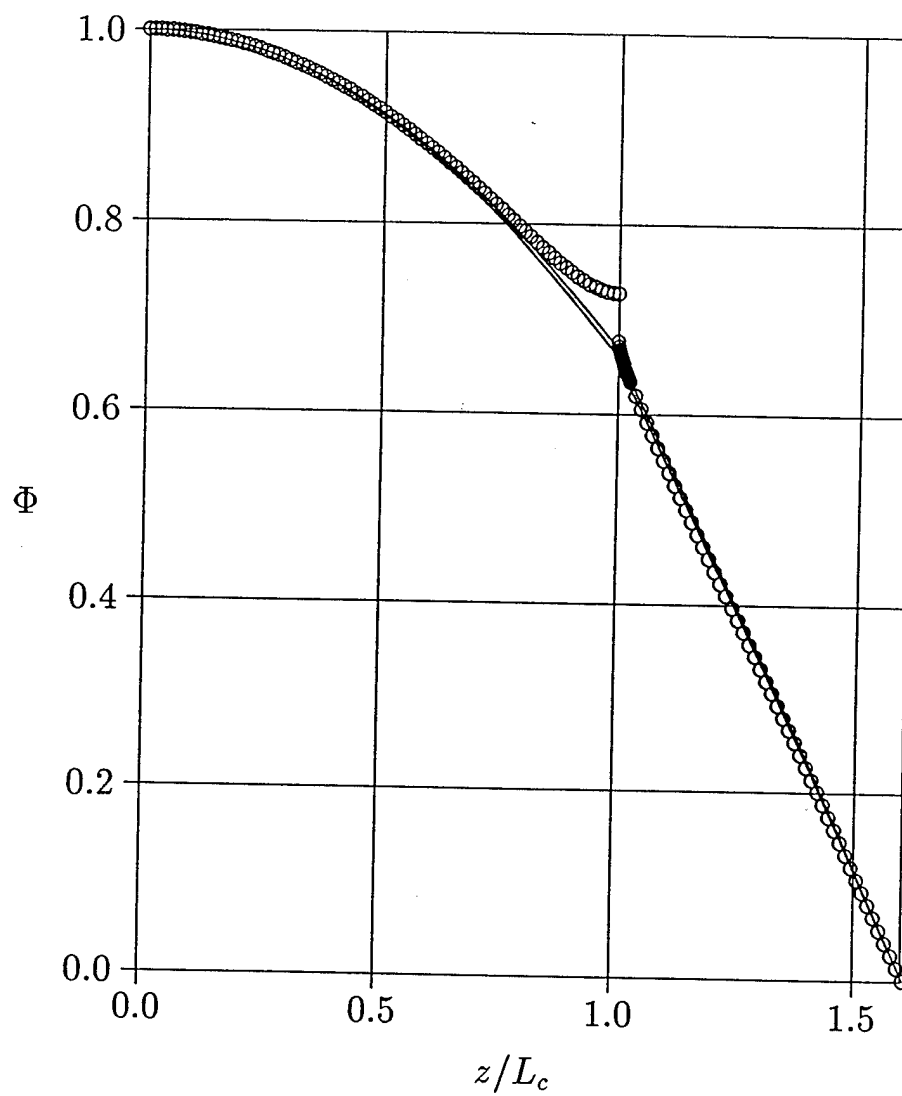
Figure 2: Numerical calculation of the eigenfunction for the dissipation-free case, compared with calculated lines using the formalism of this report.